

Review

Exploring Deposition Techniques and Supramolecular Arrangement in Thin Films for Sensor Applications

Celina M. Miyazaki ^{1,*}, Cibely S. Martin ², Maíza S. Ozório ¹, Henry S. Kavazoi ¹, Carlos J. L. Constantino ¹ and Priscila Aléssio ¹

¹ School of Technology and Sciences, São Paulo State University (UNESP), Presidente Prudente 19060-900, SP, Brazil; maiza.ozorio@unesp.br (M.S.O.); henry.seitiro@unesp.br (H.S.K.)

² School of Engineering, São Paulo State University (UNESP), Ilha Solteira 15385-000, SP, Brazil; cibely.martin@unesp.br

* Correspondence: celina.miyazaki@unesp.br or celinammiyazaki@gmail.com

Abstract: In recent decades, many research efforts have been dedicated to finding highly sensitive devices for fast and reliable identification and quantification of an expanding range of analytes. As a result, there has been an increased number of publications dedicated to this area and a consequent increase in the number of review papers on the subject. However, unlike most review articles, we chose to explore the impact of supramolecular arrangement (or deeper, when possible, approaching the molecular organization) and assembly variables on sensing performance. This review briefly discusses the methods used to determine the molecular organization of thin films. We also examine various deposition techniques, including Langmuir-Blodgett, Langmuir-Schaefer, Layer-by-Layer assembly, electrodeposition, and spray pyrolysis, describing mainly (but not limited to) the advances in the last five years in developing thin films for sensors, with a particular emphasis on how the supramolecular arrangement can influence the sensing properties of these films.

Keywords: supramolecular arrangement; thin film; Langmuir-Blodgett; Langmuir-Schaefer; Layer-by-Layer; electrodeposition; spray pyrolysis



Citation: Miyazaki, C.M.; Martin, C.S.; Ozório, M.S.; Kavazoi, H.S.; Constantino, C.J.L.; Aléssio, P. Exploring Deposition Techniques and Supramolecular Arrangement in Thin Films for Sensor Applications. *Chemosensors* **2023**, *11*, 524. <https://doi.org/10.3390/chemosensors11100524>

Academic Editors: Boris Lakard and Maria Raposo

Received: 8 August 2023

Revised: 23 September 2023

Accepted: 30 September 2023

Published: 5 October 2023



Copyright: © 2023 by the authors. Licensee MDPI, Basel, Switzerland. This article is an open access article distributed under the terms and conditions of the Creative Commons Attribution (CC BY) license (<https://creativecommons.org/licenses/by/4.0/>).

1. Introduction

Chemical sensors are defined by the International Union of Pure and Applied Chemistry (IUPAC) as devices that transform chemical information into an analytically useful signal [1]. According to Araujo, Reddy, and Paixão [2], chemical sensors are devices that respond to an analyte based on a chemical reaction (or recognition) and can be used for the qualitative or quantitative determination of species being analysed in order to provide an analytical output. For detection purposes, a variety of materials can be applied as recognition elements, and the way this (or these) material is organized or assembled as a thin film is decisive to the success of the detection. When considering “the way” they are organized, one should delve into the material deposition method, going further to the supramolecular arrangement level and deeper at the species interacting between the sensing material and the target. The term “supramolecular chemistry” refers to interactions and structures originated by noncovalent intermolecular forces [3]. When considering “supramolecular arrangement”, its scope extends beyond molecular organization, encompassing the latter and including other aspects such as crystallinity, surface morphology, and thickness. In this review paper, we approach the influence of the supramolecular arrangement in sensor applications and, when possible, we specifically address the molecular organization in thin films. The term spatial orientation (or simply orientation) is preferred when refer to the organization of nanostructures such as one or two-dimensional materials.

Considering the range of possibilities available today, simple approaches such as the Layer-by-Layer (LbL) self-assembly [4] or more sophisticated ones such as the Langmuir-Blodgett (LB) [5,6] enable nanoscale control over desired characteristics through controllable

experimental parameters. For instance, they allow control over morphology, which can be interesting to particles or molecules adsorption due to the increased surface area, or also provide the possibility of tuning the charge transfer aiming applications such as electrical (impedimetric and chemiresistive) or electrochemical sensors.

In this review, we discuss methods to manipulate materials to form thin films towards the manufacture of sensing surfaces. We start with the LB and Langmuir-Schaefer (LS) techniques, which are based on forming an ordered monolayer on the air-water interface and the transference of this monolayer onto a solid substrate. Perhaps, this one allows the most precise control over the thickness and the molecular organization in thin films. Next, we delve into the topic of the LbL technique. Based on the spontaneous adsorption of materials onto a solid substrate, the simplicity and versatility of this technique make it the most employed functionalization strategy for many applications. Following, we discuss the electrodeposition methods, which appear as a rapid and environmentally friendly way to modify electrodes. Thus, avoiding lengthy and tiring reactions as well as the use of harmful reagents. Finally, we have commented on the spray pyrolysis approach, based on spraying the precursor solution onto a heated solid, leading to thermal decomposition and film formation. The scalability and simplicity of the setup are the advantages of this method, which has gained attention in many application fields.

2. The Investigation of Molecular Organization

The study of supramolecular arrangements involves understanding the principles governing the formation, stability, and properties of these structures. Moreover, by manipulating supramolecular arrangements, new functional thin films can be developed for several applications, especially sensors. The manipulation of supramolecular arrangement can be performed by changes in experimental parameters such as solvent [7], chemical structure, chain substitution [8,9], deposition techniques [10,11] as well as heat treatments [12]. Specifically, to examine the molecular organization, techniques such as FTIR (Fourier Transform Infrared Spectroscopy) and XRD (X-ray Diffraction) can be used individually or combined to provide valuable insights helping to understand its effect on their properties.

Vibrational spectroscopy is one of the most used techniques to determine organization at the molecular level. For FTIR, due to the molecular organization and the interaction between the electric field of the incident radiation and the molecular electric dipole of the molecule during the vibration, the spectra can present differences in their band intensities. Thus, this relation is called the selection rule [8,13–15] and refers to the conditions under which a vibrational mode of a molecule will give rise to an observable absorption band in the infrared spectrum.

Based on the selection rule in FTIR measurements, the intensity of the signal I is proportional to the scalar product of the dipole moment μ and the electric field E : $I \propto (\vec{\mu} \cdot \vec{E})^2$ [16]. The absorption signal is intense when the dipole moment of the vibration mode is parallel to the electric field of the infrared (IR) beam. Thus, for a better determination of molecular organization through a film surface, FTIR characterization can be performed by reflection and transmission modes [8]. The reflection mode using an incident beam angle of 80° is typically employed [8], but in some cases, the attenuated total reflection (ATR) mode can be used by taking the measurement very close to the film surface [17–21]. Essentially, in the reflection mode, the \vec{E} is polarized mostly perpendicular to the substrate surface (Figure 1), thus promoting a strong signal for vibration modes with a dipole moment perpendicular to the substrate surface, while the vibration modes with a dipole moment parallel to the substrate tend to be suppressed. The opposite effect is expected in the transmission mode, where the \vec{E} is polarized parallel to the substrate surface (Figure 1). The signal is strong for vibration modes with a dipole moment parallel to the substrate surface, while the absorption signal for vibration mode with a dipole moment perpendicular to the substrate tends to be suppressed. It is possible to determine the molecular organization by comparing

the contrasting signal (relative intensity) obtained from the spectra acquired in reflection and transmission modes [8].

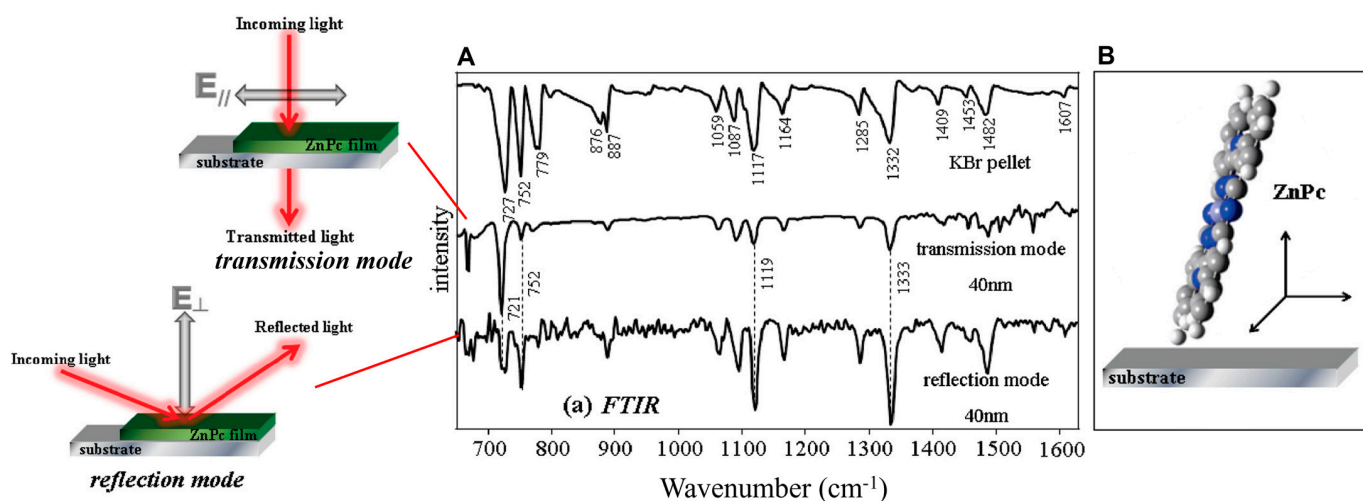


Figure 1. (A) Transmission and reflection modes–FTIR spectra of ZnPc film and corresponding representation of the electric field and surface selection rules. The ZnPc powder in the potassium bromide (KBr) pellet spectrum references random orientation. (B) Illustration of the ZnPc molecular organization in PVD films. Adapted with permission from [22]. Copyright 2010 American Chemical Society.

When using this strategy, it is important to discard the influence of the substrate since different surfaces may end up eliciting different molecular organizations. The reflection mode is usually performed on a metal-covered surface, while the transmission analysis requires an IR transparent substrate such as zinc selenide (ZnSe) or Germanium. On metal surfaces, the chemical or strong physicochemical interactions of the film with the adhesion organic layer (a self-assembled monolayer, SAM) can interfere with the supramolecular arrangement. In this case, an intermediate oxide layer between the metal surface and the film of interest avoids the chemisorption and consequently preserves the vibrational modes from the film [23,24].

Another approach for analysing molecular organization involves the comparison of the FTIR spectrum of the film collected in either reflection or transmission modes to the spectrum of the monomer (powder precursor) dispersed in potassium bromide (KBr, IR-transparent matrix) [8], assuming for the later a random distribution (isotropic structure) [22,25]. Aroca and Thedchanamoorthy [8] described the molecular organization of evaporated films of InClPc (indium(III) chloro phthalocyanine), analysing the changes in the relative intensities when comparing the spectrum of the powder in KBr pellet (random orientation) to the transmission mode spectrum of a 25 nm-thick film onto KBr and to the reflection mode spectrum of a 25 nm-thick film on a silver substrate. Zanolini et al. [22] investigated the organization of evaporated ZnPc (zinc phthalocyanine) films by analysis of the spectra of a powder sample in KBr pellet by transmission mode, the 40 nm-thick film onto ZnSe by transmission mode and a 40 nm-thick film on a silver substrate in reflection mode, as shown in Figure 1. Through the comparison of the relative intensities of each spectrum, observing the dominance of the out-of-plane stretching of the C–H band in the transmission mode, which becomes weaker in the reflection mode, it was suggested that the ZnPc molecules were preferentially organized with the macrocycle ring practically perpendicular to the surface substrate [22].

Polarized infrared spectroscopy has been applied to the determination of molecular organization [26], for instance, grazing angle attenuated total reflection (GATR) [17], p-polarized multiple-angle incidence resolution spectrometry (pMAIRS) [27–29] and polarization modulation infrared reflection-absorption spectroscopy (PM-IRRAS) have been

reported [20,23,30–32]. The mentioned polarized infrared techniques measure the reflected light and are used to study surface properties and molecular organization but differ in the experimental setup and parameters. Fraczak, Uznanski, and Moneta [17] presented an approach to investigate the molecular organization of pentacene on SiO₂ surface by comparing FTIR spectroscopy at transmission and by polarized attenuated total reflectance geometry at GATR. In the s- and p-polarized GATR, it is possible to observe only vibration modes with non-zero components of transition dipole moments parallel or perpendicular to the surface [33]. Thus, the molecular organization was determined by comparing the band intensities related to characteristic vibrations of chemical bonds: all vibrations (in-plane and out-of-plane) were observed in the spectrum collected through the p-polarized beam, while the spectrum originated from the s-polarized source depicted some bands gaining intensity and others significantly reduced. Since the unpolarized IR beam at normal incidence excites only the vibration modes with transition dipole components parallel to the substrate surface, the comparison of band intensities of the transmission mode spectrum and the s-polarized GATR spectrum helped to establish the molecular organization of pentacene, which was with the molecules standing almost perpendicular to the SiO₂ substrate [17].

Although Raman spectroscopy has been widely used to investigate the composition and structure of materials, the analysis of molecular organization became restricted to the case of surface-enhanced Raman scattering (SERS). For instance, in the case of SERS, the selection rules favour the vibrations which occur perpendicular to the particle surface [34]. Still, molecules or nanostructures adsorbed on the top of a plasmonic surface can have their organization investigated by Raman spectroscopy [34]. However, the configuration of polarized Raman spectroscopy can be applied for this purpose, interpreting the scattering intensities for different polarized scattering geometries [35]. Polymer fibres [36], 2D materials [37,38] and nanotubes [39,40] have already been investigated. For instance, angle-resolved polarized Raman spectroscopy (ARPRS) permits rotating the polarization of incident light or rotating the sample in the plane [41]. Particularly for graphene nanoplatelets, the intensity scattering of the Raman band depends on the axis of laser polarization when the laser beam is parallel to the graphene sheet plane [37,42]. Based on this, Li et al. [37] developed ways to establish the spatial orientation (correlated to molecular organization, but considering the 2D graphene structure) of GO flakes in nanocomposites.

Especially for films obtained by Langmuir films (Langmuir-Blodgett, LB and Langmuir-Schafer, LS), the molecular organization can be previously induced and investigated on the air/water interface. Interpreting the π -A isotherm and the extrapolated mean area allows us to infer the molecules or nanomaterials organization before the film transference to a substrate [43,44]. However, it is important to consider that the transference process to a solid substrate can induce a different organization [45]. Therefore, other characterization techniques should confirm the organization post-transference. An interesting example that represents the previous establishment of the organization by the formation of Langmuir films occurs for one-dimensional (1D) nanomaterials, which carry extreme anisotropic properties [46,47]. The barrier compression led to the formation of well-aligned 1D structures, which can be collected both by the horizontal or vertical dipping of the substrate. Miao et al. [48] have synthesized ZnO nanowires (Figure 2A, in random orientation) and aligned them by the barrier compression. Figure 2B,C depict a traditional π -A isotherm with the different compression states (details in Section 3.1) and a scanning electron microscopy (SEM) image of the aligned structures, respectively. The XRD analysis (Figure 2D) of the collected LB film indicated a hexagonal wurtzite structure, which is highly [100]oriented along the surface normal. Considering the XRD information allied to high resolution-transmission electron microscopy (HRTEM) (Figure 2E), the authors ascribed the topography depicted in Figure 2F.

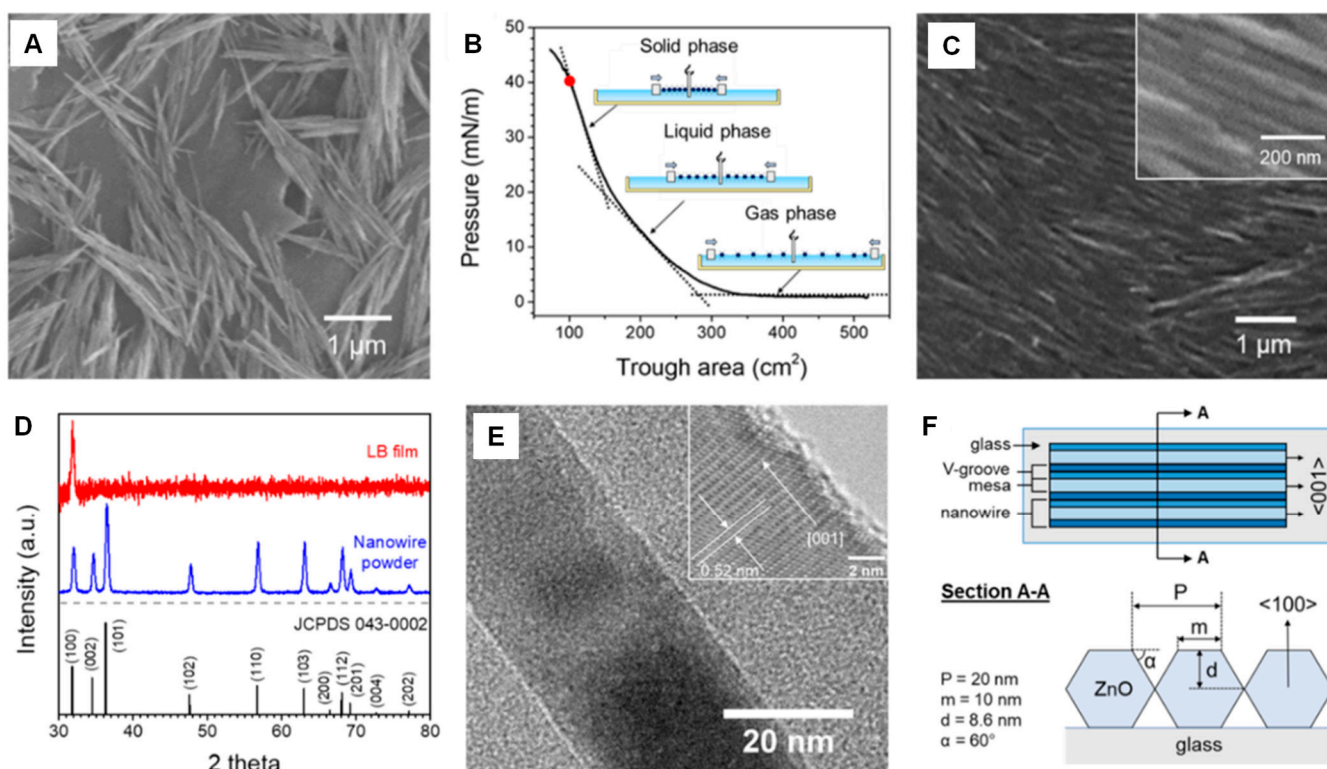


Figure 2. (A) SEM images of the as-synthesized ZnO nanowires, (B) the compression isotherm, and (C) SEM image of the ZnO LB film on Au-IDE-glass substrate. (D) XRD patterns of the ZnO LB film. (E) TEM image of the ZnO nanowire and HRTEM image (inset) depicting the lattice fringes. (F) Illustration of the v-groove topography of the ZnO film. Reprinted with permission from [48]. Copyright 2020 American Chemical Society.

Regarding crystalline materials, crystallography is also applied to determine the organization, specifically the three-dimensional arrangement of atoms or molecules within a crystal lattice. However, it may not be suitable for amorphous or disordered systems lacking long-range order. X-rays are directed at the crystal in XRD, and their interaction with the crystal lattice causes diffraction or scattering [49]. The resulting diffraction pattern is recorded and analysed to extract information about the arrangement of atoms or molecules within the crystal. Therefore, the diffractogram reveals how individual units interact and organize themselves in the crystal structure, which is crucial for studying their properties. Rivalta et al. [50] investigated the molecular organization and phase of indigo molecules deposited on silica surfaces by XRD and micro-Raman spectroscopy, respectively. By the XRD peak position and the interplane distance (from Bragg's Law), it was possible to infer that indigo molecules are oriented alongside the (1 0 0) plane while the polymorph B was determined by the specific Raman spectrum.

Currently, several techniques (or combinations of techniques) can be used to infer molecular organization in thin films. Despite being widely known that the molecular organization directly influences the properties of these films and, consequently, has a direct influence on the performance of sensors, due to the inaccessible experimental setup as well as complex and time-consuming data analysis, there are a relatively small amount of works that investigate molecular organization influence in sensors. Indeed, the works dedicated to this study demand an in-depth investigation, ultimately leading to a subject that fills a manuscript. On the other hand, most sensor application papers are worried about analytical performance. Here, we tried to find a balance or connection between the fabrication techniques, molecular organization (or supramolecular arrangement in general) and the sensing application.

3. Supramolecular Thin Films Assembly Techniques

3.1. Langmuir-Blodgett and Langmuir-Schaefer Assembly

The precise tuning of thin film growth and the possibility of achieving the desired supramolecular arrangement is the main reason for choosing the Langmuir-Blodgett (LB) and Langmuir-Schaefer (LS) depositions. Going back to 1917, Irving Langmuir demonstrated the precise control of monolayer formation at the General Electric Labs [51]. Later in 1935, his assistant Katharine Blodgett reported the sequential transferring of the floating monolayer from the air/water interface to a solid substrate [51,52].

A Langmuir trough is necessary to fabricate LB or LS films, as shown in Figure 3A. The trough consists of an inert Teflon recipient containing the aqueous subphase and some characterization accessories, essentially, a surface pressure sensor (a Wilhelmy plate) to monitor the different stages of the film organization. Other accessories, such as a surface potential analyser, PM-IRRAS [53] and Brewster angle microscopy [54] can be added to the set-up. A volatile solvent is used to suspend the material of interest (e.g., chloroform, toluene, hexane), which is spread onto the aqueous subphase using a microsyringe. After solvent evaporation, the compression of the moving barriers leads to a decrease in area. As a result, the molecules are forced into an organized state, passing through the initial gaseous phase (see Figure 3B (1)) to the liquid phase (2), followed by the condensed phase (3) and finally, the collapse of the film (4) with the superposition of molecules [5,55].

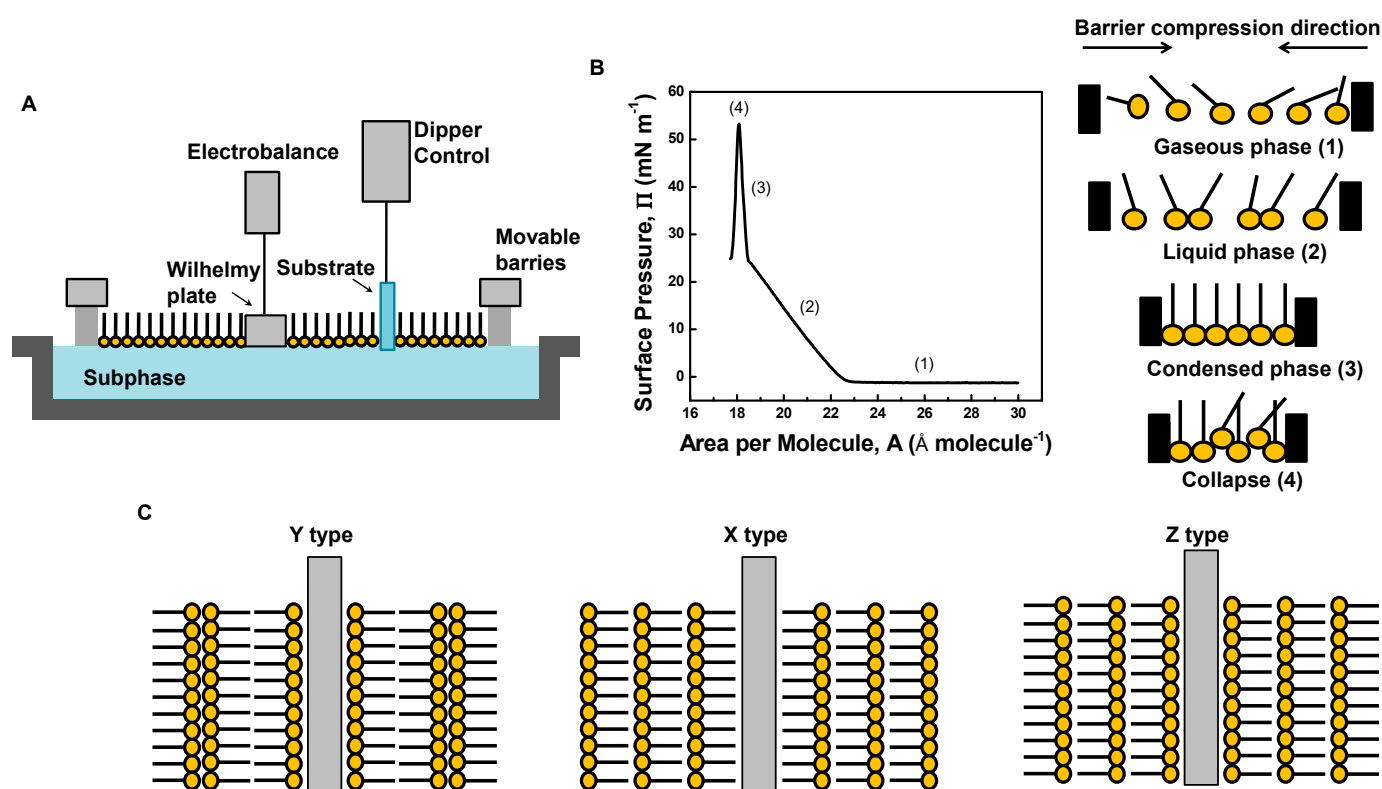


Figure 3. (A) Schematics of a Langmuir trough after amphiphilic molecule monolayer formation; (B) π -A isotherm depicting different phases during the barrier compression: (1) gaseous, (2) liquid, and (3) condensed phases, (4) collapse of the film. (C) Representation of the molecular organization of Y, X, and Z-types of LB films.

The thin film with a high organization can be transferred to a solid substrate as an LB or LS film. For the LB films, the substrate is vertically immersed or raised. For a hydrophilic substrate, Y-type deposition is achieved by the first raising of the substrate from the subphase, and consecutive immersion and raising cycles lead to molecules stacking in a head-to-head and tail-to-tail configuration (Figure 3C). The X-type LB film is formed

when the deposition occurs only during the substrate down stroke, whereas the Z-type films are produced when the deposition occurs only during the substrate up stroke [52]. The LS films, introduced by Irving Langmuir and Vicent Schaefer [55], involve the horizontal contact of the substrate with the compressed Langmuir film. The LS method is preferred for rigid monolayers, although it allows less control over deposition compared to the LB films [56]. In-depth information on the subject of Langmuir monolayers and Langmuir-Blodgett films can be found in M. Petty “Langmuir-Blodgett Films: an introduction” and A. Ulman entitled “Langmuir-Blodgett Films: An Introduction to Ultrathin Organic Films from Langmuir-Blodgett to Self-Assembly” [5,55]. Some recent review papers also bring the essence of LB films [6,57].

Initially, the LB technique was solely used for amphiphilic molecules. However, it has been expanded to include several materials to explore new applications. A plethora of literature exists on the applications of LB and LS techniques with different materials, such as metal nanoparticles [58–61], carbon nanotubes [62–65], graphene [66–69], biomolecules [70–72], metal-organic frameworks [73,74], conjugated polymers [75] and others. The LB and LS techniques have been used to fabricate hybrid films solely or combined with other approaches: (1) spreading a mixture of materials [63,76], (2) spreading a material on the air-water interface, and using the second material in the subphase [69,77]; (3) to assembly LB or LS films intercalated with self-assembled layers [68,78–80].

The control of parameters such as molecular organization and thickness is very important for sensor fabrication. Remarkably, the LB and LS techniques allow for the manipulation of packing, wrinkling, and folding of graphene nanosheets [81,82], the control of the packing density of metal nanoparticles [59–61], or the alignment of 1D materials [63,83,84]. A multitude of materials has been successfully applied as LB and LS films in sensing applications. However, due to space limitations, we will focus on a selected group of materials: graphene derivatives, 1-D materials, and nanoparticles.

3.1.1. Graphene-Derivatives

Cote, Kim, and Huang [81] pioneered assembling single graphene oxide (GO) layers by the LB assembly in 2008. The first thing to mention is that common solvents for spreading solutions, such as chloroform or toluene, are inadequate for the hydrophilic GO. To avoid aggregates, the spreading solution for GO is usually a mixture of water and methanol [81,85]. The interactions between graphene sheets govern the film formation and depend on the balance between the electrostatic repulsion and the Van der Waals attraction. At the first stage of film compression, the GO sheets started to touch each other forming a close-packed monolayer. With the decreasing area, thanks to the flexibility of the single layer, the augmented surface pressure was dissipated as folding and wrinkling of sheets at the touching points (edges) but keeping the interior flat. This edge-to-edge interaction prevents the centre of the GO sheets from wrinkling until there is no space left when the monolayer buckles. With further compression and consequent increase in the Van der Waals forces, the face-to-face interaction led to a reversible flocculation between sheets of similar sizes or an irreversible coagulation between sheets of very different sizes [81]. Following Cote’s pioneering work, Zheng et al. [86] fabricated transparent conductive LB films using ultra-large graphene sheets. Despite the in-plane compression, they discovered that the formation of wrinkling also depends on the evaporation of water molecules. For instance, at a fast substrate-pulling speed, the water molecules become trapped, and their evaporation induces the wrinkling of the sheets. Conversely, small-GO sheets allow easy water evaporation, forming wrinkle-free films.

In 2017, Bonatout et al. [85] investigated GO sheets on an air-water interface by X-ray reflectivity and XRD using synchrotron sources and pointed out that GO spontaneously forms a bilayer of sheets interfaced between air and water by hydrogen-bonded water bridges [85]. Unconventionally, Jaafar et al. [67] have used the LB technique to fabricate 3D reduced graphene oxide (rGO) structures. This was achieved by collecting the film after the

collapse pressure, producing a highly porous surface, which could be tuned by the number of deposition layers.

As a result of the high hydrophilicity conferred by the plenty of oxygenated groups on the GO structure, the accommodation of a variety of moieties is possible and makes GO a functional substrate for anchoring biomolecules to create hybrid nanostructures. The anchoring of nucleic acids [87–90], antibodies [91–93] and enzymes [69] were improved by the use of GO layers. Chalmpes et al. [79] fabricated biohybrid graphene-based structures by conventional and surfactant-assisted LS deposition for further self-assembly deposition of cytochrome c (CYC), as presented in Figure 4A. For the conventional LS deposition, the GO was spread (5:1 methanol: water mixture) onto the air-water interface, compressed to the monolayer formation, and further removed as an LS film. For the surfactant-assisted deposition, octadecylamine (ODA) is spread onto a subphase of an aqueous dispersion of GO. The barrier compression led to the ODA-GO hybrid film formation at the air-water interface, which is collected as an LS film. Further immersion of the substrates into the CYC solution provided the GO-CYC and ODA-GO-CYC films. Atomic force microscopy (AFM) images indicated a smoother distribution and higher coverage in the ODA-GO-CYC LS film (Figure 4B(a) compared to the traditional LS (b)), with the images depicting flakes with well-defined edges and negligible voids between them.

Interestingly, the ODA-GO-CYC presented no catalytic activity. Even with the ODA increasing the interlayer space between GO nanosheets, thus enabling CYC molecules' accommodation, their bulk moieties increase mass transfer limitations during biocatalysis (hampers contact between enzyme and substrate). On the other side, the protein is anchored to the edges of the GO in the GO-CYC LS films, which facilitates the enzyme-protein interaction. Additionally, another reason could be related to hydrophobic interactions between the alkyl chain of ODA and CYC, which could lead to decreased activity.

Miyazaki et al. [91] have compared GO depositions by different techniques for posterior antibody immobilization. Aiming to take advantage of oxygenated groups from the GO structure, GO was immobilized on the gold surface by SAMs of cysteamine and by LB GO films collected on two different surface pressures (15 and 30 mN/m). Although the LB films of GO provided high surface roughness, the transfer of the monolayers to the substrate left uncovered spaces on the gold substrate, which hampered the antibody loading. Also, the microscopy images indicated smaller GO sheets when compared to the self-assembled GO film. This could be due to the fact that the small sheets were able to float at the air-water interface while the large and heavy ones sunk into the subphase. Solanski et al. [66] explored LB films of ordered GO on indium tin oxide (ITO) substrates followed by hydrazine vapor reduction (creating reduced-graphene oxide-rGO) for Dengue detection. Dengue NS1 protein target was detected by the NS1 antibodies covalently linked on the rGO-coated ITO electrodes by electrochemical impedance spectroscopy (EIS) technique. The limit of detection (LOD) achieved was 0.081 ng mL^{-1} in human serum samples, which is convenient since the target antigen level in humans varies from 0.01 to $2 \mu\text{g mL}^{-1}$ in primary and secondary infections.

3.1.2. One-Dimensional Materials (Nanowires and Carbon Nanotubes)

One-dimensional (1D) materials have anisotropic physical properties. It is essential to control their alignment direction to achieve superior properties compared to the randomly oriented structures. For instance, electronic transport is known to be better along the alignment direction than those disordered and cross-linked networks [83,94,95]. Optical, catalytic, and magnetic properties also differ in aligned 1D structures due to the coupling effects and synergetic collective properties in oriented domains [83,96]. Valuable review papers on the alignment of 1D materials have been published by Hu et al. [83], specifically for nanowires by He et al. [97], for carbon nanotubes (CNTs) [46,64,65], and specifically using the LS technique [98].

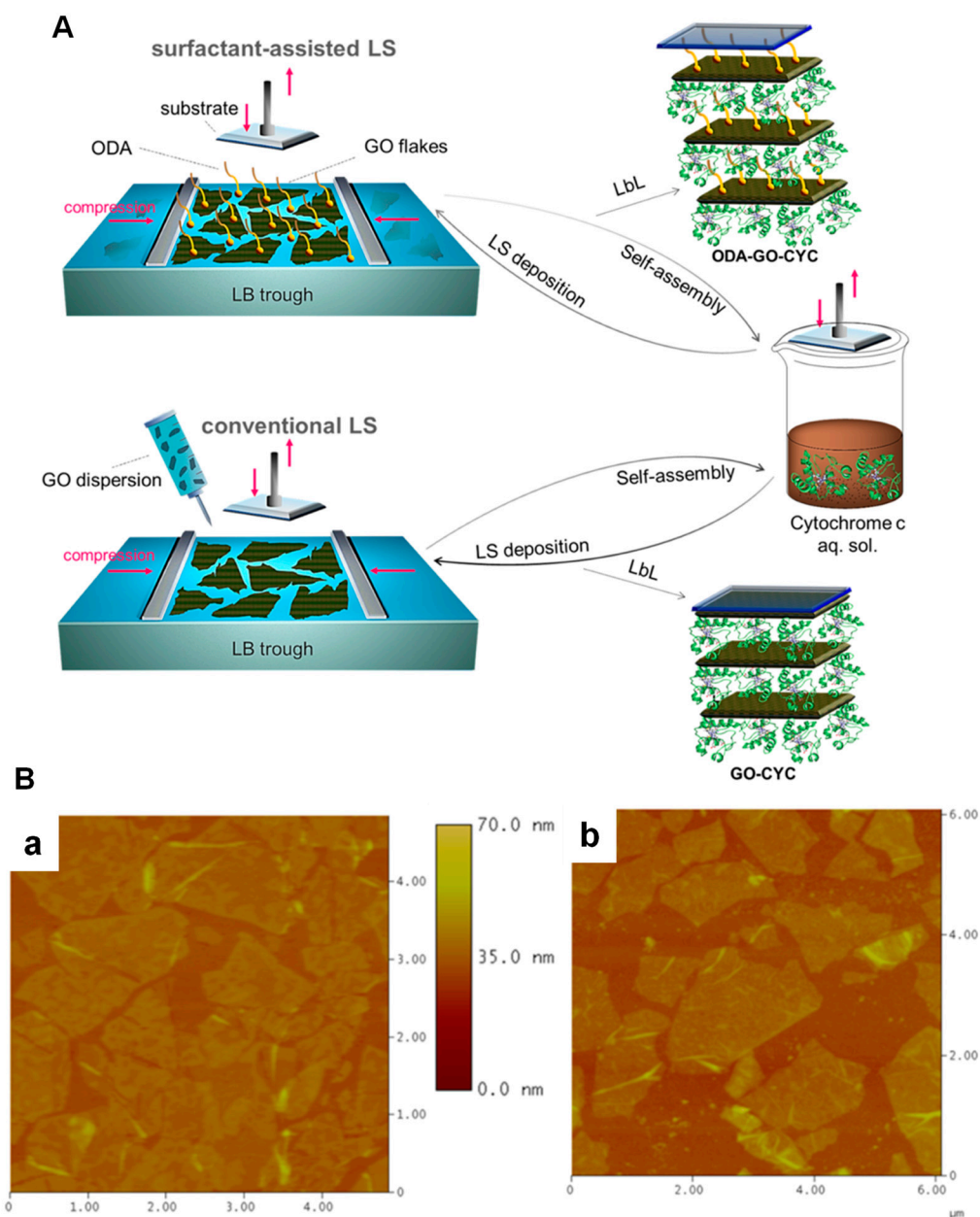


Figure 4. (A) Schematic of surfactant-assisted LS (top) and conventional LS (bottom) depositions followed by the self-assembly deposition of CYC. Multilayered film is formed by repeating the cycle of deposition. (B) AFM height images of ODA-GO-CYC (a) and GO-CYC (b). Adapted with permission from [79]. Copyright 2022 American Chemical Society.

Among the 1D materials, CNTs are one of the most widely investigated in sensing applications due to their interesting optical, electronic, and (electro)catalytic properties [99,100]. CNTs can be immobilized on solid substrates through direct growth or solution processing for sensing purposes. The latter is preferred due to the mild operation conditions (low temperature and pressure) involved and suitability for large-scale production. The alignment of 1D nanomaterials through solution processes is discussed in [101]. The LB technique, a solution-phase processing strategy, offers the advantage of allowing high-density packing [46,101,102]. The first to align CNTs using the LB technique looks to be Li et al. in 2007. Since then, LB and LS techniques have been explored to align nanotubes for sensing applications.

To fabricate LB or LS films of CNTs, they were functionalized or mixed with amphiphilic molecules. Abdulla et al. [63] have functionalized multiwalled-CNTs (MWCNT)

with polyaniline (PANI@MWCNT) to be spread on the Langmuir trough (Figure 5A). The barrier compression led to the formation of well-aligned structures, and the horizontal or vertical dipping of the substrate originated the LS or LB films, respectively. Figure 5B illustrates the TEM images and the corresponding phases in the compression isotherm from the gaseous state (a), liquid-expanded (LE) (b and c), liquid-condensed (LC) (c), and solid (S) (d) states, with the CNTs oriented parallel to the barrier. An application as a chemoresistive NH₃ gas sensor presented 2-fold superior performance compared to spin-coated sensors. It is believed that the aligned PANI@MWCNTs created an easy pathway for the NH₃ gas interaction and facilitated electron transport through the ordered network [63].

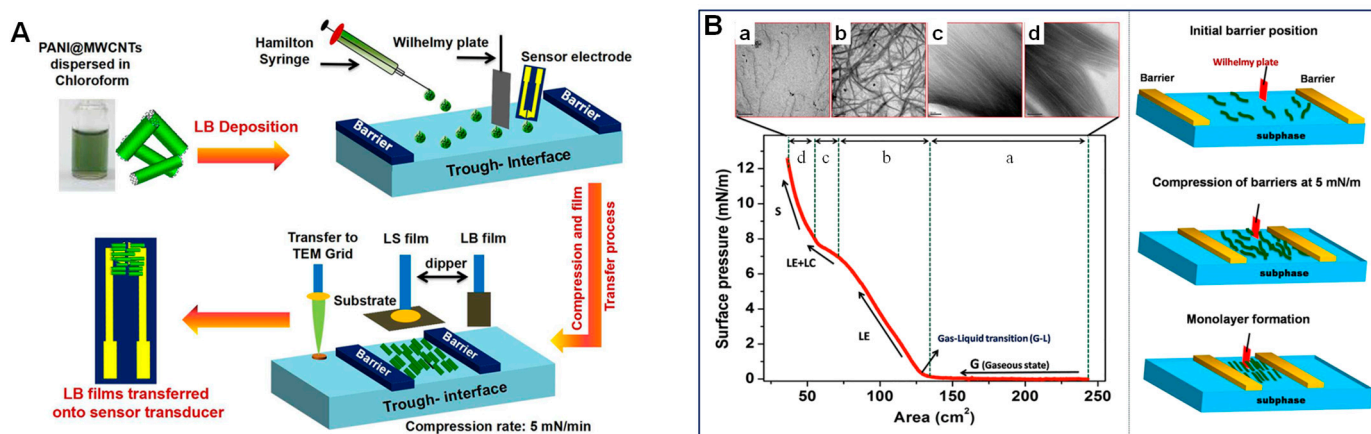


Figure 5. (A) Schematic of LB assembly of PANI@MWCNTs on sensor transducer. (B) π -A isotherm of PANI@MWCNTs at the air-water interface and corresponding TEM images for each phase (a–d) and representation of the formation of aligned structures at the air-water interface with the barrier compression. Adapted with permission from [63]. Copyright 2020 American Chemical Society.

Vertically aligned CNTs are also possible through the LB technique. Wang et al. [96] developed a method using ODA. Firstly, ODA was spread onto the trough, and after solvent evaporation, a first compression would leave a layer of ODA molecules floating with some bevel angles. Then, after a careful spreading of MWCNT, an hour is lasted to allow ODA and MWCNTs to enwind each other to finally compress the barriers. The electrochemical sensor was tested for methylparaben after transferring it to a glassy carbon electrode (GCE). The best electrochemical performance was achieved with two layers of MWCNTs. The possible reason is that the second one supplemented some imperfections left by the first deposited layer. Adding a third layer augmented the film resistance caused by the non-conductive ODA. The GCE/MWCNTs voltammetric sensor presented a linear range of 1×10^{-6} to 8×10^{-5} mol L⁻¹ and a LOD of 4×10^{-7} mol L⁻¹. The same group used a similar approach with PANI-CSA (polyaniline base doped with camphor sulphonic acid) to produce PANI-vertically aligned MWCNTs (MWCNTs-PANI-LB/GCE) [84]. The electrochemical investigation in the probe solution revealed the charge transfer resistance decreasing from MWCNTs-PANI-LB/GCE < MWCNT/GCE (dropcast) < bare GCE. This was reflected in the daidzein detection, widely used in treating cardio-cerebrovascular diseases. Compared to the randomly dispersed MWCNTs, the MWCNTs-PANI-LB/GCE presented a wider linear range (1×10^{-7} – 9×10^{-6} mol L⁻¹) and a lower LOD of 8×10^{-8} mol L⁻¹ [84].

The sensing application of nanowires (NWs) has also been explored. However, to take advantage of their 1D nature (i.e., almost monocrystalline perfection, atomically sharp termination, and small diameter, close to the electron confinement limit), the orientation of NWs must be controlled. ZnO nanowires-based LB/LS films demonstrated interesting gas-sensing properties [48,95]. As a result of the high hydrophilicity of the ZnO nanowires, a functionalization with amphiphilic surfactants is needed to allow their floating at the air-water interface, as with palmitic acid [95] or 2-dodecanthiol [48]. Baratto et al. [95] worked on the Langmuir film formation with the NWs parallel to the barrier, which was further

collected by the LS technique onto Au electrodes. Annealing was performed to improve the contact between NWs and Au electrodes and to remove the palmitic acid. The aligned ZnO-NWs sensor was suitable to detect NO₂ either at 200 °C or at room temperature, while the drop cast film (random orientation) presented no correlation between relative response and NO₂ concentration. Without orientation, there is a strong dependence on the response with the percolation through the interconnections between the NWs, which depends on the preparation conditions.

Concerning NWs, the possibility of creating aligned structures is of great interest to SERS researchers. Pioneering work of Tao et al. [103] in 2003 used the LB technique to fabricate aligned AgNWs film. The NWs with pentagonal cross-section and pyramidal tips were previously capped with poly(vinyl pyrrolidone)—PVP to turn the NWs' surface hydrophobic, thus preventing aggregation. The formed AgNWs monolayer became well-aligned parallel to the barrier, and the LB film was transferred to a silicon wafer for SERS application. The enhancement factor was 10⁵ and 10⁹ for 2,4-dinitrotoluene and Rhodamine 6G, respectively. Recently, Sheng et al. [104] have fabricated ordered LB TeNWs film to further immerse in H₂AuCl₄ aqueous solution. After the reduction, the ordered Te-Au hetero NWs film was tested as a SERS substrate. The enhancement factor using 3,3'-diethylthiatricarbocyanine iodide (DTTCI) as a probe was calculated as ~10⁶ and ~10⁵ for the ordered and disordered (dropcast film) SERS substrate, respectively. Due to the orderly and close arrangement of the plasmonic gold nanoparticles (AuNPs), there is a greater number of hot spots in the ordered film, while in the disordered one, the AuNPs are dispersed (far apart from each other). Additionally, the Te-Au hetero NWs film exhibits excellent uniformity and flexibility. Interestingly, a test using a polarized laser indicated that the local field that dominates the SERS signal is perpendicular to the NW template in the axial direction, while the intensity is independent of the angle of polarized light for the disordered film [104].

3.1.3. Nanoparticles

Regarding sensing platforms based on the surface plasmons, for instance, SERS, which is based on localized surface plasmon resonances (LSPR), and SPR (surface plasmon resonance) sensing approaches, the deposition techniques through monolayers are interesting due to the possibility of controlling the nanoparticles organization and the packing density by means of adjustment of the moving barriers. Although this message sounds very appealing from the perspective of various sensing applications, achieving a high degree of surface coverage of metal nanoparticles is still a challenge. Swierczewski and Bürgi [59] have discussed the differences between manufacturing films of purely hydrophobic metal nanoparticles to typical amphiphilic molecules. The absence of hydrogen bonds to stabilize the Langmuir layer introduces the main challenge to ordering and transferring the films [59]. Experimental conditions such as the chosen capping ligand (length and chemical nature, their density on the metal core) influence the steric repulsion and the Van der Waals attractions between the particles. Effects such as affinity between the capping ligand and the spreading solvent are also relevant.

The possibility of tuning the hot spots during the fabrication of the plasmonic architectures has attracted attention to the subject of SERS [60,61,105–107]. While the conventional self-assembly method provided a limited surface coverage (~50%) as a result of the steric hindrance [108], the LB deposition allowed much higher coverage of Au nanoparticles due to the controllable surface pressure of the monolayer (above 90% for spherical nanoparticles) [109,110]. An alternative approach in which the metal ions are adsorbed on the top of an organic Langmuir monolayer for further photoreduction also provided significant surface coverage (76%), as well as the use of LB films of silica nanoparticles followed by gold sputtering [111,112].

Tahghighi et al. [60] created a SERS substrate through AuNP monolayers at the air-water interface. Nanoparticles were capped with 1-dodecanthiol and PEG-SH to prevent aggregation. The excess (non-adsorbed) PEG-SH was removed by centrifugation before sus-

pension in chloroform and spreading. The monolayer was transferred to a (3-aminopropyl) triethoxysilane (APTES)-modified substrate and used as seeds for electroless deposition of Au. A probe molecule (4-mercaptobenzoic acid, 4-MBA) was dropped on the substrate to analyse the SERS performance. The SERS intensity increases with the lateral pressure, corresponding to an increase in particle density, until it reaches a maximum at the pressure of $\sim 13 \text{ mN m}^{-1}$ (corresponding to the limit of the monolayer stability). Progressive compression leads to the collapse of the monolayer, multilayered aggregates, and decreased signal [60]. For the Au nanostars, the maximum amplification was found in films deposited at 10 mN m^{-1} , lower than in the spherical ones since high packing densities may cause interdigitation between neighbouring nanostars [61].

Turning our attention to the use of the LB technique in the fabrication of magnetic nanoparticle films, it is worth noting that this subject remains understudied due to the self-aggregation process, which limits the suspension stability. Pandey et al. [113] presented the coating of iron oxide nanoparticles (IONPs) with poly(lactic-co-glycolic acid)—PLGA to provide stability and active sites for the immobilization of antibodies against *E. coli* O157:H7. The EIS-based sensor provided a LOD of 3.0 CFU mL^{-1} . In a study developed by Khasraw et al. [114], the application of an external magnetic field during the fabrication process of the monolayer of stearic acid-capped IONPs improved the packing density of the nanoparticles. It is possible to form striped structures aligned to the direction of the external magnetic field [114].

3.1.4. Other Materials

Due to the fashionable molecular organization, countless materials have been applied to sensing platforms and fabricated by the LB or LS techniques. Due to space limitations, we have chosen to discuss a bit about porphyrins, phthalocyanines (Pc), and biomolecules.

Porphyrins and Pc are largely investigated due to their stimuli-responsive properties. Katsuhiko Ariga has particularly reviewed the LB and the LbL strategies to fabricate films of porphyrins and related molecules [115]. Maximino et al. [116] have highlighted the versatility of fabricating thin films of metallic Pc through different techniques (LB, LS, LbL, PVD, and electrodeposition). Concerning the use of a Langmuir trough, the rigid nature of the pristine porphyrin floating monolayers appeared to hamper the transferring by the LB technique in some cases, and most works have used the LS transferring method [117–120]. Bettini et al. [117] tested three bis-porphyrin compounds (metal-free, Ni, and Co complexes) LS films for histidine detection. A previous interaction study with the Langmuir monolayer revealed that the interaction with the amino acid promotes conformation changes in the porphyrin, with an important role of the central metal ion [117]: a partially closed structure for NiNiPo₂ (tweezer structure) and an opened *anti*-conformation for the CuCuPo₂. By SPR, which is based on changes in the local refractive index very close to the sensing surface [121], the angle of minimum reflectivity varied as a function of the histidine concentration, with two ranges of linearity: 10^{-9} to 10^{-6} and 10^{-6} to 10^{-4} M. The same research group developed a sensor for chiral discrimination between L- and D-histidine through an LS film of cubane-bridged bisporphyrin (H₂por-cubane-H₂por). Again, the sensor is based on conformation changes provoked by each one of the chiral structures: L-histidine promotes the stabilization of the anti-conformer of the porphyrin molecules, while D-histidine promotes the tweezer conformation [118].

Phthalocyanines (Pc) electroactive and electrocatalytic properties have also attracted interest in developing electrochemical sensors [10,11,120,122,123]. Ermakova et al. [119] prepared LS films of porphyrin-5-ylphosphonate diesters for mercury(II) ions. To the monolayer formation, the π stacking was avoided by the bulky diethoxyphosphoryl and mesityl groups, chemically introduced for this purpose. The selectivity of the dual sensor (absorbance and fluorescence) composed of 10-layer LS film is based on the coordination of the interfering metals (Cu²⁺, Zn²⁺, Cd²⁺, and Pb²⁺) to the donor heteroatoms at the periphery of the macrocycle. The LOD of this reusable thin-film (tested over six cycles) sensor is $\sim 10^{-8}$ M. Akyüz and Koca [120] combined the LB technique to electrochemical

deposition to fabricate a sensor for pesticides. An LB film of terminal alkynyl substituted manganese phthalocyanine (MnPc-TA) film was assembled on ITO electrodes for further 4-azidoaniline (N₃-ANI) reaction to the MnPc-TA alkynyl groups. Finally, the hybrid MnPc-TA/N₃-ANI film was electropolymerized to be tested as an electrochemical sensor for fenitrothion, eserine, and diazinon. By the square-wave voltammetry, the sensor was selective only for fenitrothion, with a LOD of 0.049 $\mu\text{mol dm}^{-3}$.

Biomolecules have also been applied by the LB technique. One of the main features can be attributed to the LB films of enzymes, which keeps their activities (if not improved) for longer periods compared to the homogeneous suspension [70,71]. Usually, a matrix of phospholipids provides a friendly environment for the biomolecules. For that, the lipid monolayer is formed at the air-water interface to further enzyme adsorption (from subphase [69], injected into the water subspace after the spreading of the lipid [70] or injected below the formed lipid monolayer [71,124]). This allows the enzyme to adapt, reaching the minimum free energy to conserve its secondary structure and thus preserve its catalytic property [125]. Additionally, the combination of enzymes with conjugated polymers to provide structural conservation and improved energy transfer in sensing applications was also explored [75,126].

Regarding biosensing applications, Scholl et al. [69] have investigated the enzymatic activity of penicillinase (PEN) in lipid LB films in the presence of GO. For the Langmuir film formation, the lipid dimyristoylphosphatidic acid (DMPA) was spread at the air-water interface on a subphase containing GO and the enzyme. Additive shifts to higher areas for PEN and GO were verified (compared to pristine DMPA monolayer), indicating their interpenetration on the DMPA monolayer. The synergy between the compounds leads to a suitable molecular accommodation that preserves PEN activity [69].

3.2. Layer-by-Layer Assembly

Since its introduction by G. Decher in 1992 [127], the Layer-by-Layer (LbL) technique has garnered significant attention for manufacturing thin films. It is a straightforward way to create multilayered films through sequential and spontaneous adsorption of materials that interact via Coulomb interactions, hydrophobic forces, Van der Waals forces, and hydrogen bonds [128]. The LbL technique enables precise control of molecular-level thickness through experimental parameters. At the same time, its versatility allows for the functionalization of surfaces with unlimited size and shape, making it an interesting approach to develop new functional thin films exhibiting a synergistic combination of properties.

The traditional immersive LbL assembly, described in Figure 6, relies on the spontaneous adsorption of materials onto a solid substrate submerged in a stable aqueous suspension. Following each immersion, the substrate undergoes washing to remove any weakly adsorbed material and prevent cross-contamination. It is optional to perform a drying process (naturally in air or by nitrogen) after each step of immersion and washing. The thickness can be easily regulated by controlling the number of deposited layers. Combining two, three, or four different materials can create supramolecular arrangements with bi-, tri-, quadrilayers, or even more, as desired.

About the requirements to manufacture a thin film through the LbL technique, the substrate may be hydrophilic and preferably charged. Fortunately, functionalization strategies are available for practically all surfaces of interest to precede the LbL assembly. For instance, Au surfaces can be modified with SAMs of thiolated molecules to acquire charged functional groups: 11-mercaptopundecanoic acid, 1-octanethiol, and 6-mercapto-1-hexanol are common reagents to provide negatively charged surfaces via carboxyl or hydroxyl groups. At the same time, cysteamine and APTS (a silane coupling agent) are employed to surface functionalization with positive amine groups. Silica surfaces (as common substrates of glass and quartz) can be cleaned to exhibit their natural hydrophilicity and negative charges [129] or can be plasma activated and/or by the APTS method [130]. Other oxides, such as titanium oxide, iron oxides, ITO, and fluorine-doped tin oxide (FTO), can also be modified by APTS [130]. Another important point is that the materials of interest should

be suspended in a homogeneous and stable aqueous dispersion, even though the LbL deposition using organic solvents has already been reported [131,132].

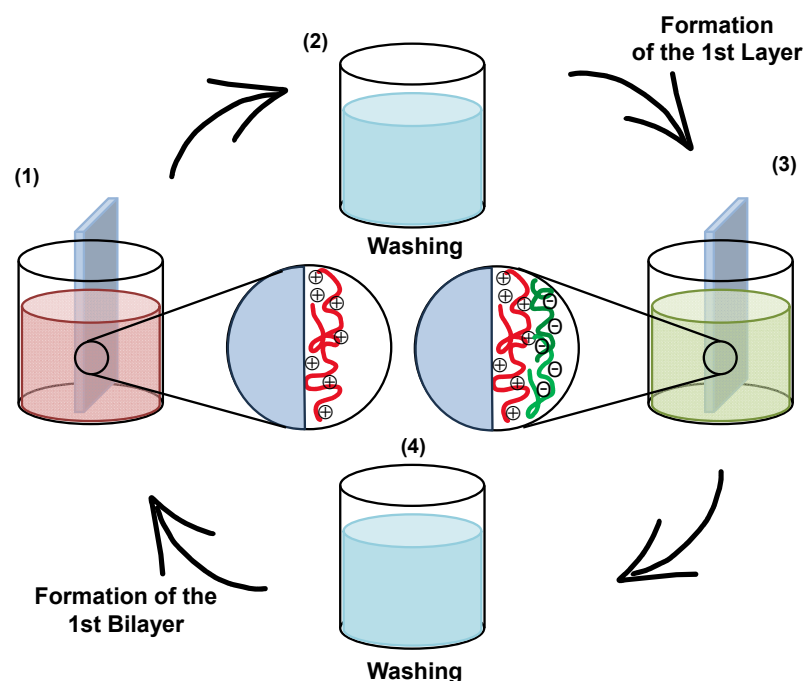


Figure 6. Schematic of the LbL fabrication: (1) a negatively charged solid substrate is immersed in a suspension with positively charged material; (2) a washing is performed to remove weakly adsorbed material and avoid cross-contamination; (3) the substrate is immersed in a negatively charged suspension; (4) the washing process is repeated to allow removing of the weakly adsorbed material. A first bilayer is formed.

Although initially proposed for charged polyelectrolytes, the LbL technique can be applied to a wide range of materials, including metal nanoparticles, carbon-based materials, and biomolecules. The LbL nanostructured films exhibit excellent stability and unique properties, thus finding widespread use in the development of various electronic and optical devices, such as energy generation and storage devices [133–135], as well as sensors and biosensors [134–136].

Other LbL approaches are possible, such as spraying, spinning, and fluidic assembly. However, we focus here on the traditional immersive self-assembly. More details about the alternative LbL approaches can be found in [137,138]. The manufacture of sensors usually accomplishes the modification of flat surfaces. However, another application that should be mentioned here is the importance of the LbL assembly in colloids, especially in developing drug delivery systems. More information on this theme can be found in recently published review papers [139–141].

3.2.1. Graphene-Based Materials

The first study on LbL assembly of graphene dates from 2009 [142]. Shen et al. [142] started with GO exfoliation to avoid graphene aggregation in an aqueous solution. GO was further reduced and stabilized with poly(acrylic acid) (PAA) and poly(acryl amide) (PAM), which introduced negative and positive charges on the graphene surface, respectively, allowing the electrostatic LbL assembly. Since then, graphene derivatives have been largely explored in LbL films. rGO is conductive and greatly applied to improve the charge transfer between specific sensing reactions and the electrode. At the same time, the abundance of oxygenated groups of the oxidized form (GO) enables improved biomolecule loading to biosensing applications, which also allows improved sensitivity [92,143].

The conductive property is the most sought-after for application as electrical and electrochemical sensors [144]. However, the conductive form possesses the sp^2 carbon network, which is hydrophobic and non-water soluble, hampers the LbL assembly of its pure form. Therefore, LbL films of graphene nanoplatelets originate from aqueous exfoliation of GO and follow two alternatives: (1) chemical reduction prior to the LbL assembly, usually functionalized or stabilized in charged polyelectrolytes to keep a stable aqueous suspension [145–147]; (2) chemical [148], electrochemical [149–151] or thermal reduction [152–154] post-assembly of LbL film of GO, which is applied as the negatively charged material multilayered with a positively charged material.

Due to its solubility in water and the easy functionalization with polyelectrolytes, GO has been combined with an infinitude of functional materials in aqueous media to stabilize the reduced form to allow the manufacture of LbL films. Rodrigues et al. [145] prepared stable dispersions using two polyelectrolytes, positively charged poly(diallyldimethylammonium chloride) (PDDA) and negatively charged poly(styrenesulfonate) (PSS), to subsequent chemical reduction with hydrazine, leading to the formation of rGO stabilized in PDDA (GPDDA) and in PSS (GPSS). The LbL films of (GPDDA/GPSS)₁₀ and an alternative arrangement containing PAH stabilized-AuNPs ((GPDDA/GPSS)₁(AuNP-PAH/GPSS)₁₀) were assembled on ITO electrodes and evaluated as an electrochemical sensor for the pesticide methyl parathion (MP). Raman spectroscopy of these films indicated the D' band (absent in bulk material) assigned to surface graphene layers (not sandwiched between two other layers), indicating the successful assembly of well-exfoliated graphene layers. While there was a homogeneous distribution of MP molecules on the LbL film with the AuNPs, the analyte was preferentially adsorbed on the graphene aggregates on the film without AuNPs. The lower LOD by the (GPDDA/GPSS)₁₀ film was justified by the facilitated charge transfer provided by the proximity of MP and graphene, while the wider linear range by the sensor with AuNP in the composition would be related to the higher analyte distribution (more interaction sites) [145].

Unlike Rodrigues et al. [145], Al-Hamry et al. [152] produced PANI/GO LbL films to perform a further thermal reduction. Likewise, Miyazaki et al. [149] performed an electrochemical reduction after depositing alternating PDDA and GO layers. In the face of the possibilities of reducing GO films, it is necessary to consider that chemical reduction requires reagents for the reduction and stabilization of nanosheets but allows control of the functionalization in suspension, whereas thermal and electrochemical reduction are reagent-less processes but require heating and the application of a reduction potential, respectively. Heat or applied potential is inherently applied to the entire film and can alter the morphology and eventually compromise the integrity of polyelectrolytes/material assembled GO.

LbL films of GO have also encountered applications in sensor development due to their planar structure and/or the oxygen-containing functional groups [92,144]. For instance, Oliveira et al. [143] deposited alternate layers of PAH:GO and PANI:poly(2-acrylamido-2-methyl-1-propanesulfonic acid) on a p-Si/SiO₂ chip. This LbL film was used as a support layer to immobilize urease and penicillinase enzymes separately for later application as urea and penicillin sensors. The LbL film provided a better adhesion of the enzymes and an increased number of sensor units (bioreceptors) due to the rougher active surface area. A 15% improvement in the average sensitivity was achieved with the LbL film modification.

3.2.2. Phthalocyanines (Pc)

Metal tetrasulfonated phthalocyanines (MTsPc) are water-soluble and versatile molecules with supramolecular properties that make them suitable for LbL deposition [116]. Typically, sulfonic groups in the MTsPc structure provide both water solubility and negative charges to the LbL assembly. FeTsPc [155], CuTsPc [156,157], and NiTsPc [158–161] were applied as an anionic material as alternated layers with a cationic polyelectrolyte such as PAH or poly(ethylene imine) (PEI). Thus, the supramolecular arrangement of LbL films with Pc derivatives can be evaluated based on factors such as LbL composition [161], the number

of bilayers [155,156], pH of the solution [162], and by the combination with other materials such as nanoparticles [157–160,163] and carbon materials [164,165].

Hybrid materials based on Pc and metal nanoparticles are widely explored for the development of electrochemical and chemiresistor sensors [166]. The incorporation of AuNPs in LbL film showed an increase in electron transfer due to the interaction of $-\text{NH}_3^+$ from PAH and $-\text{SO}_3^-$ from MTsPc, which improves the catalytic property for electrochemical sensing of propylparaben [159], tartrazine [158], and pesticides [157,161]. Although the LbL assembly depends on the electrostatic attraction between the composite layers (namely, between MTsPc and NPs), the MTsPc can also be LbL assembled based on coordination via oxo bridges [160]. Ribeiro et al. [160] described significant changes in UV-vis absorption spectra as well as the shift in Raman bands of NiTsPc after LbL deposition with IONPs, ascribing to the mutual electrostatic and covalent interaction (Ni(II)-O-Fe(III) oxo bridges). The unusual supramolecular arrangement allowed the electrocatalytic oxidation of ethinyl estradiol (EE2), which was impossible with the NiTsPc or IONPs alone [160]. The detection of EE2 was also evaluated by LbL films of MWCNTs and different MPcs (FePc, MnPc, and CoPc) [164]. The oxidation performance depended on the metal centre, with the higher oxidation achieved by CoPc [164]. The LbL combination of Pc and carbon-derived materials is also promising in sensing applications [164,167]. Besides, the incorporation of Pc in LbL films is also explored for the development of biosensors [167,168].

3.2.3. Metal Nanoparticles

Metal nanoparticles (MNPs) have been effectively incorporated into sensor development through the LbL technique. As a result of their conductive and electrocatalytic properties, MNPs are widely explored for electrical and electrochemical sensors. Due to their plasmonic properties, Au, Ag, and Cu NPs are leveraged to develop optical sensors, especially plasmonic ones.

MNPs are determining components of hybrid systems. Electrochemical sensing applications take advantage of the electrocatalytic property, augmented surface area, and reduced charge transfer resistance promoted by the MNP-modified electrodes. MNPs usually come combined with other nanomaterials as Pc [157–159,163,168], carbon-based materials [145,165,169,170], clays [171,172], ionic liquids [168,173], among others. In addition, MNPs have been combined with biomolecules for biosensing applications [169,174–177]. To contextualize, Salvo-Comino et al. [178] have combined materials with complementary functionalities by the LbL technique to build an enzymatic sensor for catechol: Pc as an efficient electron mediator, the ionic liquid to improve the conductivity of the film, and chitosan to create a suitable environment to the enzyme. They obtained a LOD at the nanomolar level, which was lower than other assemblies found in the literature using LbL, LB, and SAM approaches.

AuNPs are the most used mainly due to their chemical stability and facile surface functionalization. Stable suspensions for the LbL assembly are usually achieved under reduction by polyelectrolyte stabilization [145,165,179–181], ionic liquids [173], glutathione [175,177], and citrate [89,182]. These stable suspensions can be applied as a component of the LbL assembly combined with opposite-charged polyelectrolytes, nanomaterials, or ions. Another approach is the immobilization of the AuCl_4^- anionic precursor onto the LbL assembly to further reduction. This can be carried out by the adsorption of the ionic precursor onto a pre-formed polyelectrolyte multilayer film [179,183] or by mixing AuCl_4^- ions with polyelectrolytes to the LbL assembly [184,185] prior to the reduction.

Regarding optical sensor applications, the modification of optical fibre aiming LSPR sensing has been recently reported [179,181,182,186]. The LbL technique allows the easy and controllable assembly of AuNPs and AgNPs on the optical fibre surface providing the LSPR signal (plasmon absorption band), which is sensitive to changes in the refractive index of the surrounding medium. Another optical sensing approach is centred on the fabrication of SERS substrates [187–190]. Highlights for the possibility of easily combining

graphene and plasmonic particles uniting the fluorescence quenching of GO and signal enhancement from MNPs for SERS detection [188,189].

Mariani et al. [191] described the LbL assembly of the positively charged PAH and negatively charged citrate-capped AuNP on porous silicon (PSi) interferometers and distributed Bragg reflectors (DBRs) (Figure 7A). The PAH/AuNP assembly enhanced the Fraby–Pérot fringe contrast due to the increased reflectivity (Figure 7B). The morphology of the LbL-modified PSi with AuNPs with 15 and 4 nm sizes were depicted in Figure 7C and Figure 7D, respectively. Cross-sectional SEM and EDS analysis of PSi interferometers allowed verify that the smaller AuNPs (4 nm) efficiently decorated the inner porous while the 15 nm-AuNPs poorly penetrated the inner surfaces [191]. The sensing capability was evaluated by IAW (interferogram average over wavelength). Bulk and surface refractive index sensing were assessed, resulting in a 4.5-fold increase by NaCl infiltration and a 2.6-fold increase by bovine serum albumin (BSA) adsorption to the modified PSi. Figure 7E presents the sensorgram of IAW–IAW₀ (average value of the spectral interferogram upon the subtraction of the reflectance spectrum recorded after the injection of NaCl and the reference reflectance spectrum recorded in buffer) over the injection of different refractive index patterns. The corresponding calibration curve is illustrated in Figure 7F. This PSi/PAH/AuNP interferometers demonstrated sensitivity by both photonic (DBR stop-band) and plasmonic (LSPR) peaks to changes in the refractive index promoted by bulk and surface changes [191].

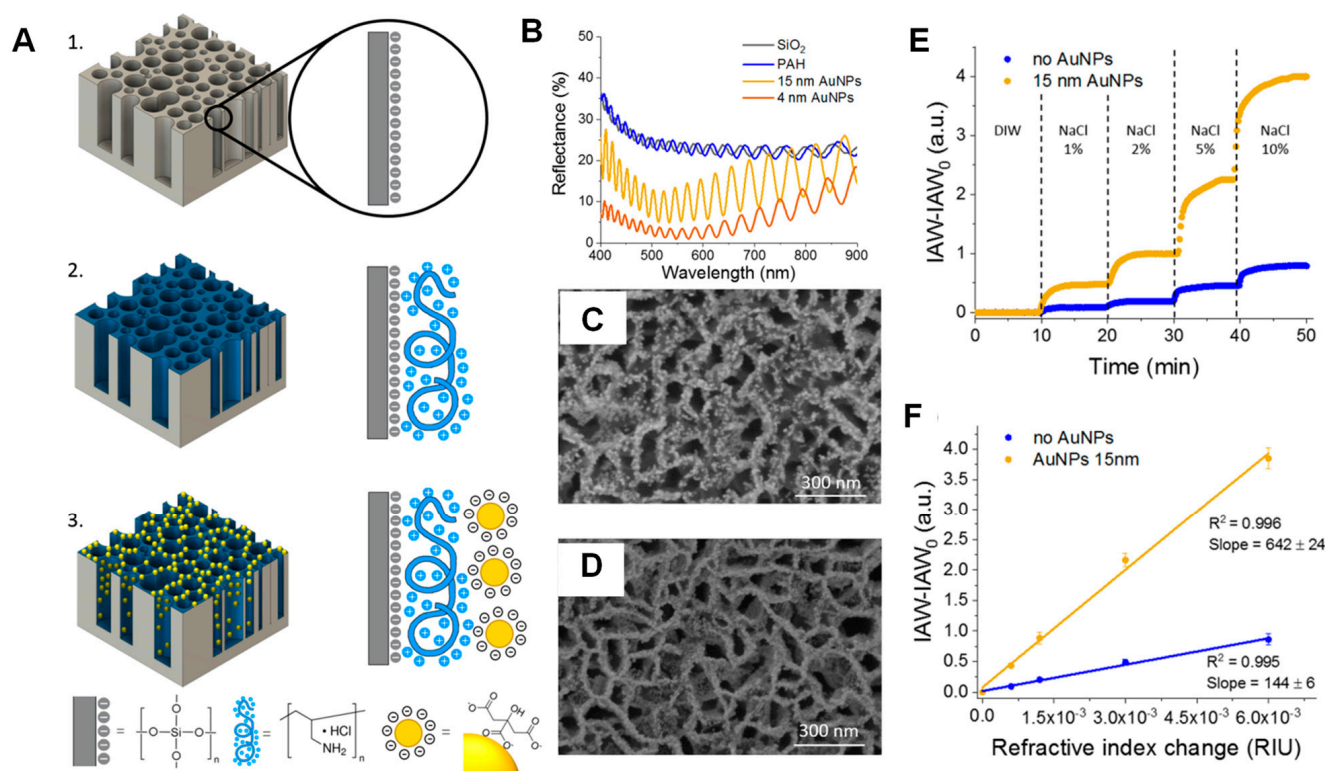


Figure 7. (A) Illustration of the LbL assembly steps of PAH/AuNP onto PSi interferometers: 1. Oxidation of PSi to provide a net negative charge. 2. PAH layer (blue, positively charged). 3. Citrate-capped AuNP layer (yellow, negatively charged). (B) Reflectance spectra recorded in the air of PSi interferometers after oxidation, PAH deposition, and 15 and 4 nm size AuNP deposition. Top-view SEM images of PSi/PAH/AuNP (with 15 nm (C) and 4 nm (D) AuNPs). (E) Sensorgram IAW–IAW₀ vs. time following the NaCl injection (1, 2, 5, and 10%) on nondecorated and 15 nm-AuNP decorated PSi interferometers. (F) Calibration curve IAW–IAW₀ in function of the refractive index from (E). Adapted from [191] under the ACS AuthorChoice License.

3.2.4. Biomolecules

Immobilizing proteins and other biological molecules on solid substrates by the LbL technique is advantageous due to the ability to maintain controlled conditions such as pH and temperature and entrapment of water molecules between the layers [192]. Although it is not common to have studies describing the molecular organization of LbL films, there is generally an investigation into the relationship between the number of layers or another experimental parameter with the sensor performance. In general, the sensitivity increases with the number of layers (with the augmented loading of biomolecules) until reaching a maximum, followed by a plateau or even a decrease [193,194] caused by the limited diffusion and/or hindered electron transfer in thick films [195]. So, the sensitivity can be tuned by the number of layers.

The LbL approach can be utilized to form multilayered structures of biomolecules, as enzymes [147,195,196] or antibodies [197], or also used to build a matrix layer to preserve the activity of biomolecules when immobilized as solid films [136,147,195,198,199]. The LbL technique also enables the possibility of achieving a synergistic effect by combining different materials. For instance, they can bring together the electrocatalytic property of carbon materials for electrochemical sensing [200,201] and an adequate environment for the biomolecule's immobilization [198,202,203]. Chitosan, a biocompatible polysaccharide found in crustacean shells [204], is commonly used as a positively charged polyelectrolyte to build LbL matrices able to maintain the biomolecule activity [201,202,205].

Regarding immunosensors, electrochemical sensors based on LbL films as a support for antibody immobilization have been described [175,199,206]. Multilaminate composite films were fabricated by negatively charged AuNPs and positively charged Fc@MgAl-LDH (MgAl layered double hydroxides containing ferrocene-carboxylic acid) and used as a support for antibody anchoring and detection of cancer biomarkers [199,206]. Zhang et al. [206] have used (AuNP/Fc@MgAl-LDH) films for electroluminescence (ECL) detection of prostate-specific antigen (PSA) through a sandwich immunoassay. In this immunosensing approach, a primary (or capture) antibody is immobilized on the solid surface and works capturing the antigen from sample, and another antibody called secondary antibody, which is labelled and binds to the antigen-antibody complex, providing the detectable signal [207]. The film (AuNP/Fc@MgAl-LDH) was used to immobilize the primary antibody. After incubation with the target PSA, a label composed of luminol and a secondary antibody (Ab₂) supported on a metal-organic framework (MOF) was left to incubate on the surface. The optimum response was achieved with 12 bilayers-(AuNP/Fc@MgAl-LDH) film. The synergy between the materials in the LbL assembly was crucial: MgAl-LDH provided an ideal microenvironment for the uniform immobilization of Fc while the Fc carboxyl groups allowed the Ab anchoring and the AuNPs were responsible for improving the electron transfer of the system. Finally, the peroxidase-like catalytic activity of MOF-supported Ab₂ and luminol improved the ECL intensity to detect PSA.

As an interesting example of an LbL-based enzymatic sensor, Welden et al. [203] have developed a field-effect biosensor (Figure 8A) for penicillin through the modification of an electrolyte-insulator semiconductor capacitor (EISCAP) with an LbL film of PAH and TMV_{Cys-Bio} (Tobacco Mosaic Virus exposing cysteine residue and biotinylated). Following this, streptavidin-functionalized penicillinase was anchored to build the sensor. Compared to a surface in the absence of PAH (direct immobilization of TMV_{Cys-Bio}), the LbL assembly provided a higher surface coverage (Figure 8B) thanks to the partial neutralization of the negative net charge of the TMV particles provided by the PAH layer, thus diminishing the Coulomb repulsion between neighbouring tubes. Since the operation principle of the sensor is based on the local pH changes (the enzymatic reaction produces protons), the signal was firstly assessed for various pH (Figure 8C) and then for penicillin (Figure 8D).

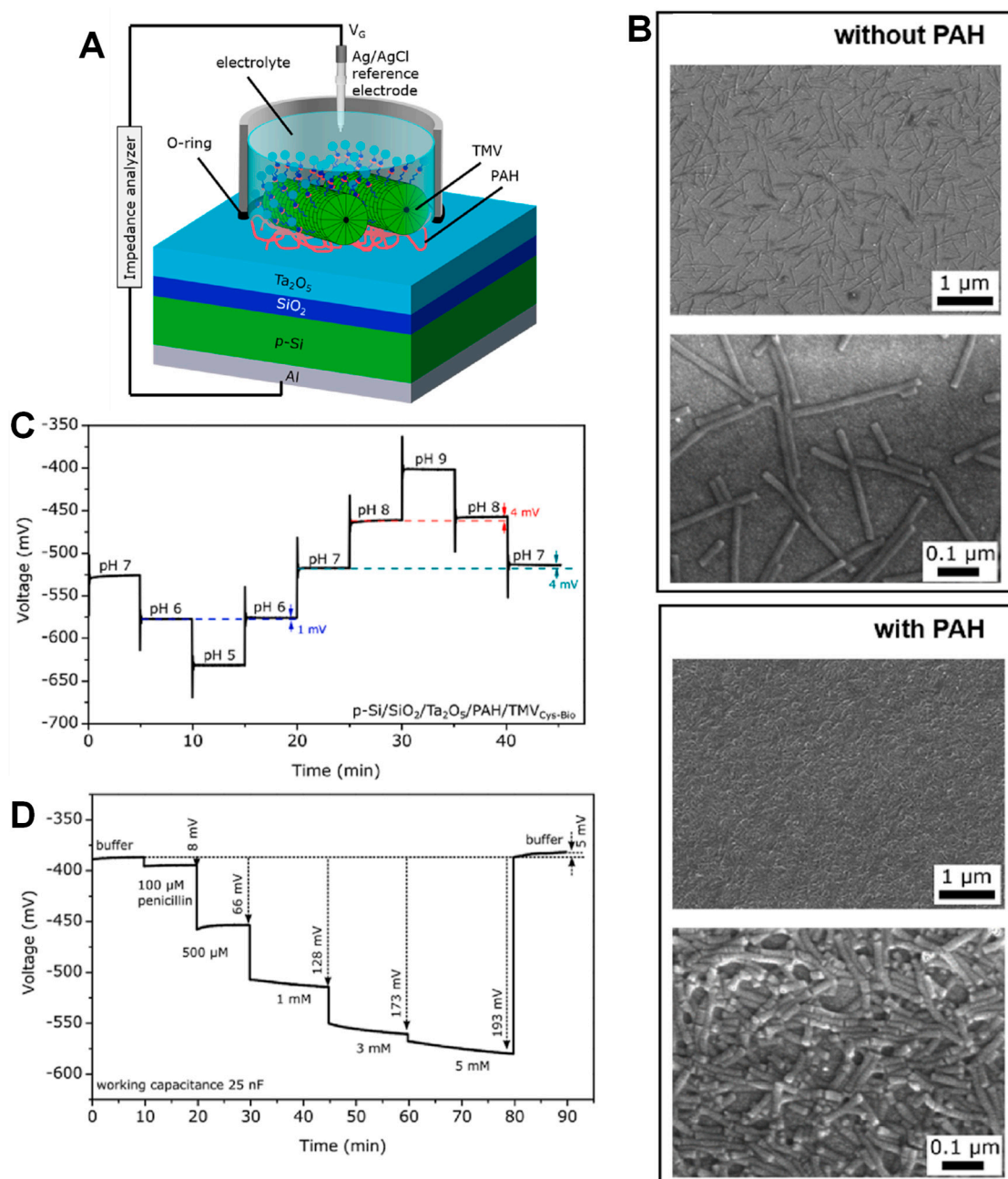


Figure 8. Scheme of (A) the modified Al/p-Si/SiO₂/Ta₂O₅ EISCAP with the LbL deposition of PAH and TMV_{Cys-Bio} (TMV exposing cysteine residue and biotinylated) followed by streptavidin-functionalized penicillinase. (B) Comparison of the surface coverage in the presence of PAH in the LbL structure and its absence by direct immobilization of TMV_{Cys-Bio} observed by SEM images in two different magnifications. Sensing responses for (C) different pH values between 5 and 9 and (D) penicillin solutions with different concentrations from 0.1 mM to 5 mM. Reprinted from [203]. Copyright 2023, with permission from Elsevier.

3.3. Electrochemical Deposition

Electrodeposition (ED) is a technique used to modify a conductive substrate, coating it with a thin layer of a specific material through an electrochemical process. It involves the use of an electrolytic cell, and the material deposition is performed based on the principle of electrolysis [208,209]. Through a controlled potential, during the redox reaction (oxidation or reduction), the material is deposited at the conductive substrate surface as a film. The success of ED depends on several factors, including the composition of

the electrolyte solution, the electrical current and voltage applied, the duration of the process, and the substrate surface preparation. These factors can influence the thickness, uniformity, and quality of the deposited layer. The film deposition can be performed using the electrochemical cell of two or three electrodes, as illustrated in Figure 9.

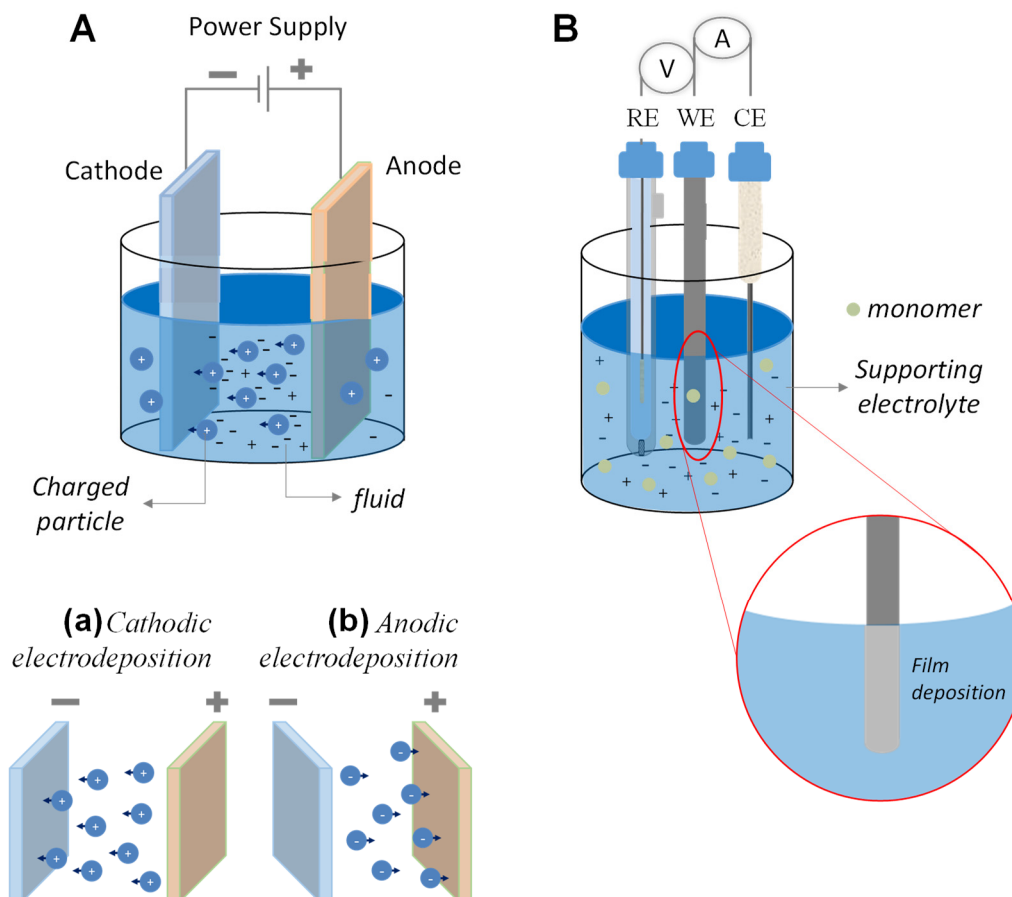


Figure 9. Illustration of an electrochemical cell for film deposition using (A) two or (B) three electrodes. (A) represents the deposition by electrophoresis technique and in (B) by the potentiodynamic or potentiostatic modes.

Electrophoresis performs ED by applying electrolysis between an anode and cathode, named electrophoretic deposition (EPD). The EPD involves the application of an electric field to drive the movement of charged particles toward the substrate, resulting in their deposition onto the substrate [209]. The deposited film by EPD is usually from metallic, ceramic, polymer, or composite materials [209]. The material suspension should contain charged particles that migrate under the influence of an electric field, i.e., the positive particles depositing through migration toward the cathode substrate (negatively charged) (Figure 9A(a)), and the negatively charged particles towards the anode substrate (positively charged) (Figure 9A(b)).

The supramolecular arrangement can be controlled by adjusting the deposition parameters, including the electric field strength, deposition time, particle concentration, and suspension composition [209]. Cai et al. [210] described the formation of polyaniline/cobalt porphyrin (PANI/CoTPP) by one-step self-assembled ED method (2.0 V, 100 s, 2 cm of electrode distance) with the deposition occurring on the anode (ITO- polyethylene terephthalate (PET) flexible working electrode). The sensing performance for ammonia detection through the PANI/CoTPP-based electrode was modulated by CoTPP monomer concentration. The increase in CoTPP concentration leads to the formation of large aggregates and high roughness, thus providing many ammonia gas adsorption sites and enhancing

the charge transfer rate. The film formed using 0.7 mmol/L CoTPP demonstrated higher sensitivity with a LOD of 0.83 ppm [210].

ED can also be performed in a voltammetric cell composed of a reference electrode, a counter-electrode, and a working electrode, where the deposition of the material occurs (Figure 9B). In this setup, the potential is applied between the reference and working electrode, and it can be performed in both potentiodynamic and potentiostatic modes. In the potentiodynamic ED, the electrode potential is varied during the deposition steps to achieve specific coating properties providing information about the ED mechanism cycle-by-cycle [211]. In potentiodynamic mode, the supramolecular arrangement, including the morphology and thickness of the film, can be controlled by the deposition rate (scan rate) [212], the number of potential cycles, and the potential range. On the other hand, the potentiostatic ED maintains a constant electrode potential for a uniform and controlled deposition, and parameters such as applied potential and time can be controlled [10].

In general, ED films on a conductor substrate have their supramolecular arrangements evaluated, attempting to understand their morphology (microscopy images) and the effect on their electrical properties (voltammetric and impedance measurements). Therefore, the optimization as a sensor is performed using techniques such as EIS and cyclic voltammetry in an inert supporting electrolyte or with a redox probe such as $[\text{Fe}(\text{CN})_6]^{3-}/[\text{Fe}(\text{CN})_6]^{4-}$. An extensive list of materials is used for both potentiodynamic and potentiostatic deposition modes. Below, a summary of recent works is organized in a group of materials, discussing mainly the effect of the supramolecular arrangement and applications as sensors.

3.3.1. Polymers and Organic Films

Conducting polymers have emerged as promising high-performance materials due to their tuneable sensitivity adjusted by formation techniques [213,214]. The conducting polymers such as thiophene [215–217], aniline [218,219], and pyrrole [217,220] can be obtained by ED, especially by potentiodynamic mode due to the possibility of understanding the mechanism of electrochemical polymerization [221]. The supramolecular arrangement and the properties of conducting polymers can be tuned by changes in the electrolyte solution, monomers, pH, doping, and electrochemical parameters such as potential range and ED time [217,221,222]. Phenazine, phenoxazine, and phenothiazine derivatives [223–225] are other examples of species with the possibility to form electrodeposited polymers, such as methylene green [226,227], methylene blue [228–230], neutral red [231,232], Nile blue [233], and others [223,234]. In general, all electrodeposited materials presented some enhancement or suppression of electrical properties due to changes in the ED stage. Olean-Oliveira et al. [234] described the role of the anion size used in the electrochemical polymerization of poly(thionine) on its electrical properties. The potential for radical cation formation depends on the anion size, with the large ones demanding lower potential application. The anion size also influences the polymer redox behaviour by limiting the movement of anions through the polymer matrix [234]. The effect of anion or polyelectrolytes on the electrochemical polymerization of conducting polymers and their efficiency in detecting ammonia was reported by Gribkova et al. [235] and Patois et al. [236].

Eventually, a previous electrode modification can be performed before the ED. Silva, Queiroz, and Brett [226] electrodeposited methylene green on the GCE surface previously modified with $\text{Fe}_2\text{O}_3\text{NP}$ (iron oxide nanoparticles)-chitosan. The poly(methylene green) (PMG) was electrodeposited in an ethaline deep eutectic solvent and an aqueous solution for comparison. The ED was performed by applying 15 potential cycles between -0.6 and $+0.8$ V at a scan rate of 50 mV s^{-1} . Different $\text{Fe}_2\text{O}_3\text{NP}$ loadings (0.2%, 0.5%, and 1.0% *w/v*) were evaluated, which influenced growth, surface morphology, and charge transfer (Figure 10). The $\text{Fe}_2\text{O}_3\text{NP}_{0.2}/\text{GCE}$ presented the best polymer film growth, and when tested to detect the antibiotic 4,4-diaminodiphenylsulfone, a LOD of $0.33 \mu\text{mol/L}$ was achieved.

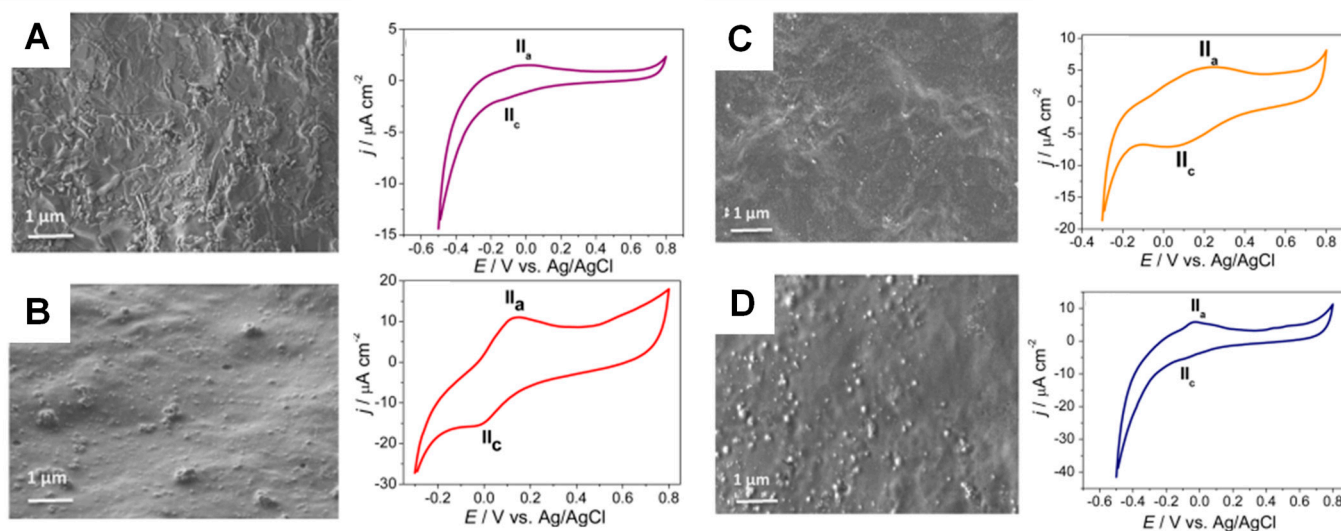


Figure 10. SEM images and corresponding cyclic voltammograms (Britton-Robinson buffer pH 3, scan rate 50 mV s^{-1}) of (A) $\text{PMG}_{\text{aqueous}}\text{-Fe}_2\text{O}_3\text{NP}_{0.2}$, (B) $\text{PMG}_{\text{ethaline}}\text{-Fe}_2\text{O}_3\text{NP}_{0.2}$, (C) $\text{PMG}_{\text{ethaline}}\text{-Fe}_2\text{O}_3\text{NP}_{0.5}$ and (D) $\text{PMG}_{\text{ethaline}}\text{-Fe}_2\text{O}_3\text{NP}_{1.0}$. Reprinted from [226]. Copyright 2020, with permission from Elsevier.

The ED of biomimetic polymers has attracted attention due to their biocompatibility and strong adhesive properties [237,238]. Besides, recent studies have revealed the development of a supramolecular arrangement that exhibits characteristics reminiscent of a 2D-ordering material [239,240]. Almeida et al. [241] described the effect of co-ED of polydopamine and laccase through one-step potentiostat deposition for application as the phenolic sensor. Incorporating laccase does not significantly affect a polydopamine film's redox behaviour, optical properties, and morphology. However, it alters the film's charge transfer properties, thickness, and hydrophilicity. The polydopamine-laccase film presented a LOD of 0.14, 0.09, and $0.29 \mu\text{mol/L}$ for caffeic acid, rosmarinic acid, and gallic acid, respectively [241].

3.3.2. Cyclodextrins

Cyclodextrins (CD) are cyclic oligosaccharides formed by glucose molecules, joined by glycosidic linkages, which allowed the formation of a truncated cone structure, which can be classified according to chain sizes as alfa, beta, and gamma ($\alpha\text{-CD}$, $\beta\text{-CD}$, $\gamma\text{-CD}$) [242]. The cone-like structure has been a recent property explored in the formation of sensors by CD ED. Pereira et al. [243] discussed the electrochemical polymerization of $\beta\text{-CD}$ in different experimental conditions. Diverse experimental parameters were tested until establishing the optimized conditions: potential range of -1.3 to 0.9 V at 100 mV/s , electrolyte at pH 5 with $\beta\text{-CD}$ concentration of 6 mmol/L under agitation and in the absence of dissolved oxygen.

Due to the hydrophobic inner cavity, the $\beta\text{-CD}$ can host biomolecules (bio-recognition probes). Chang et al. [244] described the electrochemical polymerization using the potential range of -1.0 to $+1.0 \text{ V}$ at 20 mV/s and 10 potential cycles. Following, the $\beta\text{-CD}$ allowed the immobilization of the aptamer fragment (amino-modified aptamer fragment 1, AF1) through covalent bound with carboxylic acid functionalized adamantane using EDC/NHS chemistry. The modified electrode demonstrated an enhanced charge transfer after inserting AuNPs on the electrode surface. The voltammetric detection of $17\beta\text{-estradiol}$ achieved a LOD of $6.3 \times 10^{-14} \text{ mol/L}$ [244]. The $\beta\text{-CD}$ has also been incorporated within conducting polymers and carbon derivatives, playing an important role in detecting many target molecules, such as biomolecules, drugs, pesticides and others [245–251].

3.3.3. Phthalocyanines (Pc)

The porphyrins and Pc have demonstrated interesting results for sensing applications [252] due to their structural properties, such as π -conjugated bonds, chemical and thermal stability, and self-organization [253]. Due to their high supramolecular stabilization and adsorption on the conducting surfaces, these molecules have been used to create ED films for sensing and electrical devices [254–257]. The porphyrins also draw attention due to the possibility of their ED through the metal-free porphyrins [212,258]. Kusmin et al. [258] demonstrated the effect of the substituents in porphyrins and investigated how the potentiostatic or potentiodynamic modes influence the film deposition, leading to changes in the supramolecular arrangement, including surface morphology and molecular structure [258]. For instance, the films of meta-substituted hydroxyphenylporphyrin exhibited a blocking effect on the electrochemical reaction, while the para-substituted hydroxyphenylporphyrin allowed the fabrication of polymeric films with a thickness of up to 300 nm and high specific conductivity [258]. Furthermore, the morphology is influenced by both chemical substitution and ED mode. A homogeneous distribution was observed for porphyrin films formed by potentiodynamic mode, while large aggregates were observed for the potentiostatic mode, as shown in the AFM images (Figure 11).

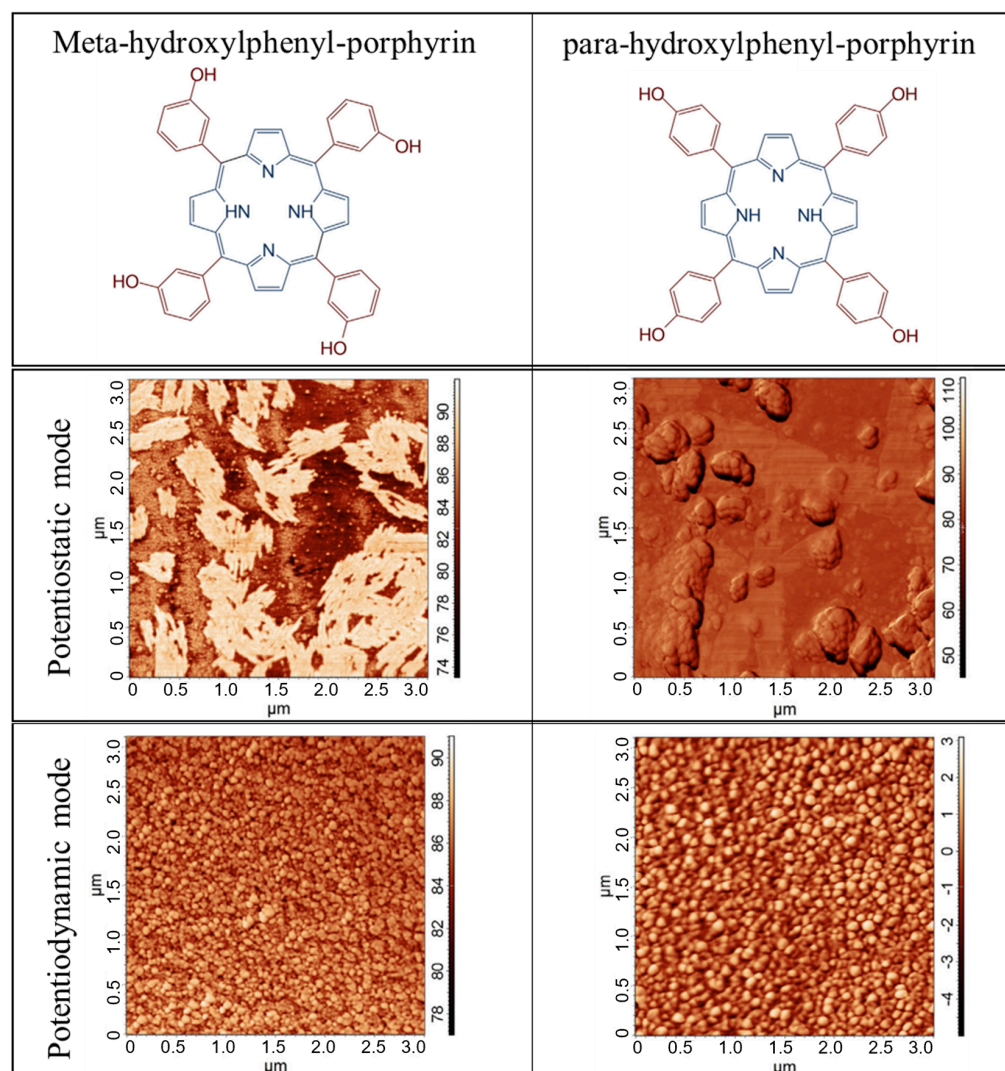


Figure 11. Structure and surface morphology by AFM images of meta-hydroxyphenylporphyrin and para-hydroxyphenylporphyrin formed by potentiostatic and potentiodynamic potential modes. Reprinted with permission [258]. Copyright 2020, with permission from Elsevier.

Metal Pc is a versatile molecule for film deposition through potential application [259,260]. Iron phthalocyanine (FePc) can be electrodeposited using dynamic and static modes [260]. Besides, the supramolecular arrangement of FePc films can be controlled by the deposition technique, as well as variations in the ED parameters [10,261]. When electrodeposited in the potentiostatic mode, the film exhibited variations in its optical and electrical properties with the ED time. Specifically, a flat-on molecular organization was observed after 1800 s of ED at -1.5 V [10]. The FePc films applied to catecholamine detection presented a LOD of 0.28 and 0.56 $\mu\text{mol/L}$ to dopamine and L-dopa, respectively [261]. The properties of Pc ED films can also be modulated through the incorporation of rGO, as reported by Charles and Mashazi [262]. In this case, the ED of rGO and cobalt tetraamino phthalocyanine (CoTAPc) demonstrated a synergic effect on the electron transfer, which allowed the simultaneous detection of dopamine and paracetamol with a low LOD, 0.095 and 0.104 $\mu\text{mol/L}$, respectively [262]. The synergic effect between Pc and rGO was also observed for other deposition methods [263].

3.3.4. Carbon Derivatives

Carbon derivatives are widely applied in electrode modification for sensor development [264–267]. In general, the carbon derivatives such as single-walled carbon nanotubes (SWCNTs), MWCNTs, and GO are deposited on the conducting electrode surface by drop casting technique followed by the ED of other functional materials forming hybrid films [231,232,268,269]. For example, Gally, Eguilaz, and Rivas [269] developed a glucose sensor based on the deposition of the enzyme onto a previously modified GCE. This modification encompassed the casting of avidin(*Av*)-MWCNT suspension onto the electrode followed by the ED of ruthenium nanoparticles (RuNPs) (constant potential of -0.6 V) to produce GCE/*Av*-MWCNT/RuNPs. The synergy between MWCNT and RuNPs allowed an increased catalytic property towards peroxidase reduction, with a LOD of 65 nmol/L. Thus, biotinylated-Glucose Oxidase (biot-GOx) was self-assembled, producing the GCE/MWCNT-*Av*-RuNP/biot-GOx, with a LOD to glucose equal to 3.3 $\mu\text{mol/L}$. In addition, the authors emphasize the importance of the supramolecular arrangement, with the GCE/*Av*-MWCNTs/RuNPs composition better than the GCE/RuNPs/*Av*-MWCNTs motivated by the lower accessibility of RuNPs through the *Av*-MWCNTs layer, as well as to a less efficient deposition of *Av*-MWCNTs onto a previous RuNPs modified-electrode. As pointed out by this example, when constructing a biosensor, the ED stage may be conducted before the immobilization of biomolecules, such as enzymes, DNA, proteins, and antibodies [270].

Alternatively, hybrid structures can also be generated by one-step co-ED of carbon-based materials mixed with other materials [271,272], as demonstrated by Sen and Sarkar [271]. They co-electrodeposited AuNPs, PEDOT (poly(3,4-ethylenedioxythiophene)), and functionalized MWCNTs on the surface of GCE. Initially, a stable colloid suspension of Au-PEDOT-MWCNT was prepared, followed by applying a potential range of -0.9 to $+1.8$ V through nine potential cycles with a scan rate of 50 mV/s [271]. The ED enhanced the effective surface area, sensitivity, and selectivity of the sensor for simultaneous detection of uric acid, xanthine, and hypoxanthine, demonstrating a LOD in the nanomolar range (199.3, 24.1; 90.5 nmol/L, respectively) [271].

Graphene derivatives have also attracted considerable attention for electrode modifications [248,273–276]. Kanagavalli et al. [277] electrochemically reduced GO (ErGO) on GCE, performing 20 cycles between 0 to -1.5 V at 50 mV/s (Figure 12A). The ErGO/GCE was investigated by in-situ Raman and X-ray photoelectron spectroscopic (XPS), revealing the ErGO surface with an abundant graphitic carbon network with residual oxygenated functional groups, which favours the electropolymerization of melamine (3 mmol/L melamine monomer in 0.5 mol/L H_2SO_4 and 5 mmol/L KCl with 20 potential cycles between 0 to 1.6 V at 100 mV/s) (Figure 12B) [277]. The ED of polymelamine (PM) was confirmed by the increase in the Raman band between 1720 and 1760 cm^{-1} , corresponding to the formation of an amine-substituted C=O functional group (Figure 12C). The SEM images also indicated

increased surface roughness after PM deposition (Figure 12A,B). The amperometric measurements indicated a catalytic effect of PM/ErGO/GCE for acyclovir when compared to ErGO/GCE, GO/GCE, PM/GCE, and bare GCE (Figure 12D). Modifying the GCE surface with ErGO before PM ED allowed modulating the sensing properties to detect acyclovir, resulting in a very low LOD (137.4 pmol/L) [277].

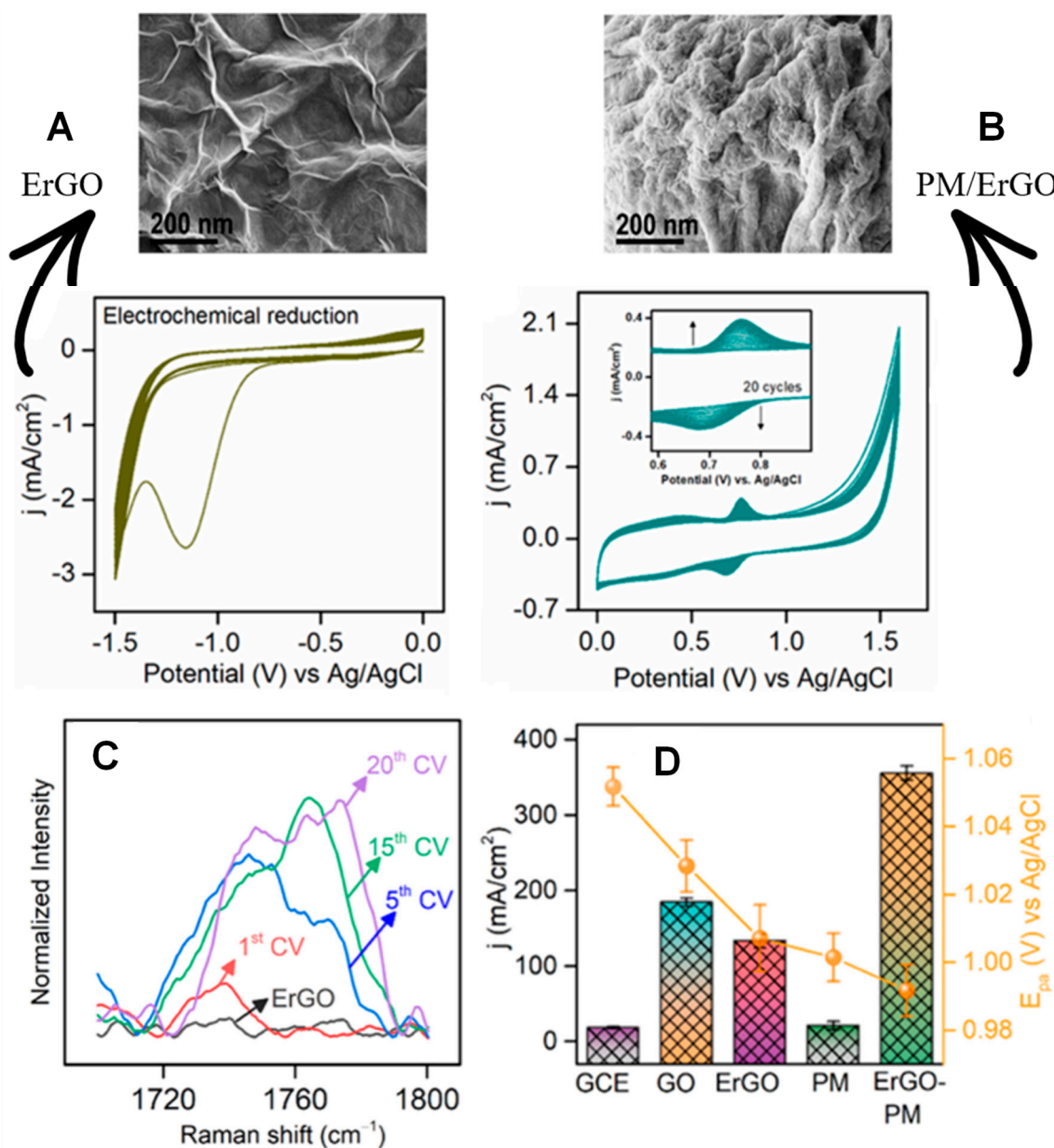


Figure 12. Cyclic voltammogram recorded during the (A) electrochemical reduction of GO/GCE to ErGO/GCE (0.1 mol/L PBS at pH 7.0 and 50 mV/s), and (B) electrochemical polymerization of melamine on ErGO/GCE (20 potential cycles at 100 mV/s in 0.5 mol/L H_2SO_4 containing 3 mmol/L melamine and 5 mmol/L KCl), and respective SEM images. (C) Emerging Raman band between 1720 and 1760 cm^{-1} observed during the PM formation. (D) Current density and anodic peak potential for acyclovir oxidation using the different modified electrodes. Adapted with permission from [277]. Copyright 2023 American Chemical Society.

3.3.5. Nanoparticles

Metal oxide [278–283] and metal [215,284,285] nanoparticles have also been electrodeposited for the development of sensors [286]. The metal oxide nanoparticle films can be

prepared by the potentiodynamic or potentiostatic modes or using both combined [283]. The potentiodynamic mode is assigned to the nucleation step, while the potentiostatic mode is to the particle growth, as reported by Dumore and Mukhopadhyay [283] studying the ED of SiO₂NPs. The authors explored the effect of the ED time (100 to 800 s) on the electrocatalysis towards H₂O₂ reduction [283]. The optimized parameters (potential of -0.85 V for 600 s) provided a high electrocatalytic effect with a sensitivity of $67.6 \mu\text{A}/\text{mmol cm}^2$ [283]. The electrocatalytic effect was improved by additional ED of platinum nanoparticles (PtNPs) and selenium nanoparticles (SeNPs). The sequence and the duration of the ED of each layer influence the morphology and electrocatalytic effect on H₂O₂ detection. The best performance was obtained for PtNPs-SeNPs-SnO₂NPs@FTO with flower, spherical and irregular shapes, while the SnO₂NPs@FTO presented only spherical and irregular shapes [283]. The PtNPs-SeNPs-SnO₂NPs@FTO demonstrated a sensitivity of $104.8 \mu\text{A}/\text{mmol cm}^2$ and a LOD of 0.01 mmol/L for H₂O₂ [283].

The AuNPs are also easily electrodeposited at the conductor surface for both potentiodynamic [268,287,288] and potentiostatic modes [257,289–292]. Compared to usual chemical routes, ED is advantageous mainly for being environmentally friendly, avoiding the use of reducing agents and stabilizers, which can hamper the conducting and catalytic properties. The supramolecular arrangement can be modulated by variations in the potential, electrolysis time, and ED precursor solution, changing principally the size and shape of nanostructures [286]. Due to the great number of works based on the electrodeposited AuNP films towards sensing applications, Table 1 summarizes the ED conditions, morphology, and sensing applications. The ED of AuNPs begins with the adsorption and reduction of AuCl₄[−] ions. Nucleation and growth occur simultaneously at potentials more negative than -0.8 V [286,293].

Table 1. List of electrodeposited AuNP film-based sensors: electrodes, precursor solution, ED conditions, morphology, and sensing applications.

Substrate	Solution	ED Conditions	Size/Shape	Application/LOD	Ref.
Carbon paper	H ₂ AuCl ₄ ·3H ₂ O (0.1%) solution	-0.2 V for 120 s	400 nm/spherical	Voltammetric sensor for glyphosate/ $0.03 \mu\text{mol/L}$	[257]
MoS ₂ /SPE	1:1 (v:v) of H ₂ AuCl ₄ and H ₂ PtCl ₆ in 0.2 mol/L Na ₂ SO ₄	-0.5 V for 100 s ^a	110–130 nm/spherical	Voltammetric sensor for lactic acid/ $0.33 \mu\text{mol/L}$	[284]
AC/GCE	5.0 mmol/L H ₂ AuCl ₄ ·3H ₂ O in 0.05 mol/L H ₂ SO ₄	-1.0 V for 30 s	125 nm/non-uniform	Voltammetric sensor for ciprofloxacin/ 0.20 nmol/L	[289]
FPC	0.5 mmol/L H ₂ AuCl ₄ ·3H ₂ O in 0.5 mol/L H ₂ SO ₄	-0.9 to 200 s	typical mellow and full shape	Voltammetric sensor for imidacloprid/ 61 nmol/L	[292]
N-rGO/GCE	0.1 mmol/L H ₂ AuCl ₄ in 0.1 mol/L PBS (pH 6.0)	-0.2 to -1.3 V, 20 cycles, 50 mV/s	spherical	Simultaneous voltammetric detection of uric acid/ 0.9 nmol/L and xanthine/ 90 pmol/L	[294]
PMD/PGEs	0.5 mmol/L H ₂ AuCl ₄ ·3H ₂ O in 0.1 mol/L KCl	-1.0 to 0.2 V, 10 cycles, 100 mV/s	50 nm/spherical	Voltammetric sensor for darifenacin/ $0.94 \mu\text{mol/L}$	[287]
NF/CD	6.0 mmol/L H ₂ AuCl ₄ in 0.1 mol/L KNO ₃	-0.8 to 0.4 V, 20 cycles, 50 mV/s	clusters	Voltammetric sensor for dopamine/ 0.6 nmol/L	[288]
GCE	0.25 mmol/L H ₂ AuCl ₄ +5 mmol/L luminol in 0.5 mol/L H ₂ SO ₄	0 to 1.0 V, 20 cycles, 100 mV/s ^b	5 nm/spherical	Immuno sensor for prostate antigen/ 0.45 fg/mL	[290]

Table 1. Cont.

Substrate	Solution	ED Conditions	Size/Shape	Application/LOD	Ref.
CNPs/GCE	5.0 mmol/L HAuCl ₄	−0.3 to 1.2 V, 10 cycles, 50 V/s	spherical	Voltammetric sensor for arsenic/0.092 ppb	[268]
SPCE *	-	0.9 to 0 V, 5 cycles, 100 mV/s	spherical	Voltammetric sensor for myo-inositol/1 nmol/L	[295]
PANI/GCE	HAuCl ₄ (1%)	−0.2 V for 30 s	clusters	electrochemiluminescence immunosensor for 3-nitrotyrosine/2.57 pmol/L	[296]
SPCE/ZnONR/ PMBDES	4.0 mmol/L HAuCl ₄ in 0.05 mol/L PBS (pH 7.0)	−1.3 to 0.2 V, 10 cycles, 50 mV/s	spherical	Voltammetric sensor for serotonin (5-HT)/1.91 nmol/L	[297]
ITO	0.05 mol/L HAuCl ₄	−0.2 to 1.3 V, 10 cycles, 50 mV/s	5.8 nm/spherical	Electrochemical biosensor for GM2A/5.8 fg/mL	[298]

^a—co-electrodeposition with platinum nanoparticles (bimetallic AuPt nanoparticles); ^b—co-electrodeposition with luminol. GCE: glassy carbon electrode; MoS₂: molybdenum disulphide; SPCE: screen-printed carbon electrode; FPC: flexible printed circuit; N-RGO: nitrogen-doped reduced graphene oxide; PMD: poly-methylidopa; PGEs: pencil graphite electrode; NF: Nafion; CD: cyclodextrin; CNPs: carbon nanoparticles; PANI: polyaniline; ZnONR: zinc oxide nanorod; PMBDES: polymethylene blue (deep eutectic solvent); ITO: thin-oxide electrode; GM2A: GM2 activator protein, * SPCE/Au as support for electrodeposition of 3-aminophenylboronic acid (3-APBA) with myo-inositol (MI) for molecularly imprinted polymer based MI sensor.

Regarding the co-ED of metal NPs with other materials, it can influence the final shape [299] and size distribution [271,284]. Zhe et al. [299] described the co-ED of rGO, β-CD, and AgNPs by cycling from 0 V to −1.5 V 30 times with a scan rate of 50 mV/s. The composition allowed the formation of dendritic nanostructures, providing a large active surface confirmed by FE-SEM images. Besides, the XRD reveals peaks at 38° (111), 44° (200), 64° (220), and 77° (311), indicating a standard face-centred cubic structure AgNPs [299]. The film was applied for electrocatalytic oxidation of nitrite at low over-potential, presenting a LOD of 0.24 μmol/L [299]. The co-ED of metal nanoparticles with other organic materials has been used as a simple approach to tune the electrochemical performance and enhance the sensitivity and selectivity of sensors [271,284,299].

Aiming biosensor development, the formation of electrodeposited AuNP films also offers an easy functionality for anchoring biomolecules, such as enzymes, nucleic acids, and antibodies [268,290,296,298,300]. Aydin, Aydin, and Sezgintürk [298] described the construction of an immunosensor for GM2 activator protein (GM2A, a cancer marker) following six steps (Figure 13). At first, AuNP ED was performed by potentiodynamic mode, and in step 2, the electropolymerization of amine-functionalized thiophene (ThiAmn) to produce poly-ThiAmn. Next, a layer of glutaraldehyde was added (step 3) to allow the antibody (anti-GM2A) immobilization (step 4); the unspecific sites were blocked by BSA (step 5); finally, perform the incubation with the antigen (GM2A). The thickness of the ThiAmn polymer layer influenced the immunosensor performance: varying the number of cycles (2, 5, and 10 potential cycles) between −0.5 and 2.5 V at 100 mV/s, the highest signal was achieved with 5 cycles [298]. The ITO/AuNPs/P(ThiAmn)/anti-GM2A/BSA electrode provided a very low LOD (5.8 fg/mL) for GM2A using the EIS technique (Nyquist plots and the relationship between the charge transfer resistance— R_{ct} versus GM2A concentrations were presented in Figure 13B and Figure 13C, respectively) [298].

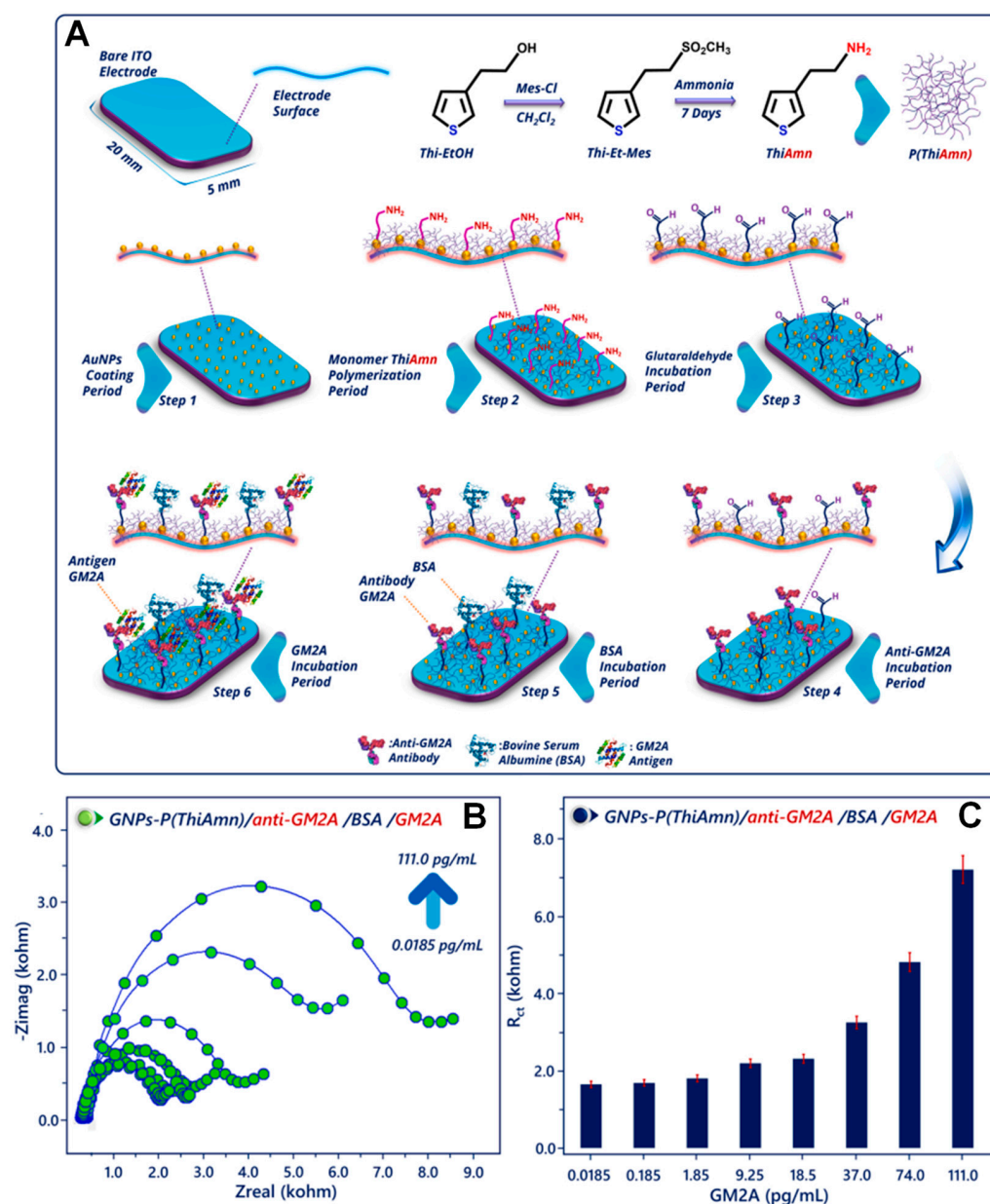


Figure 13. (A) Schematic illustrating the ThiAmn monomer obtention and the electrochemical assay for analysis of GM2A. The modification consists of six steps: GNPs deposition (Step 1), ThiAmn electropolymerization (Step 2), glutaraldehyde treatment (Step 3), anti-GM2A immobilization (Step 4), BSA blockage of free ends (Step 5), and GM2A capture by the biosensor (Step 6). (B) Nyquist diagram and (C) R_{ct} of the ITO/AuNPs/P(ThiAmn)/anti-GM2A/BSA electrode after interaction with different GM2A concentrations. The frequency range was 0.05–50 kHz. Thi-Et: 3-thiopheneethanol, Thi-Et-Mes: 3-(2-(methylsulfonyl)ethyl)thiophene. Reprinted from [298]. Copyright 2023, with permission from Elsevier.

3.4. Spray Pyrolysis

Spray coating is a method in which a liquid solution containing the desired materials is atomized and sprayed onto the substrate using a spray system. The sprayed material forms a thin layer on the substrate as it is deposited. This technique is widely used for large-scale coating applications, such as painting, protective and anticorrosive coatings [301–304]. There are two specific techniques related to spray coating: spray cold and spray pyrolysis [305]. Spray cold (SC) refers to the application of a coating or material at ambient or lower temperatures. SC coatings can be solvent-based or water-based, depending on the specific requirements

and composition of the coating material [306]. Spray pyrolysis (SP) is a technique used to deposit thin films by thermally decomposing precursor materials in a spray form. The process involves spraying a solution or suspension of precursors onto a heated substrate. As the droplets contact the substrate, the precursor undergoes pyrolysis, resulting in the deposition of a solid film on the surface. SP is often used to produce thin films in areas such as thin-film solar cells, gas sensors, and electronic devices [307]. SC and SP offer advantages in terms of ease of application, uniformity of coating, and adaptability to various substrates. However, SP is the most reported method in the literature.

According to Workie et al. [305], during the 1950s and 1960s, SP was primarily utilized for depositing metallic and semiconductor films. The main objective was to comprehend the fundamental principles of this method and create uncomplicated precursor solutions and process conditions capable of producing high-quality films. SP gained popularity in the 1970s and 1980s for depositing oxide films, including titanium, zinc, and zinc-tin oxides. During this period, the research began exploring surfactants, micelles, and polymers to regulate the morphology of the deposited films. In the 1990s and 2000s, there was a notable increase in SP applications to deposit a diverse range of materials, including composites, alloys, and multilayer structures. This progress was followed by developing new precursor solutions, such as organometallic precursors and precursors containing various metallic species. These advances allowed the growth of intricate structures with precise control over composition and morphology. Due to technological advances, SP has experienced significant improvements, facilitating the deposition of a wide range of materials and utilizing more advanced precursor solutions. These improvements have enhanced the ability to control the morphology, composition, and structural properties of films produced through this technique.

SP deposition involves spraying tiny droplets of a precursor solution, in the form of aerosols, onto a heated substrate through a nozzle [308]. The quality of the resulting film is influenced by factors such as solvent evaporation, droplet state, and chemical reactions, which are, in turn, influenced by the size and momentum of the droplets [309–311]. A schematic illustration of the SP deposition process is presented in Figure 14.

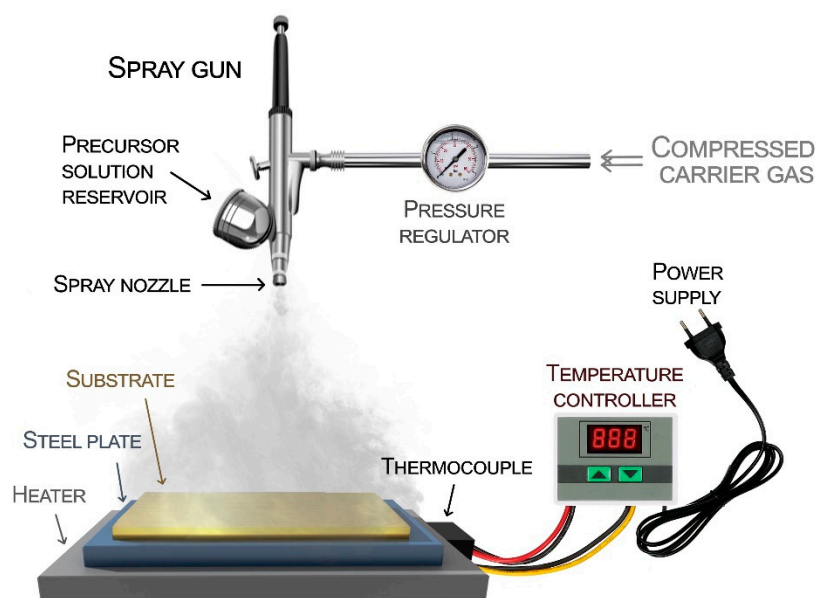


Figure 14. Simple schematic illustration of spray pyrolysis technique.

The SP technique comprises several components, including a spray gun, temperature controller, liquid flux meter, pressure regulator, heater, thermocouple, and a metallic airtight chamber. The spray gun can be attached to a rotor, facilitating its movement over the substrate and allowing dynamic spraying. The spray nozzle breaks down the precursor

solution into tiny droplets and this allows the solution to be sprayed effectively. The spray nozzle rotor, driven by an electric gear motor, is controlled by a speed controller to maintain a consistent spray rate. The heating element is a hot plate made of iron and equipped with an electric heater. This setup can achieve a maximum temperature of up to 600 °C [307]. A thermocouple is in contact with the hot iron plate to measure the temperature of the substrate. The temperature controller regulates the temperature of the iron plate to maintain desired conditions. The gas valve controls the carrier gas pressure, ensuring proper spraying conditions. Generally, the spray system is kept inside a metallic airtight chamber, which includes an exhaust to remove the gases emitted during the spray deposition process. Next, we discuss the effect of SP deposition parameters on the structure and organization of thin films.

3.4.1. Effect of Deposition Parameters

The SP method is highly effective in producing thin films with controlled morphology and uniform particle sizes. A notable advantage of this technique is its versatility in creating various nanostructures, which can be achieved by adjusting parameters such as precursor type, substrate temperature, flow rate, carrier gas, solvent type, and other deposition variables [312]. The types of nanostructures that can be deposited using the SP technique include nanorods [313], nanosheets [314], nanowires [315], nanospheres [316], and nanoparticles [317], among others. Abdulrahman et al. [318] employed the SP technique to produce zinc oxide (ZnO) nanoflowers on silicon substrates for efficient ultraviolet radiation detection. These flower-like clusters (Figure 15) are formed through a preferential growth direction and are densely packed across the substrate surface. The ZnO nanoflowers exhibited a morphology composed of tightly packed nanoneedles. The authors attributed the remarkable photoresponse of the ZnO nanoflowers device to their high surface-to-volume ratio and enhanced crystal performance. These results highlighted the efficacy of the low-cost SP technique in creating highly photoconductive ZnO nanodevices for various applications in photoelectronics.

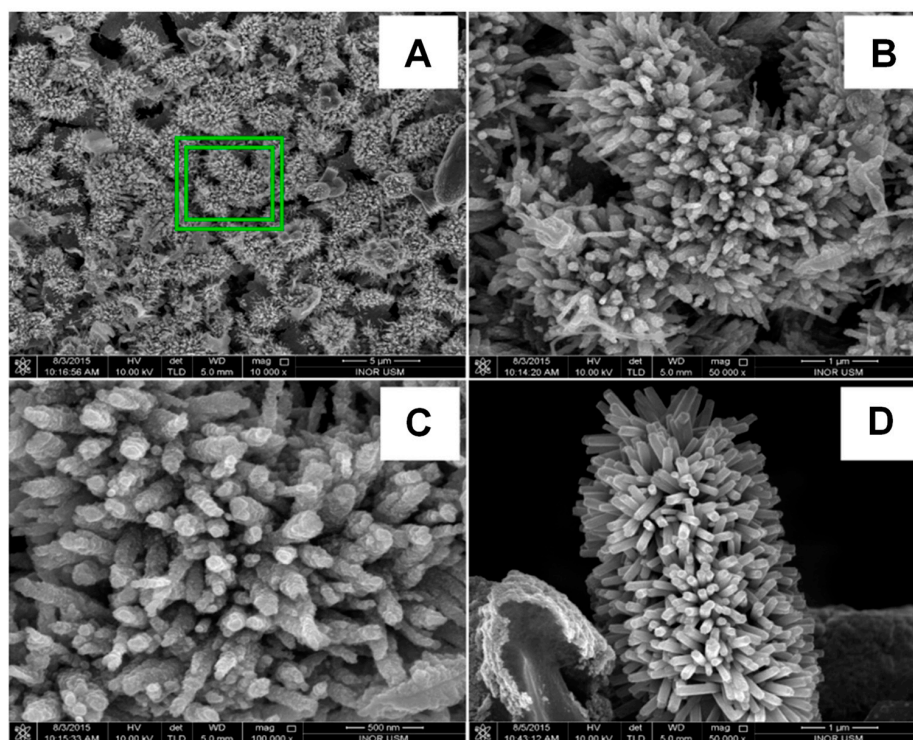


Figure 15. SEM images of ZnO nanoflowers at different magnifications: (A) 5 μm , (B) 1 μm , (C) 500 nm, and (D) cross-section of ZnO nanoflowers grown on a porous silicon substrate with a magnification of 1 μm . Reprinted from [318]. Copyright 2022, with permission from Elsevier.

The main parameters of the SP technique and their impacts on the characteristics of thin films are mentioned below:

1. **Solution flow rate:** the flow rate of the spray solution affects the thickness and uniformity of the deposited film. Higher flow rates lead to thicker films resulting in less uniformity and more defects, on the other hand lower flows lead to thinner films and may result in no percolation. Therefore, it is important to optimize the flow rate to achieve the desired film thickness and uniformity. Yusuf et al. [319] investigated the influence of the solution flow rate on the structural, morphological, and electrical properties of molybdenum oxide films. The arriving spray on the silicon substrate was controlled by varying the solution flow rate (ranging from 3.0 to 1.5 mL/min) at the substrate temperature of 300 ± 5 °C. XRD analysis allowed verify the changes in the crystallite size as the flow rate decreased. A morphological study using FE-SEM and AFM demonstrated the reducing grain size with decreasing flow rate, which promotes the homogeneity and smoothness of the film. In a study conducted by Zargou et al. [320], thin films of ZnO were deposited on glass substrates using a spray solution volume of 60 mL at 300 °C and employing different spray rates of 5, 10, 15, and 20 mL/h. They observed that the solution flow rate had a significant impact on the physical and structural properties of the thin films. The ZnO thin film deposited at a solution flow rate of 15 mL/h exhibited remarkable characteristics displaying high transparency, with a transmission rate of 99.1%. Additionally, this film demonstrated the highest electrical conductivity in dark conditions. Moreover, it exhibited the lowest carrier concentration, activation energy, and resistivity among the tested deposition conditions. Overall, the findings emphasized the notable influence of the solution flow rate on the properties of the ZnO thin films, particularly highlighting the favourable attributes achieved at a flow rate of 15 mL/h.
2. **Solution composition:** the composition of the spray solution, which includes the precursor materials and solvents [321], dramatically influences the chemical composition and stoichiometry of the resulting film. Modifying the concentration and ratio of precursors can alter the film's elemental composition, doping levels, and crystalline structure [322].
3. **Pyrolysis temperature:** the substrate temperature during the deposition in SP impacts the film's crystallinity, grain size, and morphology [323]. Higher substrate temperatures promote crystallization and grain growth, producing films with improved crystallinity and larger grain sizes. Furthermore, uncontrolled high temperatures can lead to film degradation or damage to the substrate. Ebin et al. [324] reported the production of ZnO nanoparticles and porous particles using the ultrasonic SP method through zinc nitrate precursor at different temperatures under an air atmosphere. The ZnO particles were obtained in a hexagonal crystal structure, and the shape of the crystallites changed from spherical to hexagonal as the reaction temperature increased from 400 to 1000 °C. At the lowest reaction temperature, ZnO nanoparticles were obtained, while at higher temperatures, ZnO porous particles were formed through the aggregation of ZnO nanoparticles due to effective sintering. The results indicate that the reaction temperature can be readily adjusted to manipulate the size and morphology of ZnO nanostructures, highlighting the suitability of the SP method for large-scale production due to its controllability. Al Ghamdi et al. [325] investigated the influence of substrate temperature and solution concentration on the properties of copper oxide (CuO) thin films. They deposited a series of CuO thin films on glass substrates, varying the temperature between 400 and 650 °C and using two different concentrations of copper salt. The structure and morphology of the films were examined using XRD and SEM, while UV-visible spectroscopy was employed to analyse their optical properties. A significant influence of substrate temperature on the growth mechanisms and physical characteristics of the CuO films was verified: the films primarily exhibited a single phase of CuO with an observed reduction in crystallite size as the substrate temperature increased. Hameed et al. [326] fabricated

nickel oxide (NiO) thin films on glass substrates using the SP technique at different temperatures (300, 400, and 500 °C). Analysis of the XRD data confirmed the presence of a cubic structure in the films, indicating their polycrystalline nature. Notably, it was observed that at a temperature of 500 °C, the lattice constant of the thin films closely approached the ideal lattice parameter of 4.176 Å for a cubic structure. Therefore, it can be concluded that the thin films exhibited a desirable lattice constant at 500 °C.

4. Distance between the nozzle and substrate: the distance between the spray nozzle and the substrate affects the film's morphology and surface roughness. Generally, its decrease results in a denser and smoother film due to the increased heat and mass transfer efficiency [327]. Omar [328] studied the influence of the distance between the nozzle and substrate on the morphological, structural, chemical composition, and optical properties of ZnO thin films deposited using the SP technique. The morphology of the thin film was examined using Scanning Tunneling Microscopy (STM), and it was observed that reducing the nozzle-substrate distance led to an increased root mean square (rms) roughness. Specifically, the rms values were measured as 17.470 nm and 10.062 nm at 20 cm and 30 cm distances, respectively. The surface morphology strongly influenced the optical properties, including transmittance and the optical band gap, parameters of great importance to photovoltaic applications.
5. Spray pressure: the spray pressure influences the droplet size, spray pattern, and film morphology. Higher pressure causes a lower solvent evaporation rate compared to lower pressure, and this allows the solute crystal to grow in a relatively longer time and thus larger nanoparticles are formed [327,329]. In addition, excessively high pressure can cause droplet fragmentation or spray pattern distortion.
6. Deposition time: the deposition time must be controlled according to the desired consistency and film quality requirements in order to avoid defects or degradation. Hathot et al. [330] conducted a study to assess the influence of different deposition times (4, 8, and 12 min) on the crystallinity, absorption, and electrical characteristics of zinc sulfide thin films (ZSTFs). XRD analysis of the ZSTFs indicated the presence of both hexagonal and cubic phases. The average crystallite size of the thin films ranged from 27.81 to 31.54 nm, while the optical band gap energy varied between 2.7 and 3 eV. The thin films exhibited low transmittance in the visible and infrared regions, with the surface roughness playing a significant role in this characteristic. As the deposition time increased, the refractive indices of the films also increased while the extinction coefficients decreased. The thin films demonstrated excellent electrical and dielectric properties, making them suitable for various applications.

By adjusting these deposition parameters in SP, it is possible to control the film's composition, structure, morphology, and properties. Optimization of these parameters is crucial to achieving the desired film characteristics for specific applications, particularly thin-film devices, e.g., thin-film transistors (TFTs) [331,332], electrolyte-gated transistors (EGTs) [333–335], capacitors [310], diodes [336,337], solar cells [338,339], gas sensors [340], etc. It is important to note that the specific device fabrication processes and materials may vary depending on the desired application and the research advancements in the field.

3.4.2. Sensing Applications

The SP technique offers numerous advantages for fabricating different nanostructured films for sensor applications. By adapting the composition, morphology, and properties of these nanostructures, sensors can be designed to exhibit greater sensitivity, selectivity, stability, and response time. For example, gas sensors have been developed with metal oxide films using SP [341–343]. Metal oxide films, such as tin oxide (SnO) and zinc oxide (ZnO), can exhibit changes in their electrical properties when exposed to specific gases, enabling them to detect and quantify the gas concentration. Similarly, other types of sensors, such as humidity [344,345] and biosensors [346], can be developed by incorporating appropriate materials into the film composition. SP allows one to fabricate thin films that

serve as active sensing elements with the material's choice and the sensor's specific design depending on the target application and desired sensing capabilities.

Martínez-Saucedo et al. [347] investigated the impact of copper oxide film thickness in a working electrode for a non-enzymatic glucose sensor. The CuO film was deposited on a conductive nickel substrate by the SP technique, where diethanolamine (DEA) was used as the reducing agent. The use of DEA offered the advantage of employing lower deposition temperatures (290 °C), resulting in low-resistivity films suitable for building glucose-sensing electrodes. The sensitivity ($0.475 \text{ mAmm}^{-1}/\text{cm}^2$) obtained in a wide glucose range (0–8 mM) enabled the quantification of glucose levels for diabetes mellitus monitoring. This work demonstrated that a straightforward solution-based technique such as SP could be utilized to produce functional glucose sensors.

In another study, Dong et al. [348] reported the fabrication of a modified GCE with Ag-substituted ZnO nanoflowers to detect tyramine. The Ag-substituted ZnO nanoflowers were synthesized on the GCE by the SP technique, revealing nanoflowers structures with high porosity, surface area, and density. The structural analysis confirmed Ag incorporation into the ZnO nanoflowers lattice, with ZnO adopting a hexagonal wurtzite structure and silver exhibiting a face-centred-cubic phase. These results demonstrated that the SP technique is highly promising for producing ZnO nanostructures. Amperometric measurements indicated a rapid response of the Ag-substituted ZnO-modified GCE to successive additions of tyramine, resulting in a linear range of 1–900 μM and a LOD of 0.03 μM . The interference study confirmed the selective and reliable response for tyramine.

The SP technique has also shown excellent results for the fabrication of mesoporous SiO_2 towards an efficient enzyme immobilization [349]. Using MWCNTs as a template, Kumar et al. [349] synthesized SiO_2 microparticles with a mesoporous multi-compartment structure and open pores. These highly porous SiO_2 particles were synthesized through a post-treatment process of MWCNT- SiO_2 composite particles, initially synthesized via a one-pot SP process. Glutaraldehyde-functionalized porous SiO_2 particles were then employed to immobilize lipase. The enzyme immobilized on the highly porous SiO_2 particles exhibited superior characteristics compared to previously reported immobilized enzymes on MWCNTs and octylsepharose supports. The immobilized biocatalyst used for constructing the biosensor demonstrated high sensitivity and increased stability compared to previously reported lipase-based biosensors.

The advantages of different nanostructured films obtained by the SP technique for sensor applications reside in their tuneable properties, large surface area, higher sensitivity, selectivity, and stability. Researchers and engineers can use the capabilities of the technique to develop innovative sensors with enhanced performance and features tailored to meet the specific demands of various sensing applications.

4. Final Remarks

The central idea of modifying surfaces with thin films lies in the functionalities resulting from the synergistic effect of combined materials. Coatings through drop-casting of mixtures may not fully harness the potential of this synergic effect. Some techniques ensure a certain level of molecular organization as well as control over other supramolecular arrangements. As a result, the properties can be fine-tuned through the manipulation of experimental parameters. Different organizations dictate the film's properties and, consequently, its performance as a sensor. The LB technique, although requiring relatively expensive equipment and being a laborious and time-consuming technique, persists due to the possibility of fine control over molecular organization. The LbL technique continues to be greatly used to produce multilayered thin films mainly due to its experimental simplicity. Versatility is another term to define the LbL technique since substrates of any form or size can be coated, and an infinite number of materials can be suspended as homogeneous suspensions to be assembled as an LbL film. On the other hand, ED techniques have gained prominence owing to their inherent simplicity, cost-effectiveness, rapidity, environmental sustainability, manufacturability as well as scalability. This process offers advantages across

a wide range of materials suitable for film deposition. However, it is important to note that the material of interest must possess electrochemical activity, and naturally, the substrate on which the deposition takes place should be conductive. The SP technique stands out for its simplicity, versatility, efficiency, and low operational cost. Hybrid films can be formed by precursor mixtures or intercalating suspensions to form multilayers. The main disadvantages of the SP technique are the low yield of the solutions (waste of material) and the need to control the chemical reactions that occur during the pyrolysis process. The strong influence of the deposition parameters can be interpreted as an advantage or a disadvantage. Morphological, structural, and electrical properties can be tuned but demand an extensive study of many deposition parameters. Still, SP does not reach the ideal of being able to manufacture very organized and reproducible films. Although it was challenging to compile all of the work and ideas related to ultra-thin film applications as sensors in recent years, we have attempted to gather important information about the molecular organization and its relationship to sensor performance. Each technique presents its characteristics, and all of them will still have a long future in sensor development.

Author Contributions: Conceptualization, C.M.M., C.S.M., M.S.O., H.S.K., C.J.L.C. and P.A.; methodology, C.M.M., C.S.M., M.S.O., H.S.K., C.J.L.C. and P.A.; investigation, C.M.M., C.S.M., M.S.O. and H.S.K.; resources, C.J.L.C. and P.A.; writing—original draft preparation, C.M.M., C.S.M., M.S.O. and H.S.K.; writing—review and editing, C.M.M., C.S.M., M.S.O., C.J.L.C. and P.A.; visualization, C.M.M., C.S.M., M.S.O., H.S.K., C.J.L.C. and P.A.; supervision, C.J.L.C. and P.A.; project administration, C.J.L.C. and P.A.; funding acquisition, C.J.L.C. and P.A. All authors have read and agreed to the published version of the manuscript.

Funding: This research was funded by FAPESP, grant number 2018/22214-6, 2020/11803-0, 2021/01161-4, 2021/14235-6, UNESP/PROPe 04/2022 (C.S.M.) and 13/2022 (C.M.M.), CNPq (422163/2018-0, 316535/2021-4 and 306501/2022-8) and INCT/INEO (CNPq process number 465572/2014-6, FAPESP 2014/50869-6, and CAPES 23038.000776/201754).

Institutional Review Board Statement: Not applicable.

Informed Consent Statement: Not applicable.

Data Availability Statement: The data presented in this study are available on request from the corresponding author.

Acknowledgments: The authors thank FAPESP, UNESP and INCT/INEO.

Conflicts of Interest: The authors declare no conflict of interest.

References

1. Hulanicki, A.; Glab, S.; Ingman, F. Chemical Sensors Definitions and Classification. *Pure Appl. Chem.* **1991**, *63*, 1247–1250. [[CrossRef](#)]
2. Paixao, T.R.L.C.; Reddy, S.M. *Materials for Chemical Sensing*; Springer: Berlin/Heidelberg, Germany, 2017; ISBN 978-3-319-47833-3.
3. Lehn, J.M. Supramolecular Chemistry. *Science* **1993**, *260*, 1762–1763. [[CrossRef](#)]
4. Decher, G. Fuzzy Nanoassemblies: Toward Layered Polymeric Multicomposites. *Science* **1997**, *277*, 1232–1237. [[CrossRef](#)]
5. Petty, M.C. *Langmuir-Blodgett Films: An Introduction*, 1st ed.; Cambridge University Press: Cambridge, UK, 1996; ISBN 9780521413961.
6. Oliveira, O.N.; Caseli, L.; Ariga, K. The Past and the Future of Langmuir and Langmuir-Blodgett Films. *Chem. Rev.* **2022**, *122*, 6459–6513. [[CrossRef](#)] [[PubMed](#)]
7. Rubira, R.J.G.; Aoki, P.H.B.; Constantino, C.J.L.; Alessio, P. Supramolecular Architectures of Iron Phthalocyanine Langmuir-Blodgett Films: The Role Played by the Solution Solvents. *Appl. Surf. Sci.* **2017**, *416*, 482–491. [[CrossRef](#)]
8. Aroca, R.; Thedchanamoorthy, A. Vibrational Studies of Molecular Organization in Evaporated Phthalocyanine Thin Solid Films. *Chem. Mater.* **1995**, *7*, 69–74. [[CrossRef](#)]
9. Alessio, P.; Apetrei, C.; Rubira, R.J.G.; Constantino, C.J.L.; Medina-Plaza, C.; De Saja, J.A.; Rodríguez-Méndez, M.L. Structural and Electrochemical Properties of Lutetium Bis-Octachloro-Phthalocyaninate Nanostructured Films. Application as Voltammetric Sensors. *J. Nanosci. Nanotechnol.* **2014**, *14*, 6754–6763. [[CrossRef](#)] [[PubMed](#)]
10. Martin, C.S.; Alessio, P.; Crespilho, F.N.; Constantino, C.J.L. Supramolecular Arrangement of Iron Phthalocyanine in Langmuir-Schaefer and Electrodeposited Thin Films. *J. Nanosci. Nanotechnol.* **2018**, *18*, 3206–3217. [[CrossRef](#)]

11. Furini, L.N.; Martin, C.S.; Camacho, S.A.; Rubira, R.J.G.; Fernandes, J.D.; Silva, E.A.; Gomes, T.C.; Stunges, G.M.; Constantino, C.J.L.; Alessio, P. Electrochemical Properties of Nickel Phthalocyanine: The Effect of Thin Film Morphology Tuned by Deposition Techniques. *Thin Solid Films* **2020**, *699*, 137897. [[CrossRef](#)]
12. Roy, D.; Das, N.M.; Shakti, N.; Gupta, P.S. Comparative Study of Optical, Structural and Electrical Properties of Zinc Phthalocyanine Langmuir-Blodgett Thin Film on Annealing. *RSC Adv.* **2014**, *4*, 42514–42522. [[CrossRef](#)]
13. Greenler, R.G.; Slager, T.L. Method for Obtaining the Raman Spectrum of a Thin Film on a Metal Surface. *Spectrochim. Acta Part A Mol. Spectrosc.* **1973**, *29*, 193–201. [[CrossRef](#)]
14. Greenler, R.G. Infrared Study of Adsorbed Molecules on Metal Surfaces by Reflection Techniques. *J. Chem. Phys.* **1966**, *44*, 310–315. [[CrossRef](#)]
15. Hasegawa, T. *Quantitative Infrared Spectroscopy for Understanding of a Condensed Matter*; Springer: Tokyo, Japan, 2017; ISBN 9784431564935.
16. Debe, M.K. Optical Probes of Organic Thin Films: Photons-in and Photons-Out. *Prog. Surf. Sci.* **1987**, *24*, 1–282. [[CrossRef](#)]
17. Frątczak, E.Z.; Uznański, P.; Moneta, M.E. Characterization of Molecular Organization in Pentacene Thin Films on SiO₂ Surface Using Infrared Spectroscopy, Spectroscopic Ellipsometry, and Atomic Force Microscopy. *Chem. Phys.* **2015**, *456*, 49–56. [[CrossRef](#)]
18. Bieri, M.; Bürgi, T. Adsorption Kinetics, Orientation, and Self-Assembling of N-Acetyl-L-Cysteine on Gold: A Combined ATR-IR, PM-IRRAS, and QCM Study. *J. Phys. Chem. B* **2005**, *109*, 22476–22485. [[CrossRef](#)] [[PubMed](#)]
19. Osawa, M.; Ataka, K.I.; Yoshii, K.; Yotsuyanagi, T. Surface-Enhanced Infrared ATR Spectroscopy for in Situ Studies of Electrode/Electrolyte Interfaces. *J. Electron Spectros. Relat. Phenomena* **1993**, *64–65*, 371–379. [[CrossRef](#)]
20. Hutter, E.; Assiongbon, K.A.; Fendler, J.H.; Roy, D. Fourier Transform Infrared Spectroscopy Using Polarization Modulation and Polarization Selective Techniques for Internal and External Reflection Geometries: Investigation of Self-Assembled Octadecylmercaptan on a Thin Gold Film. *J. Phys. Chem. B* **2003**, *107*, 7812–7819. [[CrossRef](#)]
21. Lang, P.; Hajlaoui, R.; Garnier, F.; Desbat, B.; Buffeteau, T.; Horowitz, G.; Yassar, A. IR Spectroscopy Evidence for a Substrate-Dependent Organization of Sexithiophene Thin Films Vacuum Evaporated onto SiH/Si and SiO₂/Si. *J. Phys. Chem.* **1995**, *99*, 5492–5499. [[CrossRef](#)]
22. Zanfolim, A.A.; Volpati, D.; Olivati, C.A.; Job, A.E.; Constantino, C.J.L. Structural and Electric-Optical Properties of Zinc Phthalocyanine Evaporated Thin Films: Temperature and Thickness Effects. *J. Phys. Chem. C* **2010**, *114*, 12290–12299. [[CrossRef](#)]
23. Zawisza, I.; Wittstock, G.; Boukherroub, R.; Szunerits, S. Polarization Modulation Infrared Reflection Absorption Spectroscopy Investigations of Thin Silica Films Deposited on Gold. 2. Structural Analysis of a 1,2-Dimyristoyl-Sn-Glycero-3-Phosphocholine Bilayer. *Langmuir* **2008**, *24*, 3922–3929. [[CrossRef](#)]
24. Umemura, J.; Kamata, T.; Kawai, T.; Takenaka, T. Quantitative Evaluation of Molecular Orientation in Thin Langmuir-Blodgett Films by FT-IR Transmission and Reflection-Absorption Spectroscopy. *J. Phys. Chem.* **1990**, *94*, 62–67. [[CrossRef](#)]
25. Früh, A.; Rutkowski, S.; Akimchenko, I.O.; Tverdokhlebov, S.I.; Frueh, J. Orientation Analysis of Polymer Thin Films on Metal Surfaces via IR Absorbance of the Relative Transition Dipole Moments. *Appl. Surf. Sci.* **2022**, *594*, 153476. [[CrossRef](#)]
26. Hasegawa, T.; Takeda, S.; Kawaguchi, A.; Umemura, J. Quantitative Analysis of Uniaxial Molecular Orientation in Langmuir-Blodgett Films by Infrared Reflection Spectroscopy. *Langmuir* **1995**, *11*, 1236–1243. [[CrossRef](#)]
27. Shioya, N.; Fujiwara, R.; Tomita, K.; Shimoaka, T.; Hasegawa, T. Simultaneous Analysis of Molecular Orientation and Quantity Change of Constituents in a Thin Film Using PMAIRS. *J. Phys. Chem. A* **2020**, *124*, 2714–2720. [[CrossRef](#)] [[PubMed](#)]
28. Wang, C.; Sharma, S.K.; Olaluwoye, O.S.; Alrashdi, S.A.; Hasegawa, T.; Leblanc, R.M. Conformation Change of α -Synuclein(61–95) at the Air-Water Interface and Quantitative Measurement of the Tilt Angle of Its α -Helix by Multiple Angle Incidence Resolution Spectroscopy. *Colloids Surf. B Biointerfaces* **2019**, *183*, 110401. [[CrossRef](#)] [[PubMed](#)]
29. Shioya, N.; Shimoaka, T.; Murdey, R.; Hasegawa, T. Accurate Molecular Orientation Analysis Using Infrared P-Polarized Multiple-Angle Incidence Resolution Spectrometry (PMAIRS) Considering the Refractive Index of the Thin Film Sample. *Appl. Spectrosc.* **2017**, *71*, 1242–1248. [[CrossRef](#)] [[PubMed](#)]
30. da Silva, E.A.; Caseli, L.; de Almeida Olivati, C. Organization of Polythiophenes at Ultrathin Films Mixed with Stearic Acid Investigated with Polarization-Modulation Infrared Reflection–Absorption Spectroscopy. *Colloids Surf. A Physicochem. Eng. Asp.* **2017**, *529*, 628–633. [[CrossRef](#)]
31. Brosseau, C.L.; Leitch, J.; Bin, X.; Chen, M.; Roscoe, S.G.; Lipkowski, J. Electrochemical and PM-IRRAS a Glycolipid-Containing Biomimetic Membrane Prepared Using Langmuir-Blodgett/Langmuir-Schaefer Deposition. *Langmuir* **2008**, *24*, 13058–13067. [[CrossRef](#)]
32. Sang, L.; Mudalige, A.; Sigdel, A.K.; Giordano, A.J.; Marder, S.R.; Berry, J.J.; Pemberton, J.E. PM-IRRAS Determination of Molecular Orientation of Phosphonic Acid Self-Assembled Monolayers on Indium Zinc Oxide. *Langmuir* **2015**, *31*, 5603–5613. [[CrossRef](#)]
33. Milosevic, M.; Berets, S.L.; Fadeev, A.Y. Single-Reflection Attenuated Total Reflection of Organic Monolayers on Silicon. *Appl. Spectrosc.* **2003**, *57*, 724–727. [[CrossRef](#)]
34. Aroca, R. *Surface-Enhanced Vibrational Spectroscopy*; Wiley: Hoboken, NJ, USA, 2006; ISBN 9780471607311.
35. Tanaka, M.; Young, R.J. Review Polarised Raman Spectroscopy for the Study of Molecular Orientation Distributions in Polymers. *J. Mater. Sci.* **2006**, *41*, 963–991. [[CrossRef](#)]
36. Svenningsson, L.; Nordstierna, L. Polarized Raman Spectroscopy Strategy for Molecular Orientation of Polymeric Fibers with Raman Tensors Deviating from the Molecular Frame. *ACS Appl. Polym. Mater.* **2020**, *2*, 4809–4813. [[CrossRef](#)]

37. Li, Z.; Young, R.J.; Wilson, N.R.; Kinloch, I.A.; Vallés, C.; Li, Z. Effect of the Orientation of Graphene-Based Nanoplatelets upon the Young's Modulus of Nanocomposites. *Compos. Sci. Technol.* **2016**, *123*, 125–133. [[CrossRef](#)]
38. Zhang, S.; Mao, N.; Zhang, N.; Wu, J.; Tong, L.; Zhang, J. Anomalous Polarized Raman Scattering and Large Circular Intensity Differential in Layered Triclinic ReS₂. *ACS Nano* **2017**, *11*, 10366–10372. [[CrossRef](#)] [[PubMed](#)]
39. Sereda, V.; Ralbovsky, N.M.; Vasudev, M.C.; Naik, R.R.; Igor, K.; States, U.; States, U.; Branch, M.M.; Directorate, M.; Air, W.; et al. Polarized Raman Spectroscopy for Determining the Orientation of Di-D-Phenylalanine Molecules in a Nanotube. *J. Raman Spectrosc.* **2016**, *47*, 1056–1062. [[CrossRef](#)]
40. Liu, T.; Kumar, S. Quantitative Characterization of SWNT Orientation by Polarized Raman Spectroscopy. *Chem. Phys. Lett.* **2003**, *378*, 257–262. [[CrossRef](#)]
41. Xu, B.; Mao, N.; Zhao, Y.; Tong, L.; Zhang, J. Polarized Raman Spectroscopy for Determining Crystallographic Orientation of Low-Dimensional Materials. *J. Phys. Chem. Lett.* **2021**, *12*, 7442–7452. [[CrossRef](#)]
42. Li, Z.; Young, R.J.; Kinloch, I.A.; Wilson, N.R.; Marsden, A.J.; Raju, A.P.A. Quantitative Determination of the Spatial Orientation of Graphene by Polarized Raman Spectroscopy. *Carbon N. Y.* **2015**, *88*, 215–224. [[CrossRef](#)]
43. Diego Fernandes, J.; Maximino, M.D.; Braunger, M.L.; Pereira, M.S.; De Almeida Olivati, C.; Constantino, C.J.L.; Alessio, P. Supramolecular Architecture and Electrical Conductivity in Organic Semiconducting Thin Films. *Phys. Chem. Chem. Phys.* **2020**, *22*, 13554–13562. [[CrossRef](#)]
44. Garcia, M.P.B.; Martin, C.S.; Kavazoi, H.S.; Maximino, M.D.; Alessio, P. Perylene Nanostructured Films Optimization for Organic Electronics: Molecular, Structural, and Electrochemical Characterization. *Thin Solid Films* **2023**, *777*, 139895. [[CrossRef](#)]
45. Hupfer, M.L.; Meyer, R.; Deckert-Gaudig, T.; Ghosh, S.; Skabeev, A.; Peneva, K.; Deckert, V.; Dietzek, B.; Presselt, M. Supramolecular Reorientation during Deposition Onto Metal Surfaces of Quasi-Two-Dimensional Langmuir Monolayers Composed of Bifunctional Amphiphilic, Twisted Perylenes. *Langmuir* **2021**, *37*, 11018–11026. [[CrossRef](#)] [[PubMed](#)]
46. Ma, Y.; Wang, B.; Wu, Y.; Huang, Y.; Chen, Y. The Production of Horizontally Aligned Single-Walled Carbon Nanotubes. *Carbon N. Y.* **2011**, *49*, 4098–4110. [[CrossRef](#)]
47. Ackermann, T.; Neuhaus, R.; Roth, S. The Effect of Rod Orientation on Electrical Anisotropy in Silver Nanowire Networks for Ultra-Transparent Electrodes. *Sci. Rep.* **2016**, *6*, 34289. [[CrossRef](#)]
48. Miao, J.; Lin, J.Y.S. Nanometer-Thick Films of Aligned ZnO Nanowires Sensitized with Au Nanoparticles for Few-Ppb-Level Acetylene Detection. *ACS Appl. Nano Mater.* **2020**, *3*, 9174–9184. [[CrossRef](#)]
49. Bunaciu, A.A.; Udriștioiu, E.G.; Aboul-Enein, H.Y. X-Ray Diffraction: Instrumentation and Applications. *Crit. Rev. Anal. Chem.* **2015**, *45*, 289–299. [[CrossRef](#)] [[PubMed](#)]
50. Rivalta, A.; Albonetti, C.; Biancone, D.; Della Ciana, M.; d'Agostino, S.; Biniek, L.; Brinkmann, M.; Giunchi, A.; Salzillo, T.; Brillante, A.; et al. Growth, Morphology and Molecular Orientation of Controlled Indigo Thin Films on Silica Surfaces. *Surf. Interfaces* **2021**, *24*, 101058. [[CrossRef](#)]
51. Dynarowicz-Łątka, P.; Dhanabalan, A.; Oliveira, O.N. Modern Physicochemical Research on Langmuir Monolayers. *Adv. Colloid Interface Sci.* **2001**, *91*, 221–293. [[CrossRef](#)]
52. Riul, A.; Miyazaki, C.M.; Dantas, C.A.; Oliveira, O.N.; Lvova, L.; Kirsanov, D.; DiNatale, C.; Legin, A. The Use of Nanostructured Films in Sensing Applications. In *Multisensor Systems for Chemical Analysis*; Lvova, L., Kirsanov, D., Di Natale, C., Legin, A., Eds.; Jenny Stanford Publishing: Dubai, United Arab Emirates, 2014; pp. 320–349, ISBN 978-981-4411-15-8.
53. Mendelsohn, R.; Mao, G.; Flach, C.R. Infrared Reflection-Absorption Spectroscopy: Principles and Applications to Lipid-Protein Interaction in Langmuir Films. *Biochim. Biophys. Acta-Biomembr.* **2010**, *1798*, 788–800. [[CrossRef](#)]
54. Cohen Stuart, M.A.; Wegh, R.A.J.; Kroon, J.M.; Sudhölter, E.J.R. Design and Testing of a Low-Cost and Compact Brewster Angle Microscope. *Langmuir* **1996**, *12*, 2863–2865. [[CrossRef](#)]
55. Ulman, A. *An Introduction to Ultrathin Organic Films: From Langmuir–Blodgett to Self-Assembly*; Academic Press: San Diego, CA, USA, 1991.
56. Miyazaki, C.M.; De Barros, A.; Mascagni, D.B.T.; Graça, J.S.; Campos, P.P.; Ferreira, M. *Self-Assembly Thin Films for Sensing*; Springer: Cham, Switzerland, 2016; ISBN 9783319478357.
57. Hussain, S.A.; Dey, B.; Bhattacharjee, D.; Mehta, N. Unique Supramolecular Assembly through Langmuir–Blodgett (LB) Technique. *Heliyon* **2018**, *4*, e01038. [[CrossRef](#)]
58. Saha, S.; Dutta, B.; Ghosh, M.; Chowdhury, J. Adsorption of 4-Mercapto Pyridine with Gold Nanoparticles Embedded in the Langmuir–Blodgett Film Matrix of Stearic Acid: SERS, XPS Studies Aided by Born-Oppenheimer on the Fly Dynamics, Time-Resolved Wavelet Transform Theory, and DFT. *ACS Omega* **2022**, *7*, 27818–27830. [[CrossRef](#)] [[PubMed](#)]
59. Swierczewski, M.; Bürgi, T. Langmuir and Langmuir-Blodgett Films of Gold and Silver Nanoparticles. *Langmuir* **2022**, *39*, 2135–2151. [[CrossRef](#)] [[PubMed](#)]
60. Tahghighi, M.; Mannelli, I.; Janner, D.; Ignés-Mullol, J. Tailoring Plasmonic Response by Langmuir–Blodgett Gold Nanoparticle Templating for the Fabrication of SERS Substrates. *Appl. Surf. Sci.* **2018**, *447*, 416–422. [[CrossRef](#)]
61. Tahghighi, M.; Janner, D.; Ignés-Mullol, J. Optimizing Gold Nanoparticle Size and Shape for the Fabrication of SERS Substrates by Means of the Langmuir–Blodgett Technique. *Nanomaterials* **2020**, *10*, 2264. [[CrossRef](#)] [[PubMed](#)]
62. Zhang, J.; Wang, M.; Yang, Z.; Zhang, X. Highly Flexible and Stretchable Strain Sensors Based on Conductive Whisker Carbon Nanotube Films. *Carbon N. Y.* **2021**, *176*, 139–147. [[CrossRef](#)]

63. Abdulla, S.; Pullithadathil, B. Unidirectional Langmuir-Blodgett-Mediated Alignment of Polyaniline-Functionalized Multiwalled Carbon Nanotubes for NH₃gas Sensor Applications. *Langmuir* **2020**, *36*, 11618–11628. [[CrossRef](#)]
64. Yin, Z.; Ding, A.; Zhang, H.; Zhang, W. The Relevant Approaches for Aligning Carbon Nanotubes. *Micromachines* **2022**, *13*, 1863. [[CrossRef](#)] [[PubMed](#)]
65. Giancane, G.; Bettini, S.; Valli, L. State of Art in the Preparation, Characterisation and Applications of Langmuir-Blodgett Films of Carbon Nanotubes. *Colloids Surfaces A Physicochem. Eng. Asp.* **2010**, *354*, 81–90. [[CrossRef](#)]
66. Solanki, S.; Soni, A.; Agrawal, V.V.; Pandey, M.K.; Sumana, G. Ultrasensitive Immunosensor Based on Langmuir-Blodgett Deposited Ordered Graphene Assemblies for Dengue Detection. *Langmuir* **2021**, *37*, 8705–8713. [[CrossRef](#)]
67. Jaafar, M.M.; Ciniciato, G.P.M.K.; Ibrahim, S.A.; Phang, S.M.; Yunus, K.; Fisher, A.C.; Iwamoto, M.; Vengadesh, P. Preparation of a Three-Dimensional Reduced Graphene Oxide Film by Using the Langmuir-Blodgett Method. *Langmuir* **2015**, *31*, 10426–10434. [[CrossRef](#)]
68. Kouloumpis, A.; Thomou, E.; Chalmpes, N.; Dimos, K.; Spyrou, K.; Bourlinos, A.B.; Koutselas, I.; Gournis, D.; Rudolf, P. Graphene/Carbon Dot Hybrid Thin Films Prepared by a Modified Langmuir-Schaefer Method. *ACS Omega* **2017**, *2*, 2090–2099. [[CrossRef](#)] [[PubMed](#)]
69. Scholl, F.A.; Siqueira, J.R.; Caseli, L. Graphene Oxide Modulating the Bioelectronic Properties of Penicillinase Immobilized in Lipid Langmuir-Blodgett Films. *Langmuir* **2022**, *38*, 2372–2378. [[CrossRef](#)] [[PubMed](#)]
70. Saha, S.; Chowdhury, J. Sustained and Improved Enzymatic Activity of Trypsin Immobilized in the Langmuir Blodgett Film of DPPC: A Rapid Enzyme Sensor for the Detection of Azocasein. *Mater. Chem. Phys.* **2020**, *243*, 122647. [[CrossRef](#)]
71. de Souza Furtado, F.A.; Caseli, L. Enzyme Activity Preservation for Galactose Oxidase Immobilized in Stearic Acid Langmuir-Blodgett Films. *Thin Solid Films* **2020**, *709*, 138253. [[CrossRef](#)]
72. Sinha, R.; Das, S.K.; Ghosh, M.; Chowdhury, J. Self-Assembled Gold Nanoparticles on the Serpentine Networks of Calf Thymus-DNA Langmuir-Blodgett Films as Efficient SERS Sensing Platform: Fabrication and Its Application in Thiram Detection. *Mater. Chem. Phys.* **2023**, *295*, 127140. [[CrossRef](#)]
73. Andrés, M.A.; Vijjapu, M.T.; Surya, S.G.; Shekhah, O.; Salama, K.N.; Serre, C.; Eddaoudi, M.; Roubeau, O.; Gascón, I. Methanol and Humidity Capacitive Sensors Based on Thin Films of MOF Nanoparticles. *ACS Appl. Mater. Interfaces* **2020**, *12*, 4155–4162. [[CrossRef](#)] [[PubMed](#)]
74. Zhang, T.; Zheng, B.; Li, L.; Song, J.; Song, L.; Zhang, M. Fewer-Layer Conductive Metal-Organic Langmuir-Blodgett Films as Electrocatalysts Enable an Ultralow Detection Limit of H₂O₂. *Appl. Surf. Sci.* **2021**, *539*, 148255. [[CrossRef](#)]
75. da Rocha Rodrigues, R.; da Silva, R.L.C.G.; Caseli, L.; Péres, L.O. Conjugated Polymers as Langmuir and Langmuir-Blodgett Films: Challenges and Applications in Nanostructured Devices. *Adv. Colloid Interface Sci.* **2020**, *285*, 102277. [[CrossRef](#)]
76. Ly, T.N.; Park, S. Highly Sensitive Gas Sensor Using Hierarchically Self-Assembled Thin Films of Graphene Oxide and Gold Nanoparticles. *J. Ind. Eng. Chem.* **2018**, *67*, 417–428. [[CrossRef](#)]
77. Ma, K.; Wang, R.; Rao, Y.; Zhao, W.; Liu, S.; Jiao, T. Langmuir-Blodgett Films of Two Chiral Perylene Bisimide-Based Molecules: Aggregation and Supramolecular Chirality. *Colloids Surfaces A Physicochem. Eng. Asp.* **2020**, *591*, 124563. [[CrossRef](#)]
78. Kouloumpis, A.; Vourdas, N.; Zygouri, P.; Chalmpes, N.; Potsi, G.; Kostas, V.; Spyrou, K.; Stathopoulos, V.N.; Gournis, D.; Rudolf, P. Controlled Deposition of Fullerene Derivatives within a Graphene Template by Means of a Modified Langmuir-Schaefer Method. *J. Colloid Interface Sci.* **2018**, *524*, 388–398. [[CrossRef](#)] [[PubMed](#)]
79. Chalmpes, N.; Patila, M.; Kouloumpis, A.; Alatzoglou, C.; Spyrou, K.; Subrati, M.; Polydera, A.C.; Bourlinos, A.B.; Stamatis, H.; Gournis, D. Graphene Oxide-Cytochrome c Multilayered Structures for Biocatalytic Applications: Decrypting the Role of Surfactant in Langmuir-Schaefer Layer Deposition. *ACS Appl. Mater. Interfaces* **2022**, *14*, 26204–26215. [[CrossRef](#)] [[PubMed](#)]
80. Gür, B.; Ayhan, M.E.; Türkhan, A.; Gür, F.; Kaya, E.D. A Facile Immobilization of Polyphenol Oxidase Enzyme on Graphene Oxide and Reduced Graphene Oxide Thin Films: An Insight into in-Vitro Activity Measurements and Characterization. *Colloids Surfaces A Physicochem. Eng. Asp.* **2019**, *562*, 179–185. [[CrossRef](#)]
81. Cote, L.J.; Kim, F.; Huang, J. Langmuir-Blodgett Assembly of Graphite Oxide Single Layers. *J. Am. Chem. Soc.* **2009**, *131*, 1043–1049. [[CrossRef](#)] [[PubMed](#)]
82. Silverberg, G.J.; Vecitis, C.D. Wrinkling and Periodic Folding of Graphene Oxide Monolayers by Langmuir-Blodgett Compression. *Langmuir* **2017**, *33*, 9880–9888. [[CrossRef](#)] [[PubMed](#)]
83. Hu, H.; Wang, S.; Feng, X.; Pauly, M.; Decher, G.; Long, Y. In-Plane Aligned Assemblies of 1D-Nanoobjects: Recent Approaches and Applications. *Chem. Soc. Rev.* **2020**, *49*, 509–553. [[CrossRef](#)] [[PubMed](#)]
84. Wang, L.; Li, Y.; Wang, Q.; Zou, L.; Ye, B. The Construction of Well-Aligned MWCNTs-PANI Langmuir-Blodgett Film Modified Glassy Carbon Electrode and Its Analytical Application. *Sensors Actuators, B Chem.* **2016**, *228*, 214–220. [[CrossRef](#)]
85. Bonatout, N.; Muller, F.; Fontaine, P.; Gascon, I.; Kononov, O.; Goldmann, M. How Exfoliated Graphene Oxide Nanosheets Organize at the Water Interface: Evidence for a Spontaneous Bilayer Self-Assembly. *Nanoscale* **2017**, *9*, 12543–12548. [[CrossRef](#)]
86. Zheng, Q.; Ip, W.H.; Lin, X.; Yousefi, N.; Yeung, K.K.; Li, Z.; Kim, J.K. Consisting of Ultralarge Graphene Sheets Produced by Langmuir A Blodgett Assembly. *ACS Nano* **2011**, *5*, 6039–6051. [[CrossRef](#)]
87. Mujica, M.L.; Zhang, Y.; Bédoui, F.; Gutiérrez, F.; Rivas, G. Label-Free Graphene Oxide-Based SPR Genosensor for the Quantification of MicroRNA21. *Anal. Bioanal. Chem.* **2020**, *412*, 3539–3546. [[CrossRef](#)]
88. Liu, B.; Salgado, S.; Maheshwari, V.; Liu, J. DNA Adsorbed on Graphene and Graphene Oxide: Fundamental Interactions, Desorption and Applications. *Curr. Opin. Colloid Interface Sci.* **2016**, *26*, 41–49. [[CrossRef](#)]

89. Gulotta, F.A.; Paz Zanini, V.I.; López de Mishima, B.A.; Martino, D.M.; Linarez Pérez, O.E.; Ferreyra, N.F. Electrostatically Mediated Layer-by-Layer Assembly of a Bioinspired Thymine Polycation and Gold Nanoparticles. *J. Electroanal. Chem.* **2021**, *883*, 114895. [[CrossRef](#)]
90. Upan, J.; Youngvises, N.; Tuantranont, A.; Karuwan, C.; Banet, P.; Aubert, P.H.; Jakmunee, J. A Simple Label-Free Electrochemical Sensor for Sensitive Detection of Alpha-Fetoprotein Based on Specific Aptamer Immobilized Platinum Nanoparticles/Carboxylated-Graphene Oxide. *Sci. Rep.* **2021**, *11*, 13969. [[CrossRef](#)] [[PubMed](#)]
91. Miyazaki, C.M.; Camilo, D.E.; Shimizu, F.M.; Ferreira, M. Improved Antibody Loading on Self-Assembled Graphene Oxide Films for Using in Surface Plasmon Resonance Immunosensors. *Appl. Surf. Sci.* **2019**, *490*, 502–509. [[CrossRef](#)]
92. Miyazaki, C.M.; Mishra, R.; Kinahan, D.J.; Ferreira, M.; Ducrée, J. Polyethylene Imine/Graphene Oxide Layer-by-Layer Surface Functionalization for Significantly Improved Limit of Detection and Binding Kinetics of Immunoassays on Acrylate Surfaces. *Colloids Surfaces B Biointerfaces* **2017**, *158*, 167–174. [[CrossRef](#)] [[PubMed](#)]
93. Nangare, S.; Patil, P. Poly(Allylamine) Coated Layer-by-Layer Assembly Decorated 2D Carbon Backbone for Highly Sensitive and Selective Detection of Tau-441 Using Surface Plasmon Resonance Biosensor. *Anal. Chim. Acta* **2023**, *1271*, 341474. [[CrossRef](#)] [[PubMed](#)]
94. Massey, M.K.; Pearson, C.; Zeze, D.A.; Mendis, B.G.; Petty, M.C. The Electrical and Optical Properties of Oriented Langmuir-Blodgett Films of Single-Walled Carbon Nanotubes. *Carbon N. Y.* **2011**, *49*, 2424–2430. [[CrossRef](#)]
95. Baratto, C.; Golovanova, V.; Faglia, G.; Hakola, H.; Niemi, T.; Tkachenko, N.; Nazarchuk, B.; Golovanov, V. On the Alignment of ZnO Nanowires by Langmuir-Blodgett Technique for Sensing Application. *Appl. Surf. Sci.* **2020**, *528*, 146959. [[CrossRef](#)]
96. Wang, L.; Li, Y.; Li, G.; Ye, B. A New Strategy for Enhancing Electrochemical Sensing from MWCNTs Modified Electrode with Langmuir-Blodgett Film and Used in Determination of Methylparaben. *Sensors Actuators, B Chem.* **2015**, *211*, 332–338. [[CrossRef](#)]
97. He, Z.; Wang, J.L.; Chen, S.M.; Liu, J.W.; Yu, S.H. Self-Assembly of Nanowires: From Dynamic Monitoring to Precision Control. *Acc. Chem. Res.* **2022**, *55*, 1480–1491. [[CrossRef](#)]
98. Bodik, M.; Maxian, O.; Hagara, J.; Nadazdy, P.; Jergel, M.; Majkova, E.; Siffalovic, P. Langmuir-Scheaffer Technique as a Method for Controlled Alignment of 1D Materials. *Langmuir* **2020**, *36*, 4540–4547. [[CrossRef](#)] [[PubMed](#)]
99. Gupta, N.; Gupta, S.M.; Sharma, S.K. Carbon Nanotubes: Synthesis, Properties and Engineering Applications. *Carbon Lett.* **2019**, *29*, 419–447. [[CrossRef](#)]
100. Rathinavel, S.; Priyadharshini, K.; Panda, D. A Review on Carbon Nanotube: An Overview of Synthesis, Properties, Functionalization, Characterization, and the Application. *Mater. Sci. Eng. B* **2021**, *268*, 115095. [[CrossRef](#)]
101. Bian, R.; Meng, L.; Zhang, M.; Chen, L.; Liu, H. Aligning One-Dimensional Nanomaterials by Solution Processes. *ACS Omega* **2019**, *4*, 1816–1823. [[CrossRef](#)] [[PubMed](#)]
102. Li, X.; Zhang, L.; Wang, X.; Shimoyama, I.; Sun, X.; Seo, W.K.; Dai, H. Langmuir-Blodgett Assembly of Densely Aligned Single-Walled Carbon Nanotubes from Bulk Materials. *J. Am. Chem. Soc.* **2007**, *129*, 4890–4891. [[CrossRef](#)] [[PubMed](#)]
103. Tao, A.; Kim, F.; Hess, C.; Goldberger, J.; He, R.; Sun, Y.; Xia, Y.; Yang, P. Langmuir-Blodgett Silver Nanowire Monolayers for Molecular Sensing Using Surface-Enhanced Raman Spectroscopy. *Nano Lett.* **2003**, *3*, 1229–1233. [[CrossRef](#)]
104. Sheng, S.Z.; Zheng, S.Q.; Feng, X.F.; Zhou, L.R.; Tao, Z.C.; Liu, J.W. Anisotropic Nanoparticle Arrays Guided by Ordered Nanowire Films Enhance Surface-Enhanced Raman Scattering. *Adv. Opt. Mater.* **2023**, *11*, 2201682. [[CrossRef](#)]
105. Saha, S.; Ghosh, M.; Chowdhury, J. Infused Self-Assembly on Langmuir-Blodgett Film: Fabrication of Highly Efficient SERS Active Substrates with Controlled Plasmonic Aggregates. *J. Raman Spectrosc.* **2019**, *50*, 330–344. [[CrossRef](#)]
106. Das, S.K.; Pal, K.; Bhattacharya, T.S.; Karmakar, P.; Chowdhury, J. Fabrication of SERS Active Langmuir-Blodgett Film Substrate for Screening Human Cancer Cell Lines: Experimental Observations Supported by Multivariate Data Analyses. *Sens. Actuators B Chem.* **2019**, *299*, 126962. [[CrossRef](#)]
107. Tramonti, V.; Lofrumento, C.; Martina, M.R.; Lucchesi, G.; Caminati, G. Graphene Oxide/Silver Nanoparticles Platforms for the Detection and Discrimination of Native and Fibrillar Lysozyme: A Combined QCM and SERS Approach. *Nanomaterials* **2022**, *12*, 600. [[CrossRef](#)]
108. Tim, B.; Błaszkiwicz, P.; Nowicka, A.B.; Kotkowiak, M. Optimizing SERS Performance through Aggregation of Gold Nanorods in Langmuir-Blodgett Films. *Appl. Surf. Sci.* **2022**, *573*, 151518. [[CrossRef](#)]
109. Wu, Y.H.; Imae, T.; Ujihara, M. Surface Enhanced Plasmon Effects by Gold Nanospheres and Nanorods in Langmuir-Blodgett Films. *Colloids Surfaces A Physicochem. Eng. Asp.* **2017**, *532*, 213–221. [[CrossRef](#)]
110. Aleksandrovic, V.; Greshnykh, D.; Randjelovic, I.; Frömsdorf, A.; Kornowski, A.; Roth, S.V.; Klinke, C.; Weller, H. Preparation and Electrical Properties of Cobalt-Platinum Nanoparticle Monolayers Deposited by the Langmuir-Blodgett Technique. *ACS Nano* **2008**, *2*, 1123–1130. [[CrossRef](#)] [[PubMed](#)]
111. Tang, J.; Zhao, Q.; Zhang, N.; Man, S.Q. Facile Fabrication of Large-Area and Uniform Silica Nanospheres Monolayer for Efficient Surface-Enhanced Raman Scattering. *Appl. Surf. Sci.* **2014**, *308*, 247–252. [[CrossRef](#)]
112. Tang, J.; Zeng, C.; Wang, Y.; Lin, Z.; Man, S.Q. Langmuir-Blodgett Film of Esterifiable Silica Nanoparticles as Substrates for Surface-Enhanced Raman Scattering. *Plasmonics* **2015**, *10*, 563–568. [[CrossRef](#)]
113. Pandey, C.M.; Pandey, M.K.; Sumana, G. Langmuir-Blodgett Based Ordered Deposition of Functionalized Iron Oxide Nanoparticles for Ultrasensitive Detection of Escherichia Coli O157: H7. *Microchem. J.* **2022**, *181*, 107708. [[CrossRef](#)]

114. Saleh Khasraw, S.; Ghaderi, S.; Raza Saeed, S.; Hallaj, R.; Hassanzadeh, A. Observation of Nanodomains and Nanostripes in the Langmuir-Blodgett Monolayers of Fe₃O₄ Magnetic Nanoparticles. *Mater. Sci. Eng. B Solid-State Mater. Adv. Technol.* **2021**, *273*, 115402. [[CrossRef](#)]
115. Ariga, K. Interfacial Nanoarchitectonics with Porphyrins and Related Molecules: Langmuir-Blodgett Method and Layer-by-Layer Assembly. *J. Porphy. Phthalocyanines* **2023**, *27*, 924–945. [[CrossRef](#)]
116. Maximino, M.D.; Martin, C.S.; Pereira, M.S.; Aléssio, P. Metallic Phthalocyanines: Impact of the Film Deposition Method on Its Supramolecular Arrangement and Sensor Performance. *An. Acad. Bras. Cienc.* **2019**, *91*, 1–14. [[CrossRef](#)]
117. Bettini, S.; Pagano, R.; Borovkov, V.; Giancane, G.; Valli, L. The Role of the Central Metal Ion of Ethane-Bridged Bis-Porphyrins in Histidine Sensing. *J. Colloid Interface Sci.* **2019**, *533*, 762–770. [[CrossRef](#)]
118. Bettini, S.; Grover, N.; Ottolini, M.; Mattern, C.; Valli, L.; Senge, M.O.; Giancane, G. Enantioselective Discrimination of Histidine by Means of an Achiral Cubane-Bridged Bis-Porphyrin. *Langmuir* **2021**, *37*, 13882–13889. [[CrossRef](#)] [[PubMed](#)]
119. Ermakova, E.V.; Koroleva, E.O.; Shokurov, A.V.; Arslanov, V.V.; Bessmertnykh-Lemeune, A. Ultra-Thin Film Sensors Based on Porphyrin-5-Ylphosphonate Diesters for Selective and Sensitive Dual-Channel Optical Detection of Mercury(II) Ions. *Dye. Pigment.* **2021**, *186*, 108967. [[CrossRef](#)]
120. Akyüz, D.; Koca, A. An Electrochemical Sensor for the Detection of Pesticides Based on the Hybrid of Manganese Phthalocyanine and Polyaniline. *Sens. Actuators B Chem.* **2019**, *283*, 848–856. [[CrossRef](#)]
121. Miyazaki, C.M.C.M.; Shimizu, F.M.F.M.; Ferreira, M.; Mejía-Salazar, J.R.; Oliveira, O.N.; Ferreira, M. *Surface Plasmon Resonance (SPR) for Sensors and Biosensors*; William Andrew Publishing: Norwich, NY, USA, 2017; Volume 28, ISBN 9780323497794.
122. de Lucena, N.C.; Miyazaki, C.M.; Shimizu, F.M.; Constantino, C.J.L.; Ferreira, M. Layer-by-Layer Composite Film of Nickel Phthalocyanine and Montmorillonite Clay for Synergistic Effect on Electrochemical Detection of Dopamine. *Appl. Surf. Sci.* **2018**, *436*, 957–966. [[CrossRef](#)]
123. da Silva, V.N.C.; Farias, E.A.D.O.; Araújo, A.R.; Xavier Magalhães, F.E.; Neves Fernandes, J.R.; Teles Souza, J.M.; Eiras, C.; Alves da Silva, D.; Hugo do Vale Bastos, V.; Teixeira, S.S. Rapid and Selective Detection of Dopamine in Human Serum Using an Electrochemical Sensor Based on Zinc Oxide Nanoparticles, Nickel Phthalocyanines, and Carbon Nanotubes. *Biosens. Bioelectron.* **2022**, *210*, 114211. [[CrossRef](#)]
124. Paula-Ayoub, F.; Caseli, L. Controlling the Molecular Architecture of Lactase Immobilized in Langmuir-Blodgett Films of Phospholipids to Modulate the Enzyme Activity. *Colloids Surf. B Biointerfaces* **2017**, *150*, 8–14. [[CrossRef](#)]
125. Girard-Egrot, A.P.; Godoy, S.; Blum, L.J. Enzyme Association with Lipidic Langmuir-Blodgett Films: Interests and Applications in Nanobioscience. *Adv. Colloid Interface Sci.* **2005**, *116*, 205–225. [[CrossRef](#)] [[PubMed](#)]
126. Araujo, F.T.; Peres, L.O.; Caseli, L. Conjugated Polymers Blended with Lipids and Galactosidase as Langmuir-Blodgett Films to Control the Biosensing Properties of Nanostructured Surfaces. *Langmuir* **2019**, *35*, 7294–7303. [[CrossRef](#)]
127. Decher, G.; Hong, J.D.; Schmitt, J. Buildup of Ultrathin Multilayer Films by a Self-Assembly Process: III. Consecutively Alternating Adsorption of Anionic and Cationic Polyelectrolytes on Charged Surfaces. *Thin Solid Films* **1992**, *210–211*, 831–835. [[CrossRef](#)]
128. Schönhoff, M. Layered Polyelectrolyte Complexes: Physics of Formation and Molecular Properties. *J. Phys. Condens. Matter* **2003**, *15*, R1781–R1808. [[CrossRef](#)]
129. Behrens, S.H.; Grier, D.G. The Charge of Glass and Silica Surfaces. *J. Chem. Phys.* **2001**, *115*, 6716–6721. [[CrossRef](#)]
130. Pujari, S.P.; Scheres, L.; Marcelis, A.T.M.; Zuilhof, H. Covalent Surface Modification of Oxide Surfaces. *Angew. Chemie-Int. Ed.* **2014**, *53*, 6322–6356. [[CrossRef](#)] [[PubMed](#)]
131. Alessio, P.; Rodríguez-Méndez, M.L.; De Saja Saez, J.A.; Constantino, C.J.L. Iron Phthalocyanine in Non-Aqueous Medium Forming Layer-by-Layer Films: Growth Mechanism, Molecular Architecture and Applications. *Phys. Chem. Chem. Phys.* **2010**, *12*, 3972–3983. [[CrossRef](#)] [[PubMed](#)]
132. Fernandes, E.G.R.; Brazaca, L.C.; Rodríguez-Mendez, M.L.; de Saja, J.A.; Zucolotto, V. Immobilization of Lutetium Bisphthalocyanine in Nanostructured Biomimetic Sensors Using the LbL Technique for Phenol Detection. *Biosens. Bioelectron.* **2011**, *26*, 4715–4719. [[CrossRef](#)] [[PubMed](#)]
133. Xiang, Y.; Lu, S.; Jiang, S.P. Layer-by-Layer Self-Assembly in the Development of Electrochemical Energy Conversion and Storage Devices from Fuel Cells to Supercapacitors. *Chem. Soc. Rev.* **2012**, *41*, 7291–7321. [[CrossRef](#)] [[PubMed](#)]
134. Guzmán, E.; Ortega, F.; Rubio, R.G. Layer-by-Layer Materials for the Fabrication of Devices with Electrochemical Applications. *Energies* **2022**, *15*, 3399. [[CrossRef](#)]
135. Oliveira, D.A.; Gasparotto, L.H.S.; Siqueira, J.R. Processing of Nanomaterials in Layer-by-Layer Films: Potential Applications in (Bio)Sensing and Energy Storage. *An. Acad. Bras. Cienc.* **2019**, *91*, 1–17. [[CrossRef](#)] [[PubMed](#)]
136. Iost, R.M.; Crespilho, F.N. Layer-by-Layer Self-Assembly and Electrochemistry: Applications in Biosensing and Bioelectronics. *Biosens. Bioelectron.* **2012**, *31*, 1–10. [[CrossRef](#)]
137. Richardson, J.J.; Cui, J.; Björnmalm, M.; Braunger, J.A.; Ejima, H.; Caruso, F. Innovation in Layer-by-Layer Assembly. *Chem. Rev.* **2016**, *116*, 14828–14867. [[CrossRef](#)]
138. Miyazaki, C.M.; Shimizu, F.M.; Ferreira, M. Layer-by-Layer Nanostructured Films for Electrochemical Sensors Fabrication. In *Functionalized Nanomaterial-Based Electrochemical Sensors: Principles, Fabrication Methods, and Applications*; Hussain, C.M., Manjunatha, J.G., Eds.; Woodhead Publishing: Sawston, UK, 2022; pp. 407–441, ISBN 9780128237885.
139. Kurapati, R.; Groth, T.W.; Raichur, A.M. Recent Developments in Layer-by-Layer Technique for Drug Delivery Applications. *ACS Appl. Bio Mater.* **2019**, *2*, 5512–5527. [[CrossRef](#)]

140. Guzmán, E.; Rubio, R.G.; Ortega, F. A Closer Physico-Chemical Look to the Layer-by-Layer Electrostatic Self-Assembly of Polyelectrolyte Multilayers. *Adv. Colloid Interface Sci.* **2020**, *282*, 102197. [[CrossRef](#)] [[PubMed](#)]
141. Lai, W.F.; Wong, W.T.; Rogach, A.L. Molecular Design of Layer-by-Layer Functionalized Liposomes for Oral Drug Delivery. *ACS Appl. Mater. Interfaces* **2020**, *12*, 43341–43351. [[CrossRef](#)] [[PubMed](#)]
142. Shen, J.; Hu, Y.; Li, C.; Qin, C.; Shi, M.; Ye, M. Layer-by-Layer Self-Assembly of Graphene Nanoplatelets. *Langmuir* **2009**, *25*, 6122–6128. [[CrossRef](#)] [[PubMed](#)]
143. Oliveira, D.A.; Molinnus, D.; Beging, S.; Siqueira, J.R.; Schöning, M.J. Biosensor Based on Self-Assembled Films of Graphene Oxide and Polyaniline Using a Field-Effect Device Platform. *Phys. Status Solidi Appl. Mater. Sci.* **2021**, *218*, 2000747. [[CrossRef](#)]
144. Lipton, J.; Weng, G.M.; Röhr, J.A.; Wang, H.; Taylor, A.D. Layer-by-Layer Assembly of Two-Dimensional Materials: Meticulous Control on the Nanoscale. *Matter* **2020**, *2*, 1148–1165. [[CrossRef](#)]
145. Rodrigues, G.H.S.; Miyazaki, C.M.; Rubira, R.J.G.; Constantino, C.J.L.; Ferreira, M. Layer-by-Layer Films of Graphene Nanoplatelets and Gold Nanoparticles for Methyl Parathion Sensing. *ACS Appl. Nano Mater.* **2019**, *2*, 1082–1091. [[CrossRef](#)]
146. Mascagni, D.B.T.; Miyazaki, C.M.; da Cruz, N.C.; de Moraes, M.L.; Riul, A.; Ferreira, M. Layer-by-Layer Assembly of Functionalized Reduced Graphene Oxide for Direct Electrochemistry and Glucose Detection. *Mater. Sci. Eng. C* **2016**, *68*, 739–745. [[CrossRef](#)] [[PubMed](#)]
147. Wu, S.; Hao, J.; Yang, S.; Sun, Y.; Wang, Y.; Zhang, W.; Mao, H.; Song, X.M. Layer-by-Layer Self-Assembly Film of PEI-Reduced Graphene Oxide Composites and Cholesterol Oxidase for Ultrasensitive Cholesterol Biosensing. *Sens. Actuators B Chem.* **2019**, *298*, 126856. [[CrossRef](#)]
148. Oytun, F.; Basarir, F. Spin-Assisted Layer-by-Layer Assembled Oppositely Charged Reduced Graphene Oxide Films. *Mater. Lett.* **2019**, *257*, 126756. [[CrossRef](#)]
149. Miyazaki, C.M.; Adriano, A.M.; Rubira, R.J.G.; Constantino, C.J.L.; Ferreira, M. Combining Electrochemically Reduced Graphene Oxide and Layer-by-Layer Films of Magnetite Nanoparticles for Carbofuran Detection. *J. Environ. Chem. Eng.* **2020**, *8*, 104294. [[CrossRef](#)]
150. Oliveira, D.A.; Lutkenhaus, J.L.; Siqueira, J.R. Building up Nanostructured Layer-by-Layer Films Combining Reduced Graphene Oxide-Manganese Dioxide Nanocomposite in Supercapacitor Electrodes. *Thin Solid Films* **2021**, *718*, 138483. [[CrossRef](#)]
151. Xu, X.; Huang, D.; Cao, K.; Wang, M.; Zakeeruddin, S.M.; Grätzel, M. Electrochemically Reduced Graphene Oxide Multilayer Films as Efficient Counter Electrode for Dye-Sensitized Solar Cells. *Sci. Rep.* **2013**, *3*, 1489. [[CrossRef](#)]
152. Al-Hamry, A.; Lu, T.; Bai, J.; Adiraju, A.; Ega, T.K.; Paterno, L.G.; Pašti, I.A.; Kanoun, O. Versatile Sensing Capabilities of Layer-by-Layer Deposited Polyaniline-Reduced Graphene Oxide Composite-Based Sensors. *Sens. Actuators B Chem.* **2023**, *390*, 133988. [[CrossRef](#)]
153. Al-Hamry, A.; Lu, T.; Bai, J.; Adiraju, A.; Ega, T.K.; Pašti, I.A.; Kanoun, O. Layer-by-Layer Deposited Multi-Modal PDAC/RGO Composite-Based Sensors. *Foods* **2023**, *12*, 268. [[CrossRef](#)] [[PubMed](#)]
154. Kruk, T.; Socha, R.P.; Szyk-Warszyńska, L.; Warszyński, P. Flexible and Ultrathin Polyelectrolyte Conductive Coatings Formed with Reduced Graphene Oxide as a Base for Advanced New Materials. *Appl. Surf. Sci.* **2019**, *484*, 501–510. [[CrossRef](#)]
155. Davia, F.G.; Johnner, N.P.; Calvo, E.J.; Williams, F.J. Growth and Electrochemical Stability of a Layer-by-Layer Thin Film Containing Tetrasulfonated Fe Phthalocyanine. *J. Electroanal. Chem.* **2020**, *877*, 114485. [[CrossRef](#)]
156. Ali, B.; McCormac, T.; Maccato, C.; Barreca, D.; Carraro, G. Multilayer Assemblies of a Cu-Phthalocyanine with Dawson Type Polyoxometalates (POMs) for the Electrocatalytic Reduction of Phosphate. *J. Electroanal. Chem.* **2020**, *858*, 113770. [[CrossRef](#)]
157. Maciel, C.C.; de SM Freitas, A.; Medrades, J.P.; Ferreira, M. Simultaneous Determination of Catechol and Paraquat Using a Flexible Electrode of PBAT and Graphite Modified with Gold Nanoparticles and Copper Phthalocyanine (g-PBAT/AuNP/CuTsPc) LbL Film. *J. Electrochem. Soc.* **2022**, *169*, 027505. [[CrossRef](#)]
158. de Lima, L.F.; Maciel, C.C.; Ferreira, A.L.; de Almeida, J.C.; Ferreira, M. Nickel (II) Phthalocyanine-Tetrasulfonic-Au Nanoparticles Nanocomposite Film for Tartrazine Electrochemical Sensing. *Mater. Lett.* **2020**, *262*, 127196. [[CrossRef](#)]
159. de Lima, L.F.; Pereira, E.A.; Ferreira, M. Electrochemical Sensor for Propylparaben Using Hybrid Layer-by-Layer Films Composed of Gold Nanoparticles, Poly(Ethylene Imine) and Nickel(II) Phthalocyanine Tetrasulfonate. *Sensors Actuators, B Chem.* **2020**, *310*, 127893. [[CrossRef](#)]
160. Ribeiro, C.D.L.; De Souza, J.R.; Pereira-Da-Silva, M.A.; Santos, V.O.; Paterno, L.G. Electrocatalytic Oxidation of Ethinyl Estradiol by an Iron Oxide Nanoparticle/Nickel Phthalocyanine Supramolecular Electrode. *J. Phys. Chem. C* **2020**, *124*, 19057–19069. [[CrossRef](#)]
161. Furini, L.N.; Fernandes, J.D.; Vieira, D.H.; Morato, L.F.d.C.; Alves, N.; Constantino, C.J.L. Combining Impedance Spectroscopy and Information Visualization Methods to Optimize the Detection of Carbendazim Using Layer-by-Layer Films. *Chemosensors* **2023**, *11*, 213. [[CrossRef](#)]
162. Belce, Y.; Cebeci, F. Investigation of PH and Concentration Influence on Layer-by-Layer Self-Assembly for Nickel(II)Phthalocyanine-tetrasulfonic Acid Tetrasodium Salt Coatings. In *Porphyrim Science By Women (In 3 Volumes)*; World Scientific Publishing Co.: Singapore, 2020; pp. 834–840, ISBN 9789811223556.
163. de Oliveira, M.S.; Farias, E.A.d.O.; de Sousa, A.M.S.; Dionísio, N.A.; Teixeira, P.R.S.; Teixeira, A.S.d.N.M.; da Silva, D.A.; Eiras, C. Composite Films Based on Copper Nanoparticles and Nickel Phthalocyanine as Electrochemical Sensors for Serotonin Detection. *Surf. Interfaces* **2021**, *25*, 101245. [[CrossRef](#)]

164. Coelho, M.K.L.; da Silva, D.N.; Pereira, A.C. Development of Electrochemical Sensor Based on Carbonaceous and Metal Phthalocyanines Materials for Determination of Ethinyl Estradiol. *Chemosensors* **2019**, *7*, 32. [[CrossRef](#)]
165. Rangel, D.P.B.; Miyazaki, C.M.; Mascagni, D.B.T.; Ferreira, M. Layer-by-Layer Films of Gold Nanoparticles and Carbon Nanotubes for Improved Amperometric Detection of Cholesterol. *J. Nanosci. Nanotechnol.* **2019**, *19*, 5483–5488. [[CrossRef](#)]
166. Basova, T.V.; Ray, A.K. Review—Hybrid Materials Based on Phthalocyanines and Metal Nanoparticles for Chemiresistive and Electrochemical Sensors: A Mini-Review. *ECS J. Solid State Sci. Technol.* **2020**, *9*, 061001. [[CrossRef](#)]
167. Winiarski, J.P.; de Melo, D.J.; Santana, E.R.; Santos, C.S.; de Jesus, C.G.; Fujiwara, S.T.; Wohnrath, K.; Pessôa, C.A. Layer-By-Layer Films of Silsesquioxane and Nickel(II) Tetrasulphophthalocyanine as Glucose Oxidase Platform Immobilization: Amperometric Determination of Glucose in Kombucha Beverages. *Chemosensors* **2023**, *11*, 346. [[CrossRef](#)]
168. Salvo-Comino, C.; González-Gil, A.; Rodríguez-Valentin, J.; Garcia-Hernandez, C.; Martin-Pedrosa, F.; Garcia-Cabezon, C.; Rodríguez-Mendez, M.L. Biosensors Platform Based on Chitosan/AuNPs/Phthalocyanine Composite Films for the Electrochemical Detection of Catechol. the Role of the Surface Structure. *Sensors* **2020**, *20*, 2152. [[CrossRef](#)]
169. Fritea, L.; Banica, F.; Costea, T.O.; Moldovan, L.; Dobjanschi, L.; Muresan, M.; Cavalu, S. Metal Nanoparticles and Carbon-Based Nanomaterials for Improved Performances of Electrochemical (Bio)Sensors with Biomedical Applications. *Materials* **2021**, *14*, 6319. [[CrossRef](#)]
170. Pang, X.; Li, F.; Huang, S.; Yang, Z.; Mo, Q.; Huang, L.; Xu, W.; Chen, L.; Li, X. Electrostatically Mediated Layer-by-Layer Assembly of Nitrogen-Doped Graphene/PDDA/Gold Nanoparticle Composites for Electrochemical Detection of Uric Acid. *Anal. Bioanal. Chem.* **2020**, *412*, 669–680. [[CrossRef](#)]
171. de Almeida, J.C.; de Barros, A.; Odone Mazali, I.; Ferreira, M. Influence of Gold Nanostructures Incorporated into Sodium Montmorillonite Clay Based on LbL Films for Detection of Metal Traces Ions. *Appl. Surf. Sci.* **2020**, *507*, 144972. [[CrossRef](#)]
172. Wu, H.; Chen, Z.; Guo, L.; Wang, Y.; Du, S.; Wu, Y.; Ren, Z. Direct Coupling of Phthalocyanine Cobalt(II) and Graphene via Self-Driven Layer-by-Layer Assembly for Efficient Electrochemical Detection of Catechol. *J. Electrochem. Soc.* **2020**, *167*, 027533. [[CrossRef](#)]
173. Teixeira, P.R.; Machado, T.R.; Machado, F.; Sodré, F.F.; Silva, J.G.; Neto, B.A.D.; Paterno, L.G. Au Nanoparticle-Poly(Ionic Liquid) Nanocomposite Electrode for the Voltammetric Detection of Triclosan in Lake Water and Toothpaste Samples. *Microchem. J.* **2020**, *152*, 104421. [[CrossRef](#)]
174. Teeparuksapun, K.; Hedström, M.; Mattiasson, B. A Sensitive Capacitive Biosensor for Protein a Detection Using Human IgG Immobilized on an Electrode Using Layer-by-Layer Applied Gold Nanoparticles. *Sensors* **2022**, *22*, 99. [[CrossRef](#)]
175. Camilo, D.E.; Miyazaki, C.M.; Shimizu, F.M.; Ferreira, M. Improving Direct Immunoassay Response by Layer-by-Layer Films of Gold Nanoparticles–Antibody Conjugate towards Label-Free Detection. *Mater. Sci. Eng. C* **2019**, *102*, 315–323. [[CrossRef](#)] [[PubMed](#)]
176. Barsan, M.M.; Brett, C.M.A. Recent Advances in Layer-by-Layer Strategies for Biosensors Incorporating Metal Nanoparticles. *TrAC-Trends Anal. Chem.* **2016**, *79*, 286–296. [[CrossRef](#)]
177. Medrades, J.d.P.; Maciel, C.C.; Moraes, A.d.S.; Leite, F.d.L.; Ferreira, M. Flavin Adenine Dinucleotide Functionalized Gold Nanoparticles for the Electrochemical Detection of Dopamine. *Sens. Actuators Rep.* **2022**, *4*, 100085. [[CrossRef](#)]
178. Salvo-Comino, C.; Garcia-Hernandez, C.; Garcia-Cabezon, C.; Rodríguez-Mendez, M.L. Promoting Laccase Sensing Activity for Catechol Detection Using LBL Assemblies of Chitosan/Ionic Liquid/Phthalocyanine as Immobilization Surfaces. *Bioelectrochemistry* **2020**, *132*, 107407. [[CrossRef](#)]
179. Martínez-Hernández, M.E.; Goicoechea, J.; Rivero, P.J.; Arregui, F.J. In-Situ Synthesis of Gold Nanoparticles in Layer-by-Layer Polymeric Coatings for the Fabrication of Optical Fiber Sensors. *Polymers* **2022**, *14*, 776. [[CrossRef](#)]
180. Almeida, L.A.; Rodrigues, B.V.M.; Balogh, D.T.; Sanfelice, R.C.; Mercante, L.A.; Frade-Barros, A.F.; Pavinatto, A. Chitosan/Gold Nanoparticles Nanocomposite Film for Bisphenol A Electrochemical Sensing. *Electrochem* **2022**, *3*, 239–247. [[CrossRef](#)]
181. Goicoechea, J.; Rivero, P.J.; Sada, S.; Arregui, F.J. Self-Referenced Optical Fiber Sensor for Hydrogen Peroxide Detection Based on LSPR of Metallic Nanoparticles in Layer-by-Layer Films. *Sensors* **2019**, *19*, 3872. [[CrossRef](#)] [[PubMed](#)]
182. Lin, M.; Lu, M.; Liang, Y.; Yu, L.; Peng, W. Polyelectrolyte-Enhanced Localized Surface Plasmon Resonance Optical Fiber Sensors: Properties Interrogation and Bioapplication. *ACS Appl. Nano Mater.* **2022**, *5*, 6171–6180. [[CrossRef](#)]
183. Chia, K.K.; Cohen, R.E.; Rubner, M.F. Amine-Rich Polyelectrolyte Multilayer Nanoreactors for in Situ Gold Nanoparticle Synthesis. *Chem. Mater.* **2008**, *20*, 6756–6763. [[CrossRef](#)]
184. Guo, Y.; Yang, L.; Wang, D.; Liu, S.; Zhang, S. Preparation and Nanotribological Properties of Polyelectrolyte Multilayers with in Situ Au Nanoparticles. *Prog. Org. Coatings* **2015**, *88*, 164–171. [[CrossRef](#)]
185. Guo, D.; Chen, X.; Cai, K.; Deng, P.; Zong, R. Analyzing the Molecular Orientation of Ultrathin Organic Films by Polarized Transmission and Grazing Incidence Reflection Absorption IR Spectroscopy. *Mater. Focus* **2013**, *2*, 231–238. [[CrossRef](#)]
186. Rivero, P.J.; Goicoechea, J.; Arregui, F.J. Layer-by-Layer Nano-Assembly: A Powerful Tool for Optical Fiber Sensing Applications. *Sensors* **2019**, *19*, 683. [[CrossRef](#)]
187. Zhang, S.; Xu, Z.; Guo, J.; Wang, H.; Ma, Y.; Kong, X.; Fan, H.; Yu, Q. Layer-by-Layer Assembly of Polystyrene/Ag for a Highly Reproducible Sers Substrate and Its Use for the Detection of Food Contaminants. *Polymers* **2021**, *13*, 3270. [[CrossRef](#)] [[PubMed](#)]
188. Kasztelan, M.; Słoniewska, A.; Gorzkowski, M.; Lewera, A.; Pałys, B.; Zoladek, S. Ammonia Modified Graphene Oxide–Gold Nanoparticles Composite as a Substrate for Surface Enhanced Raman Spectroscopy. *Appl. Surf. Sci.* **2021**, *554*, 149060. [[CrossRef](#)]

189. Costa, Í.A.; Maciel, A.P.; Sales, M.J.A.; Moreira, S.G.C.; Paterno, L.G. The Role Played by Graphene Oxide in the Photodeposition and Surface-Enhanced Raman Scattering Activity of Plasmonic Ag Nanoparticle Substrates. *Phys. Status Solidi Appl. Mater. Sci.* **2020**, *217*, 1900965. [[CrossRef](#)]
190. Karn-Orachai, K. Gap-Dependent Surface-Enhanced Raman Scattering (SERS) Enhancement Model of SERS Substrate-Probe Combination Using a Polyelectrolyte Nanodroplet as a Distance Controller. *Langmuir* **2021**, *37*, 10776–10785. [[CrossRef](#)]
191. Mariani, S.; Pagni, A.; La Mattina, A.A.; Debrassi, A.; Dähne, L.; Barillaro, G. Decoration of Porous Silicon with Gold Nanoparticles via Layer-by-Layer Nanoassembly for Interferometric and Hybrid Photonic/Plasmonic (Bio)Sensing. *ACS Appl. Mater. Interfaces* **2019**, *11*, 43731–43740. [[CrossRef](#)] [[PubMed](#)]
192. Ariga, K.; Yamauchi, Y.; Rydzek, G.; Ji, Q.; Yonamine, Y.; Kevin, C.W.; Hill, J.P. Layer-by-Layer Nanoarchitectonics: Invention, Innovation, and Evolution. *Chem. Lett.* **2014**, *43*, 36–68. [[CrossRef](#)]
193. Guan, H.; Gong, D.; Song, Y.; Han, B.; Zhang, N. Biosensor Composed of Integrated Glucose Oxidase with Liposome Microreactors/Chitosan Nanocomposite for Amperometric Glucose Sensing. *Colloids Surfaces A Physicochem. Eng. Asp.* **2019**, *574*, 260–267. [[CrossRef](#)]
194. Chen, J.; Zhao, G.C.; Wei, Y.; Feng, D. A Signal-on Photoelectrochemical Biosensor for Detecting Cancer Marker Type IV Collagenase by Coupling Enzyme Cleavage with Exciton Energy Transfer Biosensing. *Anal. Methods* **2019**, *11*, 5880–5885. [[CrossRef](#)]
195. Si, Y.; Park, J.W.; Jung, S.; Hwang, G.S.; Park, Y.E.; Lee, J.E.; Lee, H.J. Voltammetric Layer-by-Layer Biosensor Featuring Purine Nucleoside Phosphorylase and Chitosan for Inosine in Human Serum Solutions. *Sens. Actuators B Chem.* **2019**, *298*, 126840. [[CrossRef](#)]
196. Salem, S.R.; Sullivan, J.L.; Topham, P.D.; Tighe, B.J. Supramolecular Host–Guest Carrier Based on Maltose-Modified Hyperbranched Polymer and Polyelectrolyte Multilayers: Toward Stable and Reusable Glucose Biosensor. *Polym. Bull.* **2020**, *77*, 3143–3170. [[CrossRef](#)]
197. Yokomichi, A.L.Y.; Rodrigues, V.d.C.; Moroz, A.; Bertanha, M.; Ribeiro, S.J.L.; Deffune, E.; Moraes, M.L. Detection of Factor VIII and D-Dimer Biomarkers for Venous Thromboembolism Diagnosis Using Electrochemistry Immunosensor. *Talanta* **2020**, *219*, 121241. [[CrossRef](#)] [[PubMed](#)]
198. Soares, A.C.; Soares, J.C.; Rodrigues, V.C.; Follmann, H.D.M.; Arantes, L.M.R.B.; Carvalho, A.C.; Melendez, M.E.; Fregnani, J.H.T.G.; Reis, R.M.; Carvalho, A.L.; et al. Microfluidic-Based Genosensor to Detect Human Papillomavirus (HPV16) for Head and Neck Cancer. *ACS Appl. Mater. Interfaces* **2018**, *10*, 36757–36763. [[CrossRef](#)]
199. Wu, M.; Liu, S.; Qi, F.; Qiu, R.; Feng, J.; Ren, X.; Rong, S.; Ma, H.; Chang, D.; Pan, H. A Label-Free Electrochemical Immunosensor for CA125 Detection Based on CMK-3(Au/Fc@MgAl-LDH)_n Multilayer Nanocomposites Modification. *Talanta* **2022**, *241*, 123254. [[CrossRef](#)]
200. Ibáñez-Redín, G.; Materon, E.M.; Furuta, R.H.M.; Wilson, D.; do Nascimento, G.F.; Melendez, M.E.; Carvalho, A.L.; Reis, R.M.; Oliveira, O.N.; Gonçalves, D. Screen-Printed Electrodes Modified with Carbon Black and Polyelectrolyte Films for Determination of Cancer Marker Carbohydrate Antigen 19-9. *Microchim. Acta* **2020**, *187*, 417. [[CrossRef](#)]
201. Soares, J.C.; Soares, A.C.; Popolin-Neto, M.; Paulovich, F.V.; Oliveira, O.N.; Mattoso, L.H.C. Detection of Staphylococcus Aureus in Milk Samples Using Impedance Spectroscopy and Data Processing with Information Visualization Techniques and Multidimensional Calibration Space. *Sensors and Actuators Reports* **2022**, *4*, 100083. [[CrossRef](#)]
202. Bondancia, T.J.; Soares, A.C.; Popolin-Neto, M.; Gomes, N.O.; Raymundo-Pereira, P.A.; Barud, H.S.; Machado, S.A.S.; Ribeiro, S.J.L.; Melendez, M.E.; Carvalho, A.L.; et al. Low-Cost Bacterial Nanocellulose-Based Interdigitated Biosensor to Detect the P53 Cancer Biomarker. *Biomater. Adv.* **2022**, *134*, 112676. [[CrossRef](#)] [[PubMed](#)]
203. Welden, M.; Poghosian, A.; Vahidpour, F.; Wendlandt, T.; Keusgen, M.; Wege, C.; Schöning, M.J. Capacitive Field-Effect Biosensor Modified with a Stacked Bilayer of Weak Polyelectrolyte and Plant Virus Particles as Enzyme Nanocarriers. *Bioelectrochemistry* **2023**, *151*, 108397. [[CrossRef](#)] [[PubMed](#)]
204. Bakshi, P.S.; Selvakumar, D.; Kadirvelu, K.; Kumar, N.S. Chitosan as an Environment Friendly Biomaterial—A Review on Recent Modifications and Applications. *Int. J. Biol. Macromol.* **2020**, *150*, 1072–1083. [[CrossRef](#)] [[PubMed](#)]
205. Soares, A.C.; Soares, J.C.; Shimizu, F.M.; Melendez, M.E.; Carvalho, A.L.; Oliveira, O.N. Controlled Film Architectures to Detect a Biomarker for Pancreatic Cancer Using Impedance Spectroscopy. *ACS Appl. Mater. Interfaces* **2015**, *7*, 25930–25937. [[CrossRef](#)] [[PubMed](#)]
206. Zhang, Y.; Zhang, Z.; Wang, Z.; Pan, H.; Lin, Y.; Chang, D. Sensitive Detection of Prostate-Specific Antigen Based on Dual Signal Amplification of Fc@MgAl-LDH and NH₂-MIL-101(Fe). *Biosens. Bioelectron.* **2021**, *190*, 113437. [[CrossRef](#)] [[PubMed](#)]
207. Mollarasouli, F.; Kurbanoglu, S.; Ozkan, S.A. The Role of Electrochemical Immunosensors in Clinical Analysis. *Biosensors* **2019**, *9*, 86. [[CrossRef](#)]
208. Paunovic, M.; Schlesinger, M. *Fundamentals of Electrochemical Deposition: Second Edition*; Wiley: Hoboken, NJ, USA, 2005; ISBN 0471712213.
209. Besra, L.; Liu, M. A Review on Fundamentals and Applications of Electrophoretic Deposition (EPD). *Prog. Mater. Sci.* **2007**, *52*, 1–61. [[CrossRef](#)]
210. Cai, S.; Yang, H.; Chen, C.; Xu, J.; Zhao, P.; Liu, X.; Li, H.; Chen, L. Self-Assembled Deposition of Polyaniline/Cobalt Porphyrin Based on Flexible PET to Improve Sensing of Room-Temperature NH₃ Sensor. *J. Alloys Compd.* **2023**, *934*, 167566. [[CrossRef](#)]

211. Bia, F.; Gualandi, I.; Griebel, J.; Rasmussen, L.; Hallak, B.; Tonelli, D.; Kersting, B. Heterobimetallic Conducting Polymers Based on Salophen Complexes via Electrosynthesis. *J. Mater. Chem. C* **2023**, *11*, 2957–2969. [CrossRef]
212. Kuzmin, S.M.; Chulovskaya, S.A.; Parfenyuk, V.I. Scan Rate Effect on Superoxide-Assisted Electrochemical Deposition of 2H-5,10,15,20-Tetrakis(3-Aminophenyl)Porphyrin Films. *Electrochim. Acta* **2022**, *425*, 140742. [CrossRef]
213. Namsheer, K.; Rout, C.S. Conducting Polymers: A Comprehensive Review on Recent Advances in Synthesis, Properties and Applications. *RSC Adv.* **2021**, *11*, 5659–5697. [CrossRef]
214. Raza, S.; Li, X.; Soyekwo, F.; Liao, D.; Xiang, Y.; Liu, C. A Comprehensive Overview of Common Conducting Polymer-Based Nanocomposites; Recent Advances in Design and Applications. *Eur. Polym. J.* **2021**, *160*, 110773. [CrossRef]
215. Joice, E.K.; Rison, S.; Akshaya, K.B.; Varghese, A. Platinum Decorated Polythiophene Modified Stainless Steel for Electrocatalytic Oxidation of Benzyl Alcohol. *J. Appl. Electrochem.* **2019**, *49*, 937–947. [CrossRef]
216. Ahumada, G.; Hamon, P.; Roisnel, T.; Dorcet, V.; Fuentealba, M.; Hernández, L.A.; Carrillo, D.; Hamon, J.-R.; Manzur, C. Spectroscopy, Molecular Structure, and Electropolymerization of Ni(II) and Cu(II) Complexes Containing a Thiophene-Appending Fluorinated Schiff Base Ligand. *Dalt. Trans.* **2023**, *52*, 4224–4236. [CrossRef] [PubMed]
217. Oberhaus, F.V. Carbonyl Compounds and Inorganic Brønsted Acids as Catalysts for Electropolymerization of Conductive Polymers. *Electrochim. Acta* **2023**, *449*, 142237. [CrossRef]
218. Fang, D.; Xu, T.; Fang, L.; Chen, H.; Huang, Y.; Zhang, H.; Miao, Z.; Mao, C.; Chi, B.; Xu, H. A Blood Compatible, High-Efficient Sensor for Detection of Cr(VI) in Whole Blood. *Sens. Actuators B Chem.* **2021**, *329*, 129219. [CrossRef]
219. Keteklahijani, Y.Z.; Sharif, F.; Roberts, E.P.L.; Sundararaj, U. Enhanced Sensitivity of Dopamine Biosensors: An Electrochemical Approach Based on Nanocomposite Electrodes Comprising Polyaniline, Nitrogen-Doped Graphene, and DNA-Functionalized Carbon Nanotubes. *J. Electrochem. Soc.* **2019**, *166*, B1415–B1425. [CrossRef]
220. Tavares, A.P.M.; Truta, L.A.A.N.A.; Moreira, F.T.C.; Carneiro, L.P.T.; Sales, M.G.F. Self-Powered and Self-Signalled Autonomous Electrochemical Biosensor Applied to Cancinoembryonic Antigen Determination. *Biosens. Bioelectron.* **2019**, *140*, 111320. [CrossRef]
221. Wang, R.; Li, J.; Gao, L.; Yu, J. One-Step Electropolymerized Thieno[3,2-b]Thiophene-Based Bifunctional Electrode with Controlled Color Conversion for Electrochromic Energy Storage Application. *Chem. Eng. J.* **2022**, *445*, 136731. [CrossRef]
222. Pineda, E.G.; Azpeitia, L.A.; Presa, M.J.R.; Bolzán, A.E.; Gervasi, C.A. Benchmarking Electrodes Modified with Bi-Doped Polypyrrole for Sensing Applications. *Electrochim. Acta* **2023**, *444*, 142011. [CrossRef]
223. Tkach, V.V.; de Paiva Martins, J.I.F.; Ivanushko, Y.G.; Yagodynets, P.I. Dye Electropolymerization for Electrochemical Analysis. A Brief Review. *Biointerface Res. Appl. Chem.* **2022**, *12*, 4028–4047. [CrossRef]
224. Kulikova, T.; Shiabiev, I.; Padnya, P.; Rogov, A.; Evtugyn, G.; Stoikov, I.; Porfireva, A. Impedimetric DNA Sensor Based on Electropolymerized N-Phenylaminophenothiazine and Thiacalix[4]Arene Tetraacids for Doxorubicin Determination. *Biosensors* **2023**, *13*, 513. [CrossRef] [PubMed]
225. Dalkiran, B.; Brett, C.M.A. Polyphenazine and Polytriphenylmethane Redox Polymer/Nanomaterial-Based Electrochemical Sensors and Biosensors: A Review. *Microchim. Acta* **2021**, *188*, 178. [CrossRef] [PubMed]
226. da Silva, W.; Queiroz, A.C.; Brett, C.M.A. Poly(Methylene Green)–Ethaline Deep Eutectic Solvent/Fe₂O₃ Nanoparticle Modified Electrode Electrochemical Sensor for the Antibiotic Dapsone. *Sens. Actuators B Chem.* **2020**, *325*, 128747. [CrossRef]
227. Tsuruoka, N.; Soto, S.S.; Tahar, A.B.; Zebda, A.; Tsujimura, S. Mediated Electrochemical Oxidation of Glucose via Poly(Methylene Green) Grafted on the Carbon Surface Catalyzed by Flavin Adenine Dinucleotide-Dependent Glucose Dehydrogenase. *Colloids Surf. B Biointerfaces* **2020**, *192*, 111065. [CrossRef] [PubMed]
228. Ghoorchian, A.; Madrakian, T.; Afkhami, A.; Bagheri, H. Spectroelectrochemical and Electrochromic Behavior of Poly(Methylene Blue) and Poly(Thionine)-Modified Multi-Walled Carbon Nanotubes. *J. Solid State Electrochem.* **2021**, *25*, 1217–1229. [CrossRef]
229. Yin, C.; Zhuang, Q.; Xiao, Q.; Wang, Y.; Xie, J. Electropolymerization of Poly(Methylene Blue) on Flower-like Nickel-Based MOFs Used for Ratiometric Electrochemical Sensing of Total Polyphenolic Content in Chrysanthemum Tea. *Anal. Methods* **2021**, *13*, 1154–1163. [CrossRef]
230. Mokhtari, Z.; Khajehsharifi, H.; Hashemnia, S.; Solati, Z.; Azimpanah, R.; Shahrokhian, S. Evaluation of Molecular Imprinted Polymerized Methylene Blue/Aptamer as a Novel Hybrid Receptor for Cardiac Troponin I (CTnI) Detection at Glassy Carbon Electrodes Modified with New Biosynthesized ZnONPs. *Sens. Actuators B Chem.* **2020**, *320*, 128316. [CrossRef]
231. Liang, X.; Zhou, Y.; Brett, C.M.A. Electropolymerisation of Brilliant Cresyl Blue and Neutral Red on Carbon-Nanotube Modified Electrodes in Binary and Ternary Deep Eutectic Solvents. *J. Electroanal. Chem.* **2022**, *919*, 116557. [CrossRef]
232. Liang, X.; Zhou, Y.; Almeida, J.M.S.; Brett, C.M.A. A Novel Electrochemical Acetaminophen Sensor Based on Multiwalled Carbon Nanotube and Poly(Neutral Red) Modified Electrodes with Electropolymerization in Ternary Deep Eutectic Solvents. *J. Electroanal. Chem.* **2023**, *936*, 117366. [CrossRef]
233. Ağin, F.; Öztürk, G.; Kul, D. Voltammetric Analysis of Ephedrine in Pharmaceutical Dosage Forms and Urine Using Poly(Nile Blue A) Modified Glassy Carbon Electrode. *Comb. Chem. High Throughput Screen.* **2020**, *24*, 366–375. [CrossRef] [PubMed]
234. Olean-Oliveira, A.; Oliveira Brito, G.A.; Cardoso, C.X.; Teixeira, M.F.S. Role of Anion Size in the Electrochemical Performance of a Poly(Thionine) Redox Conductive Polymer Using Spectrochemical Impedance Spectroscopy. *Polymer* **2022**, *258*, 125291. [CrossRef]
235. Gribkova, O.L.; Kabanova, V.A.; Nekrasov, A.A. Electrodeposition of Thin Films of Polypyrrole-Polyelectrolyte Complexes and Their Ammonia-Sensing Properties. *J. Solid State Electrochem.* **2020**, *24*, 3091–3103. [CrossRef]

236. Patois, T.; Sanchez, J.-B.; Berger, F.; Rauch, J.-Y.; Fievet, P.; Lakard, B. Ammonia Gas Sensors Based on Polypyrrole Films: Influence of Electrodeposition Parameters. *Sens. Actuators B Chem.* **2012**, *171–172*, 431–439. [[CrossRef](#)]
237. Xie, X.; Tang, J.; Xing, Y.; Wang, Z.; Ding, T.; Zhang, J.; Cai, K. Intervention of Polydopamine Assembly and Adhesion on Nanoscale Interfaces: State-of-the-Art Designs and Biomedical Applications. *Adv. Healthc. Mater.* **2021**, *10*, 2002138. [[CrossRef](#)] [[PubMed](#)]
238. Szewczyk, J.; Aguilar-Ferrer, D.; Coy, E. Polydopamine Films: Electrochemical Growth and Sensing Applications. *Eur. Polym. J.* **2022**, *174*, 111346. [[CrossRef](#)]
239. Coy, E.; Iatsunskiy, I.; Colmenares, J.C.; Kim, Y.; Mrówczyński, R. Polydopamine Films with 2D-like Layered Structure and High Mechanical Resilience. *ACS Appl. Mater. Interfaces* **2021**, *13*, 23113–23120. [[CrossRef](#)]
240. Szewczyk, J.; Pochylski, M.; Szutkowski, K.; Kempański, M.; Mrówczyński, R.; Iatsunskiy, I.; Gapiński, J.; Coy, E. In-Situ Thickness Control of Centimetre-Scale 2D-Like Polydopamine Films with Large Scalability. *Mater. Today Chem.* **2022**, *24*, 100935. [[CrossRef](#)]
241. Almeida, L.C.; Correia, R.D.; Squillaci, G.; Morana, A.; La Cara, F.; Correia, J.P.; Viana, A.S. Electrochemical Deposition of Bio-Inspired Laccase-Polydopamine Films for Phenolic Sensors. *Electrochim. Acta* **2019**, *319*, 462–471. [[CrossRef](#)]
242. Healy, B.; Yu, T.; da Silva Alves, D.C.; Okeke, C.; Breslin, C.B. Cyclodextrins as Supramolecular Recognition Systems: Applications in the Fabrication of Electrochemical Sensors. *Materials* **2021**, *14*, 1668. [[CrossRef](#)] [[PubMed](#)]
243. Pereira, A.C.; Oliveira, A.E.F.; Bettio, G.B. β -Cyclodextrin Electropolymerization: Mechanism, Electrochemical Behavior, and Optimization. *Chem. Pap.* **2019**, *73*, 1795–1804. [[CrossRef](#)]
244. Chang, Z.; Zhu, B.; Liu, J.J.; Zhu, X.; Xu, M.; Travas-Sejdic, J. Electrochemical Aptasensor for 17β -Estradiol Using Disposable Laser Scribed Graphene Electrodes. *Biosens. Bioelectron.* **2021**, *185*, 113247. [[CrossRef](#)] [[PubMed](#)]
245. Chang, Y.H.; Woi, P.M.; Alias, Y. The Selective Electrochemical Detection of Dopamine in the Presence of Ascorbic Acid and Uric Acid Using Electro-Polymerised- β -Cyclodextrin Incorporated f-MWCNTs/Polyaniline Modified Glassy Carbon Electrode. *Microchem. J.* **2019**, *148*, 322–330. [[CrossRef](#)]
246. Harley, C.C.; Annibaldi, V.; Yu, T.; Breslin, C.B. The Selective Electrochemical Sensing of Dopamine at a Polypyrrole Film Doped with an Anionic β -cyclodextrin. *J. Electroanal. Chem.* **2019**, *855*, 113614. [[CrossRef](#)]
247. Annibaldi, V.; Breslin, C.B. Electrochemistry of Viologens at Polypyrrole Doped with Sulfonated β -Cyclodextrin. *J. Electroanal. Chem.* **2019**, *832*, 399–407. [[CrossRef](#)]
248. Ghanbari, M.H.; Shahdost-fard, F.; Khoshroo, A.; Rahimi-Nasrabadi, M.; Ganjali, M.R.; Wysokowski, M.; Rębiś, T.; Żółtowska-Aksamitowska, S.; Jesionowski, T.; Rahimi, P.; et al. A Nanocomposite Consisting of Reduced Graphene Oxide and Electropolymerized β -Cyclodextrin for Voltammetric Sensing of Levofloxacin. *Microchim. Acta* **2019**, *186*, 438. [[CrossRef](#)] [[PubMed](#)]
249. Shrivastava, S.; Bairagi, P.K.; Verma, N. Spermine Biomarker of Cancerous Cells Voltammetrically Detected on a Poly(β -Cyclodextrin)-Electropolymerized Carbon Film Dispersed with Cu-CNFs. *Sens. Actuators B Chem.* **2020**, *313*, 128055. [[CrossRef](#)]
250. Wang, R.; Wang, S.; Qin, C.; Nie, Q.; Luo, Y.; Qin, Q.-P.; Wang, R.; Liu, B.; Luo, D. An Electrochemical Sensor Based on Electropolymerization of β -Cyclodextrin on Glassy Carbon Electrode for the Determination of Fenitrothion. *Sensors* **2022**, *23*, 435. [[CrossRef](#)]
251. Ma, M.; Liang, J. Voltammetric Detection of 2-Aminoazotoluene Based on Electropolymerization of β -Cyclodextrin. *Chem. Pap.* **2023**, *77*, 2967–2976. [[CrossRef](#)]
252. Gonçalves, J.M.; Iglesias, B.A.; Martins, P.R.; Angnes, L. Recent Advances in Electroanalytical Drug Detection by Porphyrin/Phthalocyanine Macrocycles: Developments and Future Perspectives. *Analyst* **2021**, *146*, 365–381. [[CrossRef](#)] [[PubMed](#)]
253. Gottfried, J.M. Surface Chemistry of Porphyrins and Phthalocyanines. *Surf. Sci. Rep.* **2015**, *70*, 259–379. [[CrossRef](#)]
254. Rubio, R.; Suarez, M.B.; Pérez, M.E.; Heredia, D.A.; Morales, G.M.; Durantini, E.N.; Otero, L.; Gervaldó, M.; Durantini, J.E. Electropolymerized Porphyrin Films as Active Materials in Organic Supercapacitors. A Study of the Effect of Different Central Metals. *Electrochim. Acta* **2023**, *458*, 142552. [[CrossRef](#)]
255. Napierała, S.; Kubicki, M.; Patroniak, V.; Wałęsa-Chorab, M. Electropolymerization of $[2 \times 2]$ Grid-Type Cobalt(II) Complex with Thiophene Substituted Dihydrazone Ligand. *Electrochim. Acta* **2021**, *369*, 137656. [[CrossRef](#)]
256. Peng, R.; Offenhäusser, A.; Ermolenko, Y.; Mourzina, Y. Biomimetic Sensor Based on Mn(III) Meso-Tetra(N-Methyl-4-Pyridyl) Porphyrin for Non-Enzymatic Electrocatalytic Determination of Hydrogen Peroxide and as an Electrochemical Transducer in Oxidase Biosensor for Analysis of Biological Media. *Sens. Actuators B Chem.* **2020**, *321*, 128437. [[CrossRef](#)]
257. Jiang, R.; Pang, Y.-H.; Yang, Q.-Y.; Wan, C.-Q.; Shen, X.-F. Copper Porphyrin Metal-Organic Framework Modified Carbon Paper for Electrochemical Sensing of Glyphosate. *Sens. Actuators B Chem.* **2022**, *358*, 131492. [[CrossRef](#)]
258. Kuzmin, S.M.; Chulovskaya, S.A.; Parfenyuk, V.I. Effect of Substituent Structure on Formation and Properties of Poly-Hydroxyphenyl Porphyrin Films Obtained by Superoxide-Assisted Method. *Electrochim. Acta* **2020**, *342*, 136064. [[CrossRef](#)]
259. Pavel, I.-A.; Lasserre, A.; Simon, L.; Rossignol, J.; Lakard, S.; Stuerge, D.; Lakard, B. Microwave Gas Sensors Based on Electrodeposited Polypyrrole–Nickel Phthalocyanine Hybrid Films. *Sensors* **2023**, *23*, 5550. [[CrossRef](#)]
260. Martin, C.S.; Gouveia-Caridade, C.; Crespilho, F.N.; Constantino, C.J.L.; Brett, C.M.A. Iron Phthalocyanine Electrodeposited Films: Characterization and Influence on Dopamine Oxidation. *J. Phys. Chem. C* **2016**, *120*, 15698–15706. [[CrossRef](#)]
261. Martin, C.S.; Alessio, P.; Crespilho, F.N.; Brett, C.M.A.; Constantino, C.J.L. Influence of the Supramolecular Arrangement of Iron Phthalocyanine Thin Films on Catecholamine Oxidation. *J. Electroanal. Chem.* **2019**, *836*, 7–15. [[CrossRef](#)]

262. Luhana, C.; Mashazi, P. Simultaneous Detection of Dopamine and Paracetamol on Electroreduced Graphene Oxide–Cobalt Phthalocyanine Polymer Nanocomposite Electrode. *Electrocatalysis* **2023**, *14*, 406–417. [CrossRef]
263. Adeniyi, O.; Nwahara, N.; Mwanza, D.; Nyokong, T.; Mashazi, P. High-Performance Non-Enzymatic Glucose Sensing on Nanocomposite Electrocatalysts of Nickel Phthalocyanine Nanorods and Nitrogen Doped-Reduced Graphene Oxide Nanosheets. *Appl. Surf. Sci.* **2023**, *609*, 155234. [CrossRef]
264. Speranza, G. Carbon Nanomaterials: Synthesis, Functionalization and Sensing Applications. *Nanomaterials* **2021**, *11*, 967. [CrossRef] [PubMed]
265. Han, T.; Nag, A.; Chandra Mukhopadhyay, S.; Xu, Y. Carbon Nanotubes and Its Gas-Sensing Applications: A Review. *Sens. Actuators A Phys.* **2019**, *291*, 107–143. [CrossRef]
266. Norizan, M.N.; Moklis, M.H.; Ngah Demon, S.Z.; Halim, N.A.; Samsuri, A.; Mohamad, I.S.; Knight, V.F.; Abdullah, N. Carbon Nanotubes: Functionalisation and Their Application in Chemical Sensors. *RSC Adv.* **2020**, *10*, 43704–43732. [CrossRef] [PubMed]
267. Li, M.; Chen, T.; Gooding, J.J.; Liu, J. Review of Carbon and Graphene Quantum Dots for Sensing. *ACS Sensors* **2019**, *4*, 1732–1748. [CrossRef] [PubMed]
268. Mushiana, T.; Mabuba, N.; Idris, A.O.; Peleyeju, G.M.; Orimolade, B.O.; Nkosi, D.; Ajayi, R.F.; Arotiba, O.A. An Aptasensor for Arsenic on a Carbon-gold Bi-Nanoparticle Platform. *Sens. Bio-Sensing Res.* **2019**, *24*, 100280. [CrossRef]
269. Gally, P.; Eguílaz, M.; Rivas, G. Designing Electrochemical Interfaces Based on Nanohybrids of Avidin Functionalized-Carbon Nanotubes and Ruthenium Nanoparticles as Peroxidase-like Nanozyme with Supramolecular Recognition Properties for Site-Specific Anchoring of Biotinylated Residues. *Biosens. Bioelectron.* **2020**, *148*, 111764. [CrossRef]
270. Meskher, H.; Ragdi, T.; Thakur, A.K.; Ha, S.; Khelifaoui, I.; Sathyamurthy, R.; Sharshir, S.W.; Pandey, A.K.; Saidur, R.; Singh, P.; et al. A Review on CNTs-Based Electrochemical Sensors and Biosensors: Unique Properties and Potential Applications. *Crit. Rev. Anal. Chem.* **2023**, 1–24. [CrossRef]
271. Sen, S.; Sarkar, P. A Simple Electrochemical Approach to Fabricate Functionalized MWCNT-Nanogold Decorated PEDOT Nanohybrid for Simultaneous Quantification of Uric Acid, Xanthine and Hypoxanthine. *Anal. Chim. Acta* **2020**, *1114*, 15–28. [CrossRef]
272. Taylor, I.M.; Patel, N.A.; Freedman, N.C.; Castagnola, E.; Cui, X.T. Direct in Vivo Electrochemical Detection of Resting Dopamine Using Poly(3,4-Ethylenedioxythiophene)/Carbon Nanotube Functionalized Microelectrodes. *Anal. Chem.* **2019**, *91*, 12917–12927. [CrossRef] [PubMed]
273. Gao, J.; Yang, T.; Wang, X.; He, Q.; He, P.; Jia, L.; Du, L.; Deng, H.; Zhang, H.; Jia, B.; et al. Spherical Phosphomolybdic Acid Immobilized on Graphene Oxide Nanosheets as an Efficient Electrochemical Sensor for Detection of Diphenylamine. *Microchem. J.* **2020**, *158*, 105158. [CrossRef]
274. Zhao, P.; Huang, L.; Wang, H.; Wang, C.; Chen, J.; Yang, P.; Ni, M.; Chen, C.; Li, C.; Xie, Y.; et al. An Ultrasensitive High-Performance Baicalin Sensor Based on C3N4-SWCNTs/Reduced Graphene Oxide/Cyclodextrin Metal-Organic Framework Nanocomposite. *Sens. Actuators B Chem.* **2022**, *350*, 130853. [CrossRef] [PubMed]
275. Wang, X.; Mohammadzadehsaliani, S.; Vafaei, S.; Ahmadi, L.; Iqbal, A.; Alreda, B.A.; Talib Al-Naqeeb, B.Z.; Kheradjo, H. Synthesis and Electrochemical Study of Enzymatic Graphene Oxide-Based Nanocomposite as Stable Biosensor for Determination of Bevacizumab as a Medicine in Colorectal Cancer in Human Serum and Wastewater Fluids. *Chemosphere* **2023**, *336*, 139012. [CrossRef] [PubMed]
276. Bolat, G.; Yaman, Y.T.; Abacı, S.; Seyyar, S. Poly-Arginine/Graphene Oxide Functionalized Disposable Sensor for Monitoring Fenitrothion Pesticide Residues in Water and Cucumber Samples. *Mater. Today Chem.* **2023**, *30*, 101517. [CrossRef]
277. Kanagavalli, P.; Natchimuthu Karuppusamy, M.; Ganesan, V.S.; Saravanan, H.P.; Palanisamy, T.; Veerapandian, M. Electropolymerized Melamine on Electrochemically Reduced Graphene Oxide: Growth Mechanistics, Electrode Processing, and Amperometric Sensing of Acyclovir. *Langmuir* **2023**, *39*, 3512–3525. [CrossRef] [PubMed]
278. Hssi, A.A.; Atourki, L.; Labchir, N.; Abouabassi, K.; Ouafi, M.; Mouhib, H.; Ihlal, A.; Elfanaoui, A.; Benmokhtar, S.; Bouabid, K. Structural and Optical Properties of Electrodeposited Cu₂O Thin Films. *Mater. Today Proc.* **2020**, *22*, 89–92. [CrossRef]
279. Ravichandiran, C.; Sakthivelu, A.; Davidprabu, R.; Deva Arun Kumar, K.; Valanarasu, S.; Kathalingam, A.; Ganesh, V.; Shkir, M.; AlFaify, S. The Effect of Rare Earth Nd³⁺-doping on Physical Characteristics of Cu₂O Thin Films Derived by Electrodeposition Technique. *Thin Solid Films* **2019**, *683*, 82–89. [CrossRef]
280. Jose, S.; Das, S.; Vakamalla, T.R.; Sen, D. Electrochemical Glucose Sensing Using Molecularly Imprinted Polyaniline–Copper Oxide Coated Electrode. *Surf. Eng. Appl. Electrochem.* **2022**, *58*, 260–268. [CrossRef]
281. Gowda, J.I.; Hanabaratti, R.M.; Hipparagi, S.S. Development of Manganese Oxide Nanoparticles Based Chemical Sensor for Sensitive Determination of an Antiviral Drug Valaciclovir. *Results Chem.* **2023**, *5*, 100801. [CrossRef]
282. Amali, R.K.A.; Lim, H.N.; Ibrahim, I.; Zainal, Z.; Ahmad, S.A.A. A Copper-Based Metal–Organic Framework Decorated with Electrodeposited Fe₂O₃ Nanoparticles for Electrochemical Nitrite Sensing. *Microchim. Acta* **2022**, *189*, 356. [CrossRef]
283. Dumore, N.S.; Mukhopadhyay, M. Electroanalytical Performance of Non-Enzymatic Electrochemical Sensor Based on PtNPs-SeNPs-SnO₂NPs@BFTO Nanocomposites for the Detection of Hydrogen Peroxide. *Electrocatalysis* **2023**, *14*, 708–719. [CrossRef]
284. Xiao, H.; Cao, L.; Qin, H.; Wei, S.; Gu, M.; Zhao, F.; Chen, Z. Non-Enzymatic Lactic Acid Sensor Based on AuPtNPs Functionalized MoS₂ Nanosheet as Electrode Modified Materials. *J. Electroanal. Chem.* **2021**, *903*, 115806. [CrossRef]

285. Hannula, P.-M.; Pletincx, S.; Janas, D.; Yliniemi, K.; Hubin, A.; Lundström, M. Controlling the Deposition of Silver and Bimetallic Silver/Copper Particles onto a Carbon Nanotube Film by Electrodeposition-Redox Replacement. *Surf. Coatings Technol.* **2019**, *374*, 305–316. [CrossRef]
286. Tonelli, D.; Scavetta, E.; Gualandi, I. Electrochemical Deposition of Nanomaterials for Electrochemical Sensing. *Sensors* **2019**, *19*, 1186. [CrossRef]
287. Wadie, M.; Abdel-Moety, E.M.; Rezk, M.R.; Mahmoud, A.M.; Marzouk, H.M. Electro-Polymerized Poly-Methylidopa as a Novel Synthetic Mussel-Inspired Molecularly Imprinted Polymeric Sensor for Darifenacin: Computational and Experimental Study. *Appl. Mater. Today* **2022**, *29*, 101595. [CrossRef]
288. Atta, N.F.; Galal, A.; El-Said, D.M. Novel Design of a Layered Electrochemical Dopamine Sensor in Real Samples Based on Gold Nanoparticles/ β -Cyclodextrin/Nafion-Modified Gold Electrode. *ACS Omega* **2019**, *4*, 17947–17955. [CrossRef]
289. Gissawong, N.; Srijaranai, S.; Boonchiangma, S.; Uppachai, P.; Seehamart, K.; Jantrasee, S.; Moore, E.; Mukdasai, S. An Electrochemical Sensor for Voltammetric Detection of Ciprofloxacin Using a Glassy Carbon Electrode Modified with Activated Carbon, Gold Nanoparticles and Supramolecular Solvent. *Microchim. Acta* **2021**, *188*, 208. [CrossRef]
290. Paramasivam, S.; Veerapandian, M.; Kumar, S.S. Rational Design of Effective Solid-State Electrochemiluminescence Platform of Gold@Polyluminol Nanocomposite as an Ultrasensitive Immuno-Probe for Selective Detection of Prostate Specific Antigen. *Anal. Chim. Acta* **2022**, *1206*, 339736. [CrossRef]
291. Stoian, I.A.; Iacob, B.C.; Prates Ramalho, J.P.; Marian, I.O.; Chiş, V.; Bodoki, E.; Oprean, R. A Chiral Electrochemical System Based on L-Cysteine Modified Gold Nanoparticles for Propranolol Enantiodiscrimination: Electroanalysis and Computational Modelling. *Electrochim. Acta* **2019**, *326*, 134961. [CrossRef]
292. Liu, C.; Wei, X.; Wang, X.; Shi, J.; Chen, Z.; Zhang, H.; Zhang, W.; Zou, X. Ratiometric Electrochemical Analysis on a Flexibly-Fabricated Vibratory Electrode Module for Reliable and Selective Determination of Imidacloprid. *Sensors Actuators, B Chem.* **2021**, *329*, 129228. [CrossRef]
293. Wang, Y.; Deng, J.; Di, J.; Tu, Y. Electrodeposition of Large Size Gold Nanoparticles on Indium Tin Oxide Glass and Application as Refractive Index Sensor. *Electrochem. commun.* **2009**, *11*, 1034–1037. [CrossRef]
294. Ghanbari, M.H.; Mashhadizadeh, M.H.; Norouzi, Z.; Salehzadeh, H. Simultaneous Electrochemical Detection of Uric Acid and Xanthine Based on Electrodeposited B, N Co-Doped Reduced Graphene Oxide, Gold Nanoparticles and Electropolymerized Poly (L-Cysteine) Gradually Modified Electrode Platform. *Microchem. J.* **2022**, *175*, 107213. [CrossRef]
295. Karthikeyan, M.; Dhinesh Kumar, M.; Kaniraja, G.; Ananthappan, P.; Sivasamy Vasantha, V.; Karunakaran, C. Gold Nanoparticles Enhanced Molecularly Imprinted Poly(3-Aminophenylboronic Acid) Sensor for Myo-Inositol Detection. *Microchem. J.* **2023**, *189*, 108536. [CrossRef]
296. Ning, L.; Bai, Y.; Wang, Z.; Wen, W.; Wang, J. Label-Free Electrochemiluminescence Immunosensor Based on Conductive PANI to Synergistically Amplify Electrodeposited AuNPs Luminophore Signal for Ultrasensitive Detection of 3-Nitrotyrosine. *Microchem. J.* **2023**, *190*, 108619. [CrossRef]
297. Atici, T.; Bilgi Kamaç, M.; Yilmaz, M.; Yilmaz Kabaca, A. Zinc Oxide Nanorod/Polymethylene Blue (Deep Eutectic Solvent)/Gold Nanoparticles Modified Electrode for Electrochemical Determination of Serotonin (5-HT). *Electrochim. Acta* **2023**, *458*, 142484. [CrossRef]
298. Aydın, E.B.; Aydın, M.; Sezgintürk, M.K. A Label-Free Electrochemical Biosensor for Highly Sensitive Detection of GM2A Based on Gold Nanoparticles/Conducting Amino-Functionalized Thiophene Polymer Layer. *Sens. Actuators B Chem.* **2023**, *392*, 134025. [CrossRef]
299. Zhe, T.; Sun, X.; Wang, Q.; Liu, Y.; Li, R.; Li, F.; Wang, L. A Screen Printed Carbon Electrode Modified with a Lamellar Nanocomposite Containing Dendritic Silver Nanostructures, Reduced Graphene Oxide, and β -Cyclodextrin for Voltammetric Sensing of Nitrite. *Microchim. Acta* **2019**, *186*, 319. [CrossRef]
300. Zhang, H.; Xu, G.; Chen, Y.; Li, X.; Wang, S.; Jiang, F.; Zhan, P.; Lu, C.; Cao, X.; Ye, Y.; et al. Electrochemical Detection of OmpA Gene of *C. Sakazakii* Based on Glucose-Oxidase-Mimicking Nanotags of Gold-Nanoparticles-Doped Copper Metal-Organic Frameworks. *Sensors* **2023**, *23*, 4396. [CrossRef]
301. Rhys-Jones, T.N. Thermally Sprayed Coating Systems for Surface Protection and Clearance Control Applications in Aero Engines. *Surf. Coatings Technol.* **1990**, *43–44*, 402–415. [CrossRef]
302. Jena, G.; Philip, J. A Review on Recent Advances in Graphene Oxide-Based Composite Coatings for Anticorrosion Applications. *Prog. Org. Coatings* **2022**, *173*, 107208. [CrossRef]
303. Fotovvati, B.; Namdari, N.; Dehghanhadikolaei, A. On Coating Techniques for Surface Protection: A Review. *J. Manuf. Mater. Process.* **2019**, *3*, 28. [CrossRef]
304. Ma, S.; Sansoni, S.; Gatti, T.; Fino, P.; Liu, G.; Lamberti, F. Research Progress on Homogeneous Fabrication of Large-Area Perovskite Films by Spray Coating. *Crystals* **2023**, *13*, 216. [CrossRef]
305. Workie, A.B.; Ningsih, H.S.; Shih, S.J. An Comprehensive Review on the Spray Pyrolysis Technique: Historical Context, Operational Factors, Classifications, and Product Applications. *J. Anal. Appl. Pyrolysis* **2023**, *170*, 105915. [CrossRef]
306. Liao, T.Y.; Biesiekierski, A.; Berndt, C.C.; King, P.C.; Ivanova, E.P.; Thissen, H.; Kingshott, P. Multifunctional Cold Spray Coatings for Biological and Biomedical Applications: A Review. *Prog. Surf. Sci.* **2022**, *97*, 100654. [CrossRef]
307. Sriram, S.R.; Parne, S.R.; Pothukanuri, N.; Edla, D.R. Prospects of Spray Pyrolysis Technique for Gas Sensor Applications—A Comprehensive Review. *J. Anal. Appl. Pyrolysis* **2022**, *164*, 105527. [CrossRef]

308. Guild, C.; Biswas, S.; Meng, Y.; Jafari, T.; Gaffney, A.M.; Suib, S.L. Perspectives of Spray Pyrolysis for Facile Synthesis of Catalysts and Thin Films: An Introduction and Summary of Recent Directions. *Catal. Today* **2014**, *238*, 87–94. [[CrossRef](#)]
309. Sawant, J.P.; Deokate, R.J.; Pathan, H.M.; Kale, R.B. Spray Pyrolytic Deposition of CuInS₂ Thin Films: Properties and Applications. *Eng. Sci.* **2021**, *13*, 51–64. [[CrossRef](#)]
310. Kate, R.S.; Pathan, H.M.; Kalubarme, R.; Kale, B.B.; Deokate, R.J. Spray Pyrolysis: Approaches for Nanostructured Metal Oxide Films in Energy Storage Application. *J. Energy Storage* **2022**, *54*, 105387. [[CrossRef](#)]
311. Lampkin, C.M. Aerodynamics of Nozzles Used in Spray Pyrolysis. *Prog. Cryst. Growth Charact.* **1979**, *1*, 405–416. [[CrossRef](#)]
312. Kastrinaki, G.; Lorentzou, S.; Karagiannakis, G.; Rattenbury, M.; Woodhead, J.; Konstandopoulos, A.G. Parametric Synthesis Study of Iron Based Nanoparticles via Aerosol Spray Pyrolysis Route. *J. Aerosol Sci.* **2018**, *115*, 96–107. [[CrossRef](#)]
313. Abd-Alghafour, N.M.; Ahmed, N.M.; Hassan, Z. Fabrication and Characterization of V₂O₅ Nanorods Based Metal–Semiconductor–Metal Photodetector. *Sens. Actuators A Phys.* **2016**, *250*, 250–257. [[CrossRef](#)]
314. Shahbazi, M.; Taherkhani, A. Study of Optical and Structural Properties of GO and MnO₂-GO Hybrid Fabricated by Spray Pyrolysis Technique. *Opt. Mater.* **2022**, *123*, 111849. [[CrossRef](#)]
315. Vijayalakshmi, K.; Renitta, A.; Monamary, A. Substantial Effect of Pd Incorporation on the Room Temperature Hydrogen Sensing Performance of ZnO/ITO Nanowires Prepared by Spray Pyrolysis Method. *J. Mater. Sci. Mater. Electron.* **2018**, *29*, 21023–21032. [[CrossRef](#)]
316. Kundu, M.; Karunakaran, G.; Kolesnikov, E.; Sergeevna, V.E.; Kumari, S.; Gorshenkov, M.V.; Kuznetsov, D. Hollow NiCo₂O₄ Nano-Spheres Obtained by Ultrasonic Spray Pyrolysis Method with Superior Electrochemical Performance for Lithium-Ion Batteries and Supercapacitors. *J. Ind. Eng. Chem.* **2017**, *59*, 90–98. [[CrossRef](#)]
317. Kaya, E.E.; Kaya, O.; Alkan, G.; Gürmen, S.; Stopic, S.; Friedrich, B. New Proposal for Size and Size-Distribution Evaluation of Nanoparticles Synthesized via Ultrasonic Spray Pyrolysis Using Search Algorithm Based on Image-Processing Technique. *Materials* **2020**, *13*, 38. [[CrossRef](#)] [[PubMed](#)]
318. Abdulrahman, A.F.; Abd-Alghafour, N.M. Synthesis and Characterization of ZnO Nanoflowers by Using Simple Spray Pyrolysis Technique. *Solid. State. Electron.* **2022**, *189*, 108225. [[CrossRef](#)]
319. Yusuf, B.; Hashim, M.R.; Pakhuruddin, M.Z.; Halim, M.M. Effect of Solution Flow Rate on the Physical Properties of Spray Pyrolyzed MoO₃ Thin Films as Silicon-Based Heterojunction Device. *Superlattices Microstruct.* **2021**, *164*, 107111. [[CrossRef](#)]
320. Zargou, S.; Chabane Sari, S.M.; Senoudi, A.R.; Aida, M.; Attaf, N.; Hakem, I.F. Effect of Solution Flow Rate on Growth and Characterization of Nanostructured ZnO Thin Films Deposited Using Spray Pyrolysis. *J. Mater. Environ. Sci.* **2016**, *7*, 3134–3147.
321. Winkler, N.; Wibowo, R.A.; Kautek, W.; Dimopoulos, T. Influence of the Aqueous Solution Composition on the Morphology of Zn_{1-x}Mg_xO Films Deposited by Spray Pyrolysis. *J. Mater. Chem. C* **2019**, *7*, 3889–3900. [[CrossRef](#)]
322. Arca, E.; Fleischer, K.; Shvets, I.V. Influence of the Precursors and Chemical Composition of the Solution on the Properties of ZnO Thin Films Grown by Spray Pyrolysis. *J. Phys. Chem. C* **2009**, *113*, 21074–21081. [[CrossRef](#)]
323. Suresh, R.; Ponnuswamy, V.; Mariappan, R. Effect of Solvent and Substrate Temperature on Morphology of Cerium Oxide Thin Films by Simple Nebuliser Spray Pyrolysis Technique. *Mater. Technol.* **2015**, *30*, 12–22. [[CrossRef](#)]
324. Ebin, B.; Arig, E.; Özkal, B.; Gürmen, S. Production and Characterization of ZnO Nanoparticles and Porous Particles by Ultrasonic Spray Pyrolysis Using a Zinc Nitrate Precursor. *Int. J. Miner. Metall. Mater.* **2012**, *19*, 651–656. [[CrossRef](#)]
325. Al Ghamdi, S.D.; Alzahrani, A.O.M.; Aida, M.S.; Abdel-wahab, M.S. Influence of Substrate Temperature and Solution Molarity on CuO Thin Films' Properties Prepared by Spray Pyrolysis. *J. Mater. Sci. Mater. Electron.* **2022**, *33*, 14702–14710. [[CrossRef](#)]
326. Hameed, S.A.; Kareem, M.M.; Khodair, Z.T.; Mohammed Saeed, I.M. The Influence of Deposition Temperatures on the Structural and Optical Properties for NiO Nanostructured Thin Films Prepared via Spray Pyrolysis Technique. *Chem. Data Collect.* **2021**, *33*, 100677. [[CrossRef](#)]
327. Rahemi Ardekani, S.; Sabour Rouh Aghdam, A.; Nazari, M.; Bayat, A.; Yazdani, E.; Saievar-Iranizad, E. A Comprehensive Review on Ultrasonic Spray Pyrolysis Technique: Mechanism, Main Parameters and Applications in Condensed Matter. *J. Anal. Appl. Pyrolysis* **2019**, *141*, 104631. [[CrossRef](#)]
328. Omar, H.; Omar, H. Substrate to Nozzle Distance Influence on the Properties of Zinc Oxide Films Formed with Chemical Spray Pyrolysis Technique. *J. Eng. Technol. Appl. Sci.* **2019**, *4*, 9–18. [[CrossRef](#)]
329. Wang, W.N.; Itoh, Y.; Lenggoro, I.W.; Okuyama, K. Nickel and Nickel Oxide Nanoparticles Prepared from Nickel Nitrate Hexahydrate by a Low Pressure Spray Pyrolysis. *Mater. Sci. Eng. B Solid-State Mater. Adv. Technol.* **2004**, *111*, 69–76. [[CrossRef](#)]
330. Hathot, S.F.; Abbas, S.I.; AlOgaili, H.A.T.; Salim, A.A. Influence of Deposition Time on Absorption and Electrical Characteristics of ZnS Thin Films. *Optik (Stuttg.)* **2022**, *260*, 169056. [[CrossRef](#)]
331. Saha, J.K.; Jang, J.; Billah, M.M.; Bukke, R.N.; Kim, Y.G.; Mude, N.N.; Siddik, A.B.; Islam, M.M.; Do, Y.; Choi, M. Highly Stable, Nanocrystalline, ZnO Thin-Film Transistor by Spray Pyrolysis Using High-K Dielectric. *IEEE Trans. Electron Devices* **2020**, *67*, 1021–1026. [[CrossRef](#)]
332. Bae, J.; Ali, A.; Jang, J. Spray Pyrolyzed Amorphous InGaZnO for High Performance, Self-Aligned Coplanar Thin-Film Transistor Backplanes. *Adv. Mater. Technol.* **2023**, *8*, 2200726. [[CrossRef](#)]
333. Ozório, M.S.; Vieira, D.H.; Nogueira, G.L.; Martin, C.S.; Alves, N.; Constantino, C.J.L. Effect of the Gate Electrodes/Water Interface on the Performance of ZnO-Based Water Gate Field-Effect Transistors. *Mater. Sci. Semicond. Process.* **2022**, *151*, 107045. [[CrossRef](#)]

334. Morais, R.M.; Vieira, D.H.; Ozorio, M.D.S.; Pereira, L.; Martins, R.; Alves, N. UV-Assisted Annealing Effect on the Performance of an Electrolyte-Gated Transistor Based on Inkjet Printed ZnO Nanoparticles Blended with Zinc Nitrate. *IEEE Trans. Electron Devices* **2022**, *69*, 1538–1544. [[CrossRef](#)]
335. Vieira, D.H.; Nogueira, G.L.; Ozório, M.S.; Fernandes, J.D.; Seidel, K.F.; Serbena, J.P.M.; Alves, N. A Performance Comparison between Honey and Water as Electrolytic Dielectrics for ZnO Liquid-Gated Transistors. *Appl. Phys. A Mater. Sci. Process.* **2023**, *129*, 272. [[CrossRef](#)]
336. Ozório, M.S.; Nascimento, M.R.; Vieira, D.H.; Nogueira, G.L.; Martin, C.S.; Lima, S.A.M.; Alves, N. AZO Transparent Electrodes Grown in Situ during the Deposition of Zinc Acetate Dihydrate onto Aluminum Thin Film by Spray Pyrolysis. *J. Mater. Sci. Mater. Electron.* **2019**, *30*, 13454–13461. [[CrossRef](#)]
337. Bertoldo, L.H.T.; Nogueira, G.L.; Vieira, D.H.; Klem, M.S.; Ozório, M.S.; Alves, N. Analytical Study of a Solution-Processed Diode Based on ZnO Nanoparticles Using Multi-Walled Carbon Nanotubes as Schottky Contact. *J. Mater. Sci. Mater. Electron.* **2022**, *33*, 14508–14518. [[CrossRef](#)]
338. Vijayan, K.; Vijayachamundeeswari, S.P.; Sivaperuman, K.; Ahsan, N.; Logu, T.; Okada, Y. A Review on Advancements, Challenges, and Prospective of Copper and Non-Copper Based Thin-Film Solar Cells Using Facile Spray Pyrolysis Technique. *Sol. Energy* **2022**, *234*, 81–102. [[CrossRef](#)]
339. Shahiduzzaman, M.; Hossain, M.I.; Visal, S.; Kaneko, T.; Qarony, W.; Umezu, S.; Tomita, K.; Iwamori, S.; Knipp, D.; Tsang, Y.H.; et al. Spray Pyrolyzed TiO₂ Embedded Multi-Layer Front Contact Design for High-Efficiency Perovskite Solar Cells. *Nano-Micro Lett.* **2021**, *13*, 36. [[CrossRef](#)]
340. Lv, L.; Wang, Y.; Cheng, P.; Zhang, B.; Dang, F.; Xu, L. Ultrasonic Spray Pyrolysis Synthesis of Three-Dimensional ZnFe₂O₄-Based Macroporous Spheres for Excellent Sensitive Acetone Gas Sensor. *Sens. Actuators B Chem.* **2019**, *297*, 126755. [[CrossRef](#)]
341. Filipovic, L.; Selberherr, S. Spray Pyrolysis Deposition for Gas Sensor Integration in the Backend of Standard CMOS Processes. In Proceedings of the 2014 IEEE 12th International Conference on Solid-State and Integrated Circuit Technology, ICSICT 2014, Guilin, China, 28–31 October 2014; pp. 1–4.
342. Tombak, A.; Ocak, Y.S.; Bayansal, F. Cu/SnO₂ Gas Sensor Fabricated by Ultrasonic Spray Pyrolysis for Effective Detection of Carbon Monoxide. *Appl. Surf. Sci.* **2019**, *493*, 1075–1082. [[CrossRef](#)]
343. Sankar ganesh, R.; Navaneethan, M.; Mani, G.K.; Ponnusamy, S.; Tsuchiya, K.; Muthamizhchelvan, C.; Kawasaki, S.; Hayakawa, Y. Influence of Al Doping on the Structural, Morphological, Optical, and Gas Sensing Properties of ZnO Nanorods. *J. Alloys Compd.* **2017**, *698*, 555–564. [[CrossRef](#)]
344. Kundu, S.; Majumder, R.; Ghosh, R.; Pal Chowdhury, M. Superior Positive Relative Humidity Sensing Properties of Porous Nanostructured Al:ZnO Thin Films Deposited by Jet-Atomizer Spray Pyrolysis Technique. *J. Mater. Sci. Mater. Electron.* **2019**, *30*, 4618–4625. [[CrossRef](#)]
345. Xiao, B.; Jiao, A.; Zhang, Y.; Yang, L.; Zhao, X.; Wu, C.; Guo, D.; Zhan, R.; Lin, H. Mixed Potential Type Ammonia Sensor Using Fe-Substituted LaCoO₃ Sensing Electrode Prepared by Flame Spray Pyrolysis. *Sens. Actuators B Chem.* **2021**, *346*, 130470. [[CrossRef](#)]
346. Jang, H.D.; Kim, S.K.; Chang, H.; Jo, E.H.; Roh, K.M.; Choi, J.H.; Choi, J.W. Synthesis of 3D Silver-Graphene-Titanium Dioxide Composite via Aerosol Spray Pyrolysis for Sensitive Glucose Biosensor. *Aerosol Sci. Technol.* **2015**, *49*, 538–546. [[CrossRef](#)]
347. Martínez-Saucedo, G.; Ugalde-Reygadas, M.; Peña, J.J.A.; Lastra-Medina, G.; Márquez-Marín, J.; Torres-Delgado, G.; Castanedo-Pérez, R.; Chávez-Urbiola, I.R. Non-Enzymatic Glucose Sensor Using Nanostructured Copper Oxide Thin Films Deposited by Spray Pyrolysis. *Surf. Interfaces* **2023**, *37*, 102702. [[CrossRef](#)]
348. Dong, F.; Zhang, L.; Li, R.; Qu, Z.; Zou, X.; Jia, S. Electrochemical Non-Enzymatic Biosensor for Tyramine Detection in Food Based on Silver-Substituted ZnO Nano-Flower Modified Glassy Carbon Electrode. *Int. J. Electrochem. Sci.* **2021**, *16*, 210234. [[CrossRef](#)]
349. Kumar, A.; Park, G.D.; Patel, S.K.S.; Kondaveeti, S.; Otari, S.; Anwar, M.Z.; Kalia, V.C.; Singh, Y.; Kim, S.C.; Cho, B.K.; et al. SiO₂ Microparticles with Carbon Nanotube-Derived Mesopores as an Efficient Support for Enzyme Immobilization. *Chem. Eng. J.* **2019**, *359*, 1252–1264. [[CrossRef](#)]

Disclaimer/Publisher's Note: The statements, opinions and data contained in all publications are solely those of the individual author(s) and contributor(s) and not of MDPI and/or the editor(s). MDPI and/or the editor(s) disclaim responsibility for any injury to people or property resulting from any ideas, methods, instructions or products referred to in the content.